Final Research Report

**Investigation of pore space and physical properties
for the understanding of landslide mechanisms
- A case study at Kohong Range, HatYai -**

Helmut Durrast

Project

Investigation of pore space and physical properties for the understanding of landslide mechanisms - A case study at Kohong Range, HatYai

Researcher

Dr. Helmut Durrast

Geophysics Research Center

Department of Physics, Faculty of Science

Prince of Songkla University,

Hatyai, Songkhla 90112

Tel.:   074-28 8736

Fax: 074-55 8849

eMail: helmut.j@psu.ac.th

Duration

1. October 2012 to 30. September 2013 (1 Year)

Extended to 30. September 2014

Funding

Government Fund/Budget

Content

List of Figures

List of Tables

Acknowledgements

Publications

Suksawat, S. and Dürrast, H. Seismic velocities of unconsolidated sediments with clay. Proceedings of the Fifth Thailand Rock Mechanics Symposium (ThaiRock 2015), January 22-23, 2015, Romantic Resort & Spa, Khao Yai National Park, Thailand (accepted for publication).

Suksawat, S. and Dürrast, H. Electrical resistivity of unconsolidated sediments with clay. THAI JOURNAL OF PHYSICS, SERIES 10, 2014 (in press).

Abstract

The shallow subsurface, a few hundred meters in depth, comprises mainly of unconsolidated sediments, a porous material, with gravel, sand, silt, clay, and rock fragments, and it is the source for groundwater as well as the region of landslide hazards, and the main resource in agriculture, soil. For geophysical investigations of this region electrical and seismic methods are first choices; however this requires a good understanding between these physical properties and the characteristics of these unconsolidated sediments. For this study disturbed samples of unconsolidated sediments from different layers from bedrock to the top soil layer were taken from two locations of the Khao Khohong mountain range, Hat Yai, Songkhla Province. The two sample locations comprise different bedrock lithologies, sandstone and granite. The dried samples were characterized as following: main composition, grain size distribution, grain matrix density, bulk density, porosity, as well as pore structure. The electrical resistivity and seismic P- and S-wave velocities were determined under laboratory conditions with increasing water saturation (0–100%) of the sample. In general, the electrical resistivity decreases with increasing water content, with a larger gradient until about 40% saturation and a lower one above. For clay bearing sediments the electrical resistivity is the combination of electrolytic (water) and colloidal (wet clay) conductivity. With a modified Archie equation proposed by Sen et al. (1988) the laboratory derived data could be modeled; however the tortuosity factor (m, usually 2), the saturation index (n, usually 1.3), and a constant (a, usually 1) have to be modified, with m=0.3-3.1, n=1.4-2.2 for sediments from the granite site, and m=1.0-3.9, n=2.5-3.2 for the sandstone site, due to differences in the grain size distribution. The seismic velocity data show for samples from both sites a significantly decrease of the shear velocities at around 60-80% water saturation, which correlates with a decrease in the Young's modulus and an increase to almost 0.5 of the Poisson's ratio, indicating significantly changes of the mechanical properties, thus reducing the stiffness of the samples. The absolute velocity values depend on the porosity as well as the composition of the samples. This study has clearly demonstrated that sediments are different in their nature depending on their source or base rock, here granite and sandstone. The nature of the sediments also changes or can change with different states of weathering and different distances of short transportation as shown here. The different nature of the sediments has an effect on the electrical resistivity and seismic velocities. This has to be taken into account for any applications, especially in the design and calibration of sensors for landslide early warning systems.

Executive Summary

1. Introduction and Literature Review
1.1 Landslide Hazard

Landslides are a common natural hazard in many countries around the world, where abundant rainfall in combination will slopes and construction of buildings can be found. However, extreme weather events with more intensive rainfalls are becoming more common as well as land use and urban development are developing fast, so landslides "*are increasing in frequency, scope and destructive capacity*", said by Sálvano Briceño, Chair, Scientific Committee at Integrated Research on Disaster Risk, Beijing (Qiu, 2014). For example, in Zhouqu, Northwestern China, in 2010, heavy rainfall has led to a mixture of mud and rocks that flattened 550 houses and killed nearly 1,800 people. In May 2014 a mudslide in northeastern Afghanistan killed more than 2,000 people in the village of Ab Barak. In August 2014 a mudslide in Japan's Hiroshima Prefecture killed more than fifty people after in one day the equivalent of one month rain felt in the area (see Figure 1.1). A recent study by has revealed that of the 32,322 landslide fatalities between 2004 and 2010, most occurred in Asia, mainly in the Himalaya Mountains and in China (Petley, 2012).

Figure 1.1: Land(mud)slide in Japan, Hiroshima, in August 2014 (from BBC, 2014).

The main physical mechanism behind such destructive forces is the slope failure, where parts of a hill slope becomes detached. Water has infiltrated the soils and sediments after and during heavy rainfalls and as groundwater it acts somehow as a lubricant between the grains and weakening the whole system leading to an unstable

hill slope. Two-thirds of landslides are triggered by rainfall. According to Kyoji Sassa from the Kyoto University in Japan, he says that the unanswered question is how rainfall can change the dynamics of the groundwater and by this the strength of soil and rock particles in the slope (Qiu, 2014).

In Thailand landslides are a common phenomenon due to deep weathered rocks and sediments and a rainy season with heavy and prolonged rainfall. Landslides occurrence is registered almost every rainy season in mountainous or hilly areas, with the latest landslide in Khao Phanom, Krabi Province, Chayia, Surat Thani Province, Lang Suan, Chumphon Province, and Kathu in Phuket Province; all occurred in March 2011, with loss of lives and livelihoods (The Nation, 2011). In January 2011 a landslide in Songkhla's Muang District killed one person at the foot of the hills. According to witnesses debris from the November flooding blocked the nearby waterway and thus causing water to change its direction and subsequently flowed into the houses at the foothills (MCOT news, 2011). More than 130 people were killed by a debris flow and associated debris flood in August 2001 in Ban Nam Ko Yai, which is situated on the alluvial fan below the canyon mouth of the same-named Nam Ko Yai stream, a tributary of Pa Sak River in Lom Sak District, Phetchabun, Central Thailand. The muddy debris flow felt trees and destroyed several houses along the stream banks with an estimation of over 200 million Bath of the property damage (Yumuang, 2005).

1.2 Physics and Mechanics of Landslides

Landslides as the motion of soil, sediments, or rocks can be described by the combination of laws related to friction, cohesion, and gravity with normal and shear stress. In case of soil containing substantial amounts of mud, so called cohesive material, and water, such a mud or debris flow can be described as rheological flow, which practically is a fluid with complex properties. On the other hand movement of granular material can result in granular flow, a type where friction plays an important role in the dynamics. Other types of landslides are slow moving masses and rock falls. All of them described above from the group of landslides under the overall regime of gravity mass flows (de Blasio, 2011; see Figure 1.2).

For the stability of slopes and the hazard of landslides the shear strength is a main geotechnical parameter to be considered; it describes the magnitude of the shear stress that a soil can sustain or the shear strength of the material is the greatest stress it can sustain. Shear strength in soils depends primarily on interactions between

particles and at finite normal stresses it is the result of two main parameters, friction and cohesion. Both parameters are determined in geomechanical laboratories using the direct shear test or triaxial shear test method (Sawangsuriya, 2012).
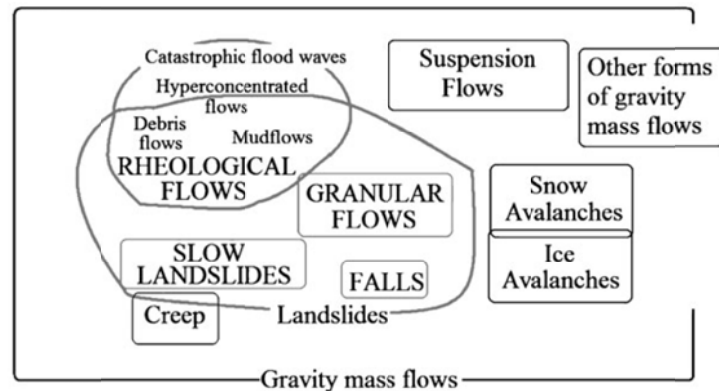
Figure 1.2: Different types of flows form the landslide group that is part of gravity mass flow (her not all kinds of gravity mass flow are shown) (from de Blasio, 2011).

Friction is usually characterized by a coefficient of friction which is the ratio of the frictional resistance force to the normal force which presses the surfaces together, here gravity. Frictional resistance is stress dependent component. Cohesion, which represents the stress independent component, is the results from electrostatic bonds between clay and silt particle in the soils and from the cementation between grains (true cohesion). Therefore, soils with no clay or silt are not cohesive except for capillary forces; they are the result of little water that forms bridges between the sand grains, thus resulting in negative pore pressure or "suction" (apparent cohesion) , which is lost upon wetting. Typical values of soil cohesion are of the order of some kPa, whereas rocks normally exhibit much greater values (e.g. Selby, 1993).

Both cohesion and friction depend on the composition of the soils, its structure, and shape and size distribution of the particles, as well as aging, altogether the nature of the soil (intrinsic variables). These parameters also influence the small strain stiffness, G_0, of the soil, which can be described by the shear wave velocity (V_S) and the total or bulk density (ρ_{total}) as following (e.g. Salgado, 2000)

$$G_0 = V_S^{\,2} \cdot \rho_{total} \tag{1.1}$$

The small strain stiffness can be determined by several methods, see below, which are relatively easy and fast. Another related parameter is the Young's modulus, which provides a value about the stiffness of the material. However, the friction and

cohesion parameters still have to be determined in the geomechanical laboratory (Sawangsuriya, 2012).

1.3 Role of Pore water

Landslides induced by heavy rainfall usually occur in areas where the slope angles are steeper than the friction angle of the soil or sediment. The reason is that only within a certain range of water saturation these slopes are stable. This is when the effect of suction creates an apparent cohesion between the soil and sediment particles and by this increases the shear resistance between the soil or sediment particles (e.g., Fredlund and Rahardjo, 1993; Springman et al., 2003). If the saturation gets above a certain or critical value both parameters, suction and shear resistance, are significantly reduced (e.g. Pagano et al., 2010). Especially heavy rainfalls results in higher water saturation that may exceed a critical limit in certain parts of a slope, and by this starting the local failure, which consequently is leading to a landslide or debris flow (e.g. Sassa et al., 2010).

Further, the fast infiltration of rainwater in natural slopes can result in higher water pressures inside the pores of the soil and sediments. In has to be noted that in the near–surface vadose zone air is always present and by this influencing the infiltration of the water, as the gas phase can transmit the pressure during the infiltration (Hartge and Horn, 1999). In case the near–surface soils and sediments are separated in layers with different permeability or hydraulic conductivity they can create buoyancy effects when the water is flowing beneath low–permeable layers (e.g. Stadler et al., 2009). Further important parameters of how and how fast the rainwater infiltrates the soil and sediments are the occurrence and distribution of pores with different sizes (pores size distribution), which have an effect. Especially of importance are the occurrence and distribution of macropores (e.g. root channels, fissure, soil cracks, borrows from earthworms and other animals; Beven and German, 1982; Jarvis, 2007), as they are responsible for a fast infiltration and pressure reaction in the soil and sediments (e.g. Uchida et al., 2001). Further, macropores in a low–permeable matrix create a dual–permeability system that will affect the infiltration and the water flow down the slope of a hill or mountain (e.g. Stadler et al., 2008).

Every slope is different, with different soils and sediment, different materials, and these materials having different properties, e.g. porosity, permeability, or the distribution of macropores, and due to these differences the processes leading to the slope failure (landslide) can be also different. A detailed investigation of the slope structure and geometry is necessary. This is also of importance for any geophysical

investigations prior to an installation of any landslide early warning system at any given slope (e.g. Friedel et al., 2006). Especially, the electrical and seismic properties are significantly affected by the composition of the material (e.g. clay content; Guenzel, 1994) as well as the pore space properties (porosity and permeability, e.g. Schön, 1983) and the water saturation (e.g. Sharma et al., 2010). The later one is subject to change over time due to water infiltration after rainfall.

1.4 Electrical Properties of Unconsolidated Sediments

Electrical resistivity method is one of the most used geophysical methods in shallow investigation, for example soil moisture content in agriculture, or as vertical electrical sounding in groundwater exploration. It is based on measuring the electrical potentials between one electrode pair while transmitting a direct current between another electrode pair (Telford et al., 1990). Electrical resistivity is a parameter exhibiting a large range of values sensitive to various factors like the nature of material (e.g., gravel, sand, and clay), the water content and its conductivity, porosity, permeability, and the water or fluid saturation. Table 1.1 gives an overview over electrical conductivity values for common unconsolidated materials of the shallow subsurface.

Table 1.1. Electrical resistivity values of common unconsolidated sediments (after Telford et al., 1990; Reynolds, 1997).

Material	Electrical conductivity (S/m)
Clays	0.01 – 1.00
Top soil	5.8×10^{-4} -4.0×10^{-3}
Soil (40% clay)	0.125
Soil (20% clay)	0.030
Sand and gravel	0.01-0.03
Unconsolidated wet clay	0.05
Alluvium and sand	$1.25 \times 10^{3} – 1.0 \times 10^{-1}$

The shallow subsurface is a few hundred meters in depth, comprises mainly of unconsolidated sediments, porous material, solid fragmental material from weathering of rocks, transported and deposited by air, but mainly by water, that form layers on the Earth's surface at normal temperature and pressure conditions; near surface in unconsolidated form, e.g., sand, gravel, silt, mud, alluvium (Immoor, 2006). Unconsolidated sediment characteristics are composition, grain size, grain shape, grain arrangement, as well as pore size and shape.

The electrical resistivity (ρ, Ohm-m) of a homogeneous cylindrical solid of length L in meters and with a cross section area A in square meters, having resistance R in ohms between the end faces, is given as, (Telford et al., 1990):

$$\rho = \frac{RA}{L}$$

(1.2)

The resistivity of a saturated porous rock can be expressed by Archie's law (Telford et al., 1990) as below

$$\rho = aS^{-n}\phi^{-m}\rho_w$$

(1.3)

where S is the degree of the water saturation, ϕ is porosity, ρ_w is the resistivity of pore fluid or water (it is temperature dependent), *m* is the tortuosity factor (m is used like porosity exponent, shape factor, or cementation degree), *n* is the saturation exponent, a is the constant that reflects the influence of mineral grains on current flow (Kirsch, 2006). In general, the exponent *m* and the parameter *a* expresses empirically the complicated pore channel geometry with respect to the electrical current flow and they are therefore a kind of pore textural property. Archie noted that the exponent has a value of about 1.3 for unconsolidated sands and a range between 1.8 and 2.0 for many consolidated sandstones (Schön, 2011).

In case of a fully saturated rock (S=100%) the Archie Equation can be rewritten in the form, where F is the formation factor

$$\frac{\rho}{\rho_w} = \frac{a}{\phi^m} = F$$

(1.4)

Figure 1.3 shows the relationship between porosity and formation factor, which in a log-log scale gives a straight line. With increasing porosity the formation factor decreases. Assuming that the resistivity of the water (fluid) is not changing then the resistivity of the water-saturated rock is decreasing as the relative water content is increasing with increasing porosity.

Equation 1.3, or Archie equation, is valid only for clay free (clean) sediments as it describes the electrical resistivity of a sample only by the electrolytic conductivity of the pore filling water, respectively fluid. However, unsaturated sediments often contain clay in various structural arrangements (see Figure 1.4), except, for example, beach sand that can be considered clean sand. Shale (in rocks) or clay (in sediments) can be in a laminar arrangement, as layers between the grains; it also can be structurally distributed among the grains, or dispersed in the pore space.
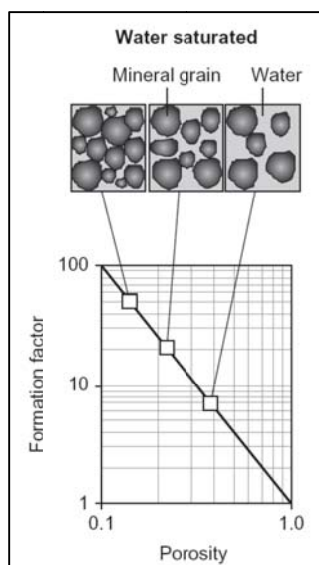
Figure 1.3. Increase of the formation factor with decreasing porosity following Archie Equation for clean, shale/clay free rocks (from Schön, 2011).
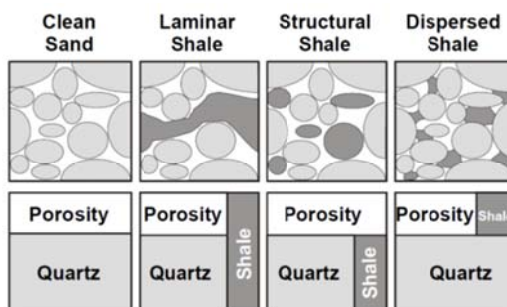
Figure 1.4. Different types of the distribution of clays in a sediment or rock in relation to quartz grains and porosity illustrated in the top and schematically drawn in the bottom (after Revil and Glover, 1998).

However, for the interpretation of resistivity data of clay bearing material the factors saturation, porosity, and clay content were identified as crucial (Sen et al., 1988). Clay minerals are hydrated minerals, which exhibit high porosity but quite low permeability values. Although clay minerals themselves are not very conductive, their surfaces can generate an excess of cations in the pore fluid adjacent to the negatively charged surfaces of the clay minerals (see Figure 1.5), see so called Stern layer (see Figure 1.5). The result is a high conductivity space near to the clay surfaces, which can dominate the overall conductivity of the sediment even if the conductivity of the pore fluid is quite low; the overall conductivity of clay bearing sediments is named colloidal conductivity.
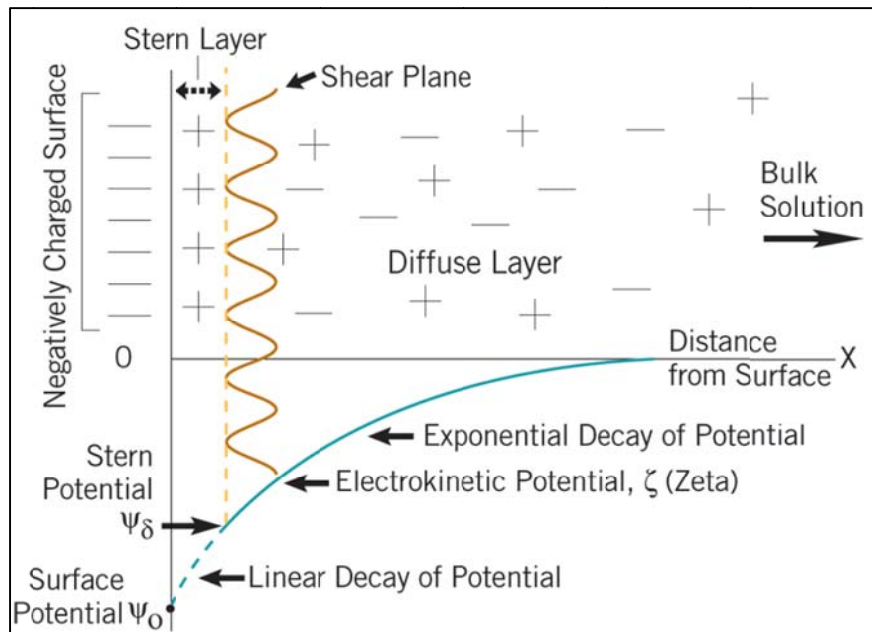
Figure 1.5. Negatively charged surface of the clay mineral (grey) generates an excess of cations in the pore fluid. The first more complete layer due to the electrostatic forces is the Stern layer having the Stern potential. The following outer layer is the shear plane that generates the zeta (ζ) potential in the pore fluid. After that is the diffuse layer showing a low and with distance decaying potential (from Practical Sciences, 2014).

Following model for the conductivity of clay bearing sediments is proposed by (Sen et al., 1988)

$$\sigma = S^n \phi^m a^{-1}[\sigma_w + AQ_v/(1 + CQ_v/\sigma_w)] \tag{1.5}$$

where, σ is soil/sediment conductivity in S/m ($\sigma = 1/\rho$), S is degree of the water saturation, ϕ is porosity, σ_w is the conductivity of water, m is the tortuosity factor (see above), n is saturation exponent, a is the constant (see above), A=1.94×m in (S/m)/(mol/l) and C =0.7/Qv in S/m, Q_v (in mol/l) is the concentration of Na-exchange cations relative to the water saturated pore space, which depends on the cation exchange capacity (C_{ex}) in mol/g and the matrix specific density ρm. Q_v replaced by Q*=Q_v/S (for partial saturation; (Guenzel, 1994), with:

$$Q_v = C_{ex}\rho_m \frac{1-\phi}{\phi}$$

$$\tag{1.6}$$

The dependence of the exchange capacity Cex on the relative clay and silt content (mineral composition of clay) P_{clay} and P_{silt} are estimated by a relationship proposed by Guenzel (1994):

$$C_{ex} = 0.47(P_{clay} + 0.2P_{silt}) \qquad (1.7)$$

Table 1.2 presents exchange capacity values, in milli-equivalents per 100 g of soil (me/100 g), for various clay minerals, which are commonly found in unconsolidated sediments. One milli-equivalent is defined as 1.0 milligram of hydrogen or the amount of any other element that is combined with it or displaced by it. Montmorillonite and Vermiculite show the highest values of the exchange capacity, whereas Kaolinite, which is a clay mineral often found and a common weathering product of feldspar, has a relatively low value.

Table 1.2. Cation exchange capacity in milli-equivalents per 100 g of soil for different clay minerals (from McNeill, 1980).

Clay	Exchange Capacity
Kaolinite	3 to 15 m-equiv/100 g
Halloysite . $2H_2O$	5 to 10
Halloysite . $4H_2O$	40 to 50
Montmorillonite	80 to 150
Illite	10 to 40
Vermiculite	100 to 150
Chlorite	10 to 40
Attapulgite	20 to 30

Table 1.3. Organic matter and clay content and CEC, in milli-equivalents per 100 g of soil for different soil types (from McNeill, 1980).

Soil Texture	Organic Matter %	Clay %	CEC* me/100 g
Sand	1.7	7	6.3
Sandy loam	3.2	13.2	13.7
Loam	4.9	16.8	20.2
Silt loam	5.4	18.4	24.0
Clay loam	5.5	31.2	27.2

The exchange capacities of typical sediments/soils are listed in Table 1.3. With higher clay content the cation exchange capacity increase, for example clay loam with 31.2 % of clay has a CEC value of 27.2 me/100 g. For clay bearing

sediments the electrical resistivity value with increasing water saturation is decreasing following Equation 1.5, assuming that the fluid resistivity is constant. Figure 1.6 shows the data for four different clays. After the volumetric water content has reached a value of about 20 to 30% the resistivity changes only slightly, whereas from 0-30% the decrease is significant.
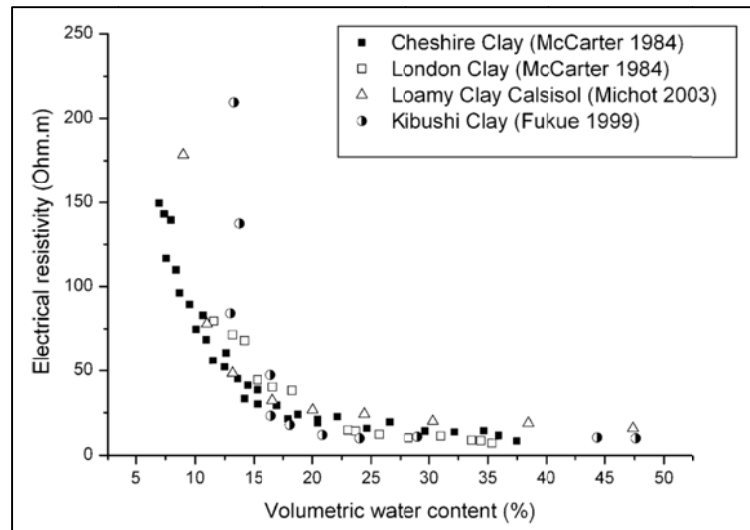
Figure 1.6. Electrical resistivity (Ohm m) versus the volumetric water content of different clay samples (from Samouëlian et al., 2005).
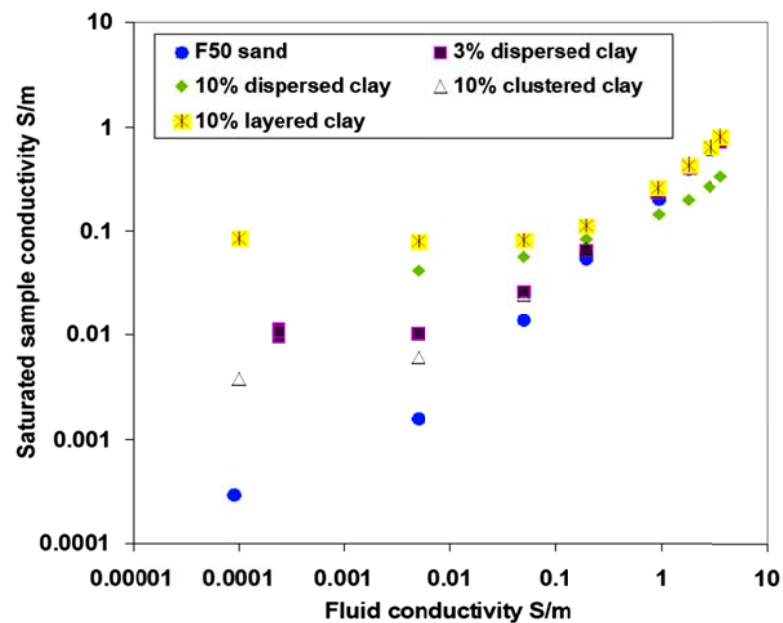
Figure 1.7. Electrical conductivity (S/m)of the saturated sample versus fluid conductivity (S/m) for a clay free sand a sand with different clay content and with clustered over dispersed to layered clay (from Wildenschild et al., 2000).

The effect of clay minerals on the overall resistivity of the soil is illustrated in Figure 1.7, here sand without/with different percentages of clays of different types. For sand the sample conductivity increases almost linearly with the fluid conductivity indicating that the soil resistivity depends only on the fluid resistivity. With increasing clay content and also from clustered over dispersed to layered clay, the sample conductivity is up to two and a half times higher than for sand and almost shows no change with increasing fluid conductivity until 0.1 to 1 S/m. This reflects the contribution of the clay minerals to the overall conductivity. Only when the fluid resistivity is significant high, about 0.1 to 1 S/m the fluid resistivity dominates the overall soil resistivity as the contribution of the clay surface to the overall resistivity is limited due to the CEC.

1.5 Seismic Properties of Unconsolidated Sediments

Wave propagation methods, determining P- and S-wave velocities, have become standard techniques in the evaluation of the stiffness of the subsurface, including the near shallow subsurface with soils and unconsolidated sediments (e.g. Santamarina et al. 2001). These methods have several advantages, mainly they are a) relatively simple, rapid, repeatable, and nondestructive, and b) when the laboratory samples are at the same conditions as those in the field a good agreement between stiffness measured in the laboratory and in the field can be achieved (see also Sawangsuriya, 2012). Table 1.4 provides an overview of the main wave propagation methods utilized.
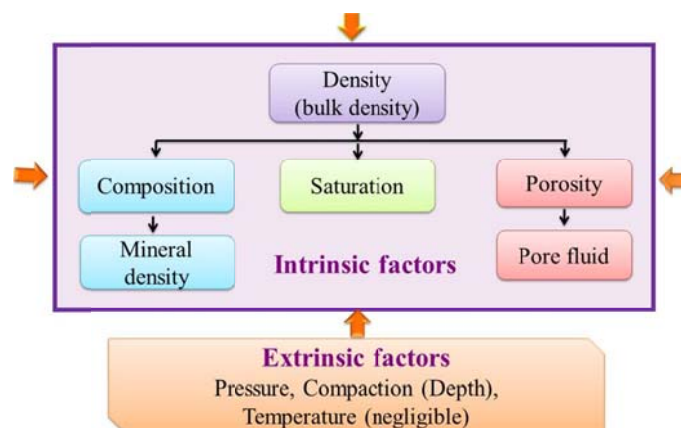
Figure 1.8. Intrinsic and extrinsic parameters of unconsolidated sediments and soil affecting the physical properties.

The main parameters affecting the seismic velocities, compressional (Vp) and shear wave velocity (Vs), are the material composition, with grain size, shape, and arrangement, bulk and mineral density, porosity, with pore size and pore distribution, and saturation, either air or water. These parameters can be summarized as intrinsic parameters (Figure 1.8), whereas pressure and temperature are extrinsic parameters. For shallow sediments and soils the latter one have almost no influence, mainly as pressure increases with depth 26.46 MPa/km (for ρ=2.70), referred to as the lithostatic pressure gradient.

Table 1.4. Summary of wave propagation methods for determining the stiffness of soils, sediments and rocks in the subsurface (after Sawangsuriya, 2012).

Test	US Standard	Methodology
Soil Stiffness Gauge (SSG)	ASTM D 6758	LABORATORY - Small dynamic force generated inside a device is applied through a ring shaped foot resting on the ground surface. Deflection is measured using velocity sensors. Near-surface stiffness is the ratio of the applied force to the measured deflection.
Bender Element	no	LABORATORY - Shear wave travel time and tip-to-tip distance of piezoceramic bender elements are used to determine shear wave velocity. With mass density the shear stiffness is calculated from that.
Resonant Column	ASTM D 4015	LABORATORY - Shear wave velocity and the corresponding shear stiffness determined from resonant frequency.
Ultrasonic Pulse Transmission	ASTM C 597	LABORATORY/FIELD - From travel time of compressional or shear wave arrivals and distance between transducers elastic wave velocity are determined and stiffness is calculated based on elastic theory.
Reflection Seismic	No	FIELD - Travel times of seismic waves reflected from subsurface interfaces following the law of reflection are measured. Wave velocities and corresponding stiffness are determined.
Refraction Seismic	ASTM D 5777	FIELD - Travel time of seismic waves refracted at subsurface interfaces (Snell's law) is measured. Wave velocity and stiffness of are determined.
Spectral Analysis of Surface Waves (SASW)	No	FIELD - Surface (Rayleigh) wave velocity varied with frequency is measured utilizing their dispersion characteristics. Surface waves propagate to subsurface depths that are proportional to their wavelengths or frequencies in order to determine the stiffness of subsurface profiles.
Seismic Cross-Hole	ASTM D 4428	FIELD/BOREHOLE - Measurement of wave velocity (Vp or Vs) from one borhole to another in a linear array. Elastic waves propagate in the horizontal direction through the subsurface and measured by the geophones.
Seismic Down-Hole or Up-Hole	No	BOREHOLE - Travel time of P - or S-wave propagate vertically in a single borehole are monitored. Wave velocity at any depths is from travel time versus depth.
Seismic Cone Penetration	No	FIELD - No borehole is required. A profile of shear wave velocity is obtained comparable to seismic down-hole test. Receiver is located in the cone.

Soils and unconsolidated sediments mainly compose of quartz, feldspar, and clay minerals, which is reflected by the mineral density. The bulk density decreases with increasing porosity, decreasing water saturation, decreasing pressure and increasing temperature. Porosity also decreases nonlinearly with depth or correspondingly compaction. As a result of compaction or increasing confining pressure both the compressional and shear wave velocities increase, due to an enhanced stiffness among the grains (Schön, 2011).

Compressional wave velocities are also controlled also by the type of pore fluid (gas, water). They increase from air to water, and they show very small changes with increasing saturation up to about 80-85%, and then the P-wave velocities abruptly increase. Shear wave velocities are not strongly controlled by the type of pore fluid and a small decrease is not influenced by the pore filling because its shear modulus is zero (Schön, 2011). However, they increase with increasing saturation due to contact level capillary forces. Subject to drying they reach their maximum at dry conditions due to salt precipitation and buttress formed by clay minerals (Santamarina et al., 2001; also Figure 1.9).
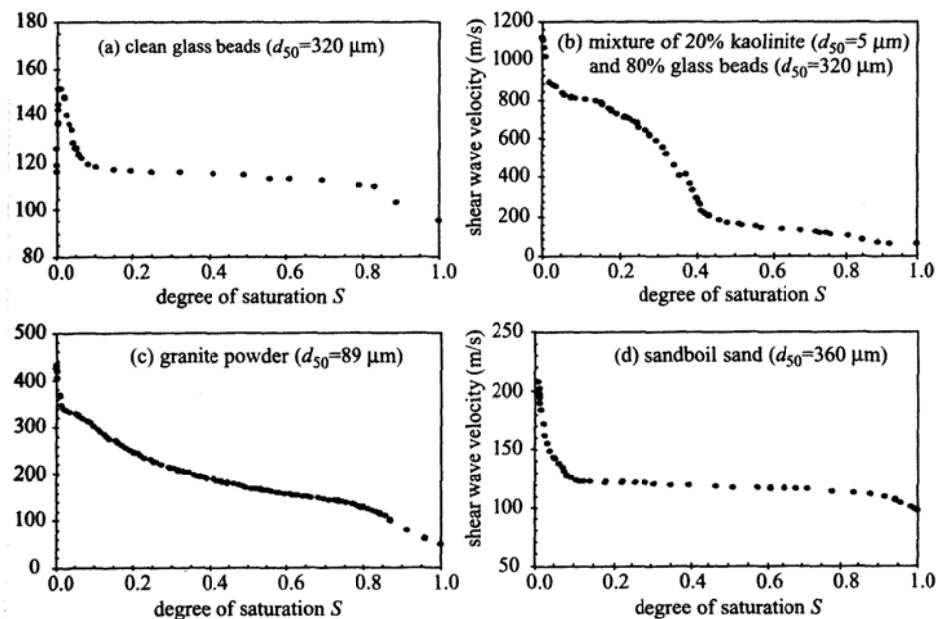
Figure 1.9. Shear wave velocities versus degree of saturation different materials representing different types of soils (vertical load of 1.5 kPa applied, after Cho and Santamarina, 2001).

Velocity values in unconsolidated sediments are distinctly lower than those in consolidated sediments. With increasing clay content, the velocity generally decreases

in unconsolidated sediments. Velocity decreases with increasing porosity and decreasing water saturation and pressure (Schön, 2011).

1.6 Landslide Early Warning System

As landslides are in some way predictable in their locations due to the known locations of potential unstable slopes, but unpredictable in occurrence time, a landslide early warning system (LEWS) is a possible choice to minimize the hazard regarding human lives, as well as properties and infrastructures. Worldwide landslides warning system are developed and employed at critical locations, e.g. an LEWS was installed after the Torgiovannetto landslide at a slope of Mount Subasio, near the city of Assisi, Perugia, Umbria Region, Central Italy (Intrieri et al., 2012), or at Anthoniar colony, Munnar, Idukki (Dist), Kerala (State), India, after this area historically experienced several landslides, with the latest one occurring in the year 2005, with death toll of eight people (Ramesh, 2014).

A landslide early warning system comprises of following main parts (see Figure 1.10), first (a) the risk knowledge, or where potential landslides can occur, the (b) the monitoring part utilizing a number of different sensors, the (c) data acquisition, followed by data analysis and the generation of forecasting scenarios, the (d) dissemination of a warning message using different warning levels, and finally (e) the response, what people or trained responders have to do in order to minimize the risk for the people, for example evacuation.
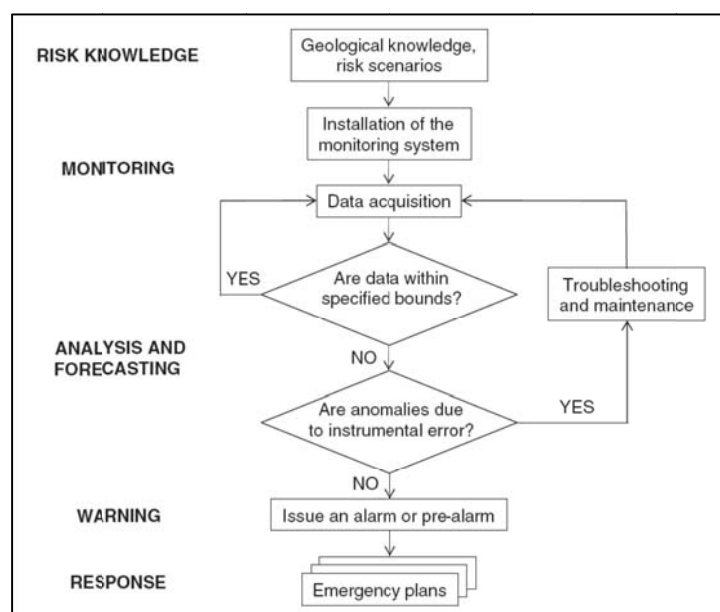
Figure 1.10. Flow chart of the activities of a generic early warning system. Modified after DiBiagio and Kjekstad (2007), from Intrieri et al. (2012).
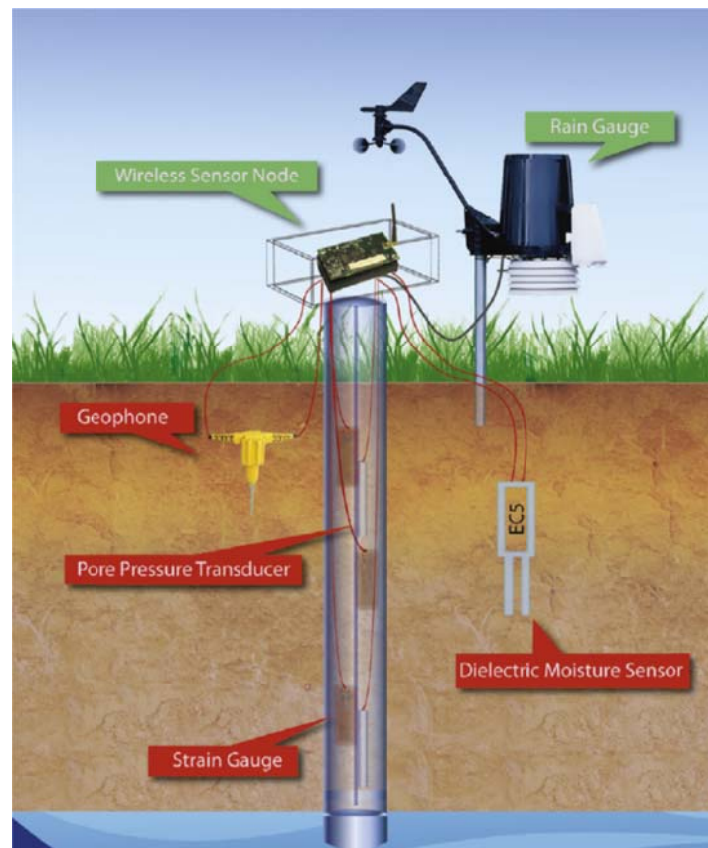
Figure 1.11. Multi-sensor station for a landslide early warning system (from Ramesh, 2014).

For a landslide early warning system several senor types are already available, depending on the different physical parameter to be measured. The main parameters of interest are changes in moisture content, pore pressure, rainfall, movement, and vibrations inside the earth, as earthquakes can trigger also landslides. Ramesh (2014) provides an overview of the main sensors currently applied for LEWSs; see also Figure 1.11.

a) Dielectric moisture sensors measuring the dielectric constant or permittivity of the soil as the electrical properties change with increasing waste content in the soil.

b) Pore pressure piezometers measure the water pressure in the pores of the soil and sediment, because increasing rainfall leads to higher water accumulation in the pores of the soil, and by this exerting a negative pressure. This can cause the loosening of the soil strength.

c) Strain gauges are used to measure the deformation of the soil layers related to any movement, which might be seen as the early onset of a later landslide.

d) High accuracy tiltmeters are used for measuring the soil layer rotational movements, which might be also the early onset of a later landslide.

e) Geophones with near real-time data collection are used for the analysis of vibrations caused during the beginning of a landslide. This demands the measurement of frequencies up to 250 Hz with a resolution of 0.1 Hz.

f) Rain gauges measure the rainfall in the area of potential landslides. Abundant rainfall is one of the main parameters causing landslides, as the water that infiltrates into the slope can change the soil properties, raising the water table, and reducing the shear strength of soils that subsequently may trigger a landslide.

g) Temperature sensors are needed as the physical properties of soil and water change with temperature.

1.7 Objective of the Study

The aims of this study are first focusing on the understanding of the processes leading to potential landslides in the study area (Kohong Range, Hat Yai) through investigations of the structure, geometry, physical properties and related mechanical parameters of soils and sediments (porous media) and the distribution of pores and flow pathways (pore space properties) by applying field and laboratory investigations. Second, from the results of the laboratory and field investigations relationships between physical properties of soils and sediments (electrical resistivity, compressional and shear wave velocities) and different water saturation levels through laboratory investigations are attempted in order to create a physical base to determine what geophysical method is sensitive to saturation changes for potential use in any landslide early warning system.

2. Methodology

2.1 Fieldwork

For this study disturbed samples of unconsolidated sediments from different layers from bedrock to the top soil layer were taken from two locations of the Khao Khohong mountain range in Hat Yai District, Songkhla Province as shown in Figure 2.1. The two sample locations comprise different bedrock lithology, the first location from UTM 0666802 East, 0779972 North, mainly granite at a mountain site in different states of weathering. The second location from UTM 0666927 East, 0774098 North, mainly sandstone with different layers from bedrock to top soil. Before the field surveys previous studies, geological map and topographic map were analyzed to identify outcrop location, mainly outcrops of shallow unconsolidated sediments. Field observation of the selected outcrops focuses on the identification of lithology, different layers, structures, stratigraphy and geologic processes were studied and recorded. Detailed photos were taken, sketched structures, description of geology, made grids, and measured strike directions of faults.

2.2 Sampling method

Sediment samples classify being either disturbed or undisturbed. The disturbed sample has been changed sufficiently that tests of structural properties of the sediment will not be representative of in-situ conditions, and only properties of the sediment grains can be accurately determined. The undisturbed sample is close enough to the conditions of the in-situ sediment to allow tests of structural properties of the sediment to be used to approximate the properties of the sediment at in-situ conditions (Wikipedia, 2014). For this study, from the first site samples (mainly granite) have been randomly collected around the area and the second site samples (mainly sandstone) have been collected as a profile from the top layer to the bottom layer (see Figure 2.2). The top layer (KH_1_2), the second layer (KH_2_2) and bottom layer (KH_3_2).
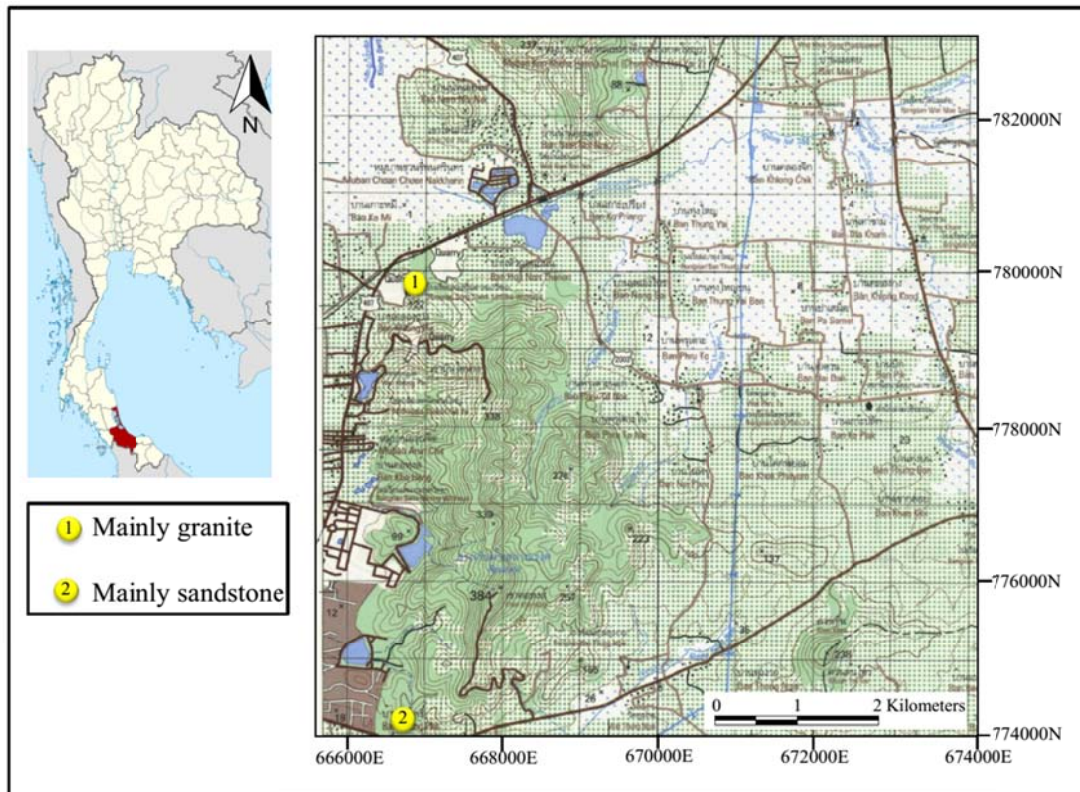
Figure 2.1 Study locations in Khao Khohong mountain range in Hat Yai District, Songkhla Province (modified from Sheet 5123III, Series L7018, Changwat Songkhla, Royal Thai Survey Department, 1997).
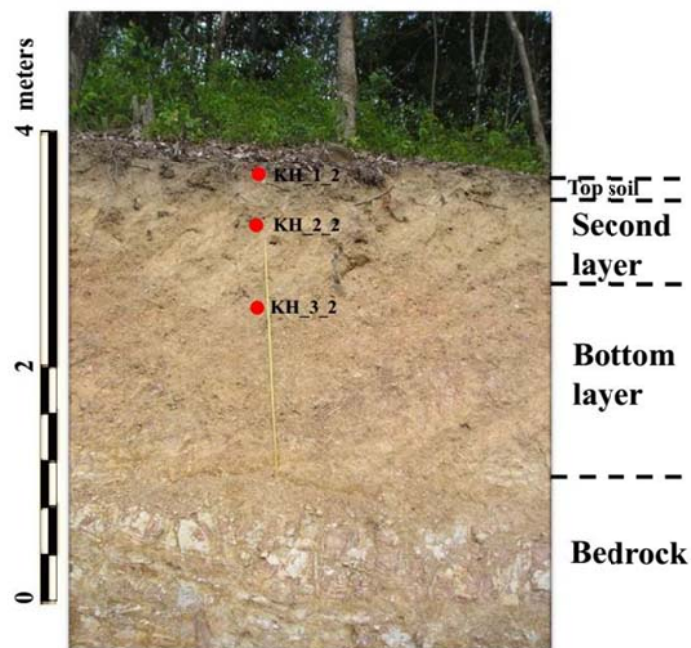
Figure 2.2 Sample of unconsolidated sediments from Khao Khohong Mountain. Bedrock is a sand/siltstone, red point is sample.

The unconsolidated sediment samples were taken as disturbed samples by shovel as shown in Figure 2.3; samples have been obtained by digging out unconsolidated sediments from the site. The unconsolidated sediment samples were two kilogram per sample and put in a plastic bag, labeled with data of sample and notes were taken about composition, grain size, grain shape, color, texture, and sedimentary structures. The first sample site has nine samples and the second sample has site 12 samples, with some samples are rocks. Samples were carried to laboratory, taken out of the plastic bag and air dried over a few weeks.

Figure 2.3 Sampling of unconsolidated sediments using standard tools (left) with the samples afterwards put in a plastic bag (right).

2.3 Density analysis

<u>Theory</u>

Density of a substance is its mass per unit volume. The symbol most often used for density is ρ. Density is defined as mass (m) divided by volume (V), as it follows from Equation 2.1, the SI unit of density is kg/m^3 or g/cm^3 is another unit commonly used in a laboratory.

$$\rho \frac{m}{V} \tag{2.1}$$

The density of a material can be separated into the matrix density (ρ_m) depends on the components (mineral), and the bulk density (ρ_b) stated with respect to the porosity of a material (e.g. Siegesmund and Dürrast, 2011). Density of minerals is

controlled by their elemental composition and internal bonding and structure. Density of porous sediments is controlled by the mineral composition (grain density), porosity, and saturation (Schön, 2011).

The bulk density ρ_b considering dry-sediments conditions is defined as the ratio of the mass of the solid phase m_s to the volume of the whole body V

$$\rho_b = \frac{m_s}{V} \tag{2.2}$$

and the matrix density of the sediments ρ_s is determined by the ratio of the mass of solid phase m_s to its volume V_s

$$\rho_m = \frac{m_s}{V_s} \tag{2.3}$$

Methodology

The mineral density was determined by the pycnometer methods using water, ASTM D854 - Standard Test Methods for Specific Gravity of Soil Solids by Water Pycnometer (AASHTO T100 - Standard Method of Test for Specific Gravity of Soils). First, recorded the weighted the mass of the empty clean and dry pycnometer, then the dry sediments sample filled into the pycnometer and the mass was about 5 g. Distilled water was added to fill the about half to three-fourth of the pycnometer (with sample), removing entrapped air, added to fill the pycnometer until full and weighted. Finally, the pycnometer was filled with distilled water only and weighted again (see Figure 2.4). This method done at Department of Mining and Materials Engineering, Faculty of Engineering, Prince of Songkla University. The specific gravity of sediment sample was calculated follow

$$Specific\ Gravity\ =\ \frac{W_p - W_{ps}}{W_p - W_{ps} - W_{psw} + W_w} \tag{2.4}$$

where W_P is mass of empty clean pycnometer in grams, W_{ps} is mass of empty pycnometer and dry sediment sample in grams, W_{psw} is mass of pycnometer, dry sediment sample and water in grams and W_w is mass of pycnometer and water in grams.
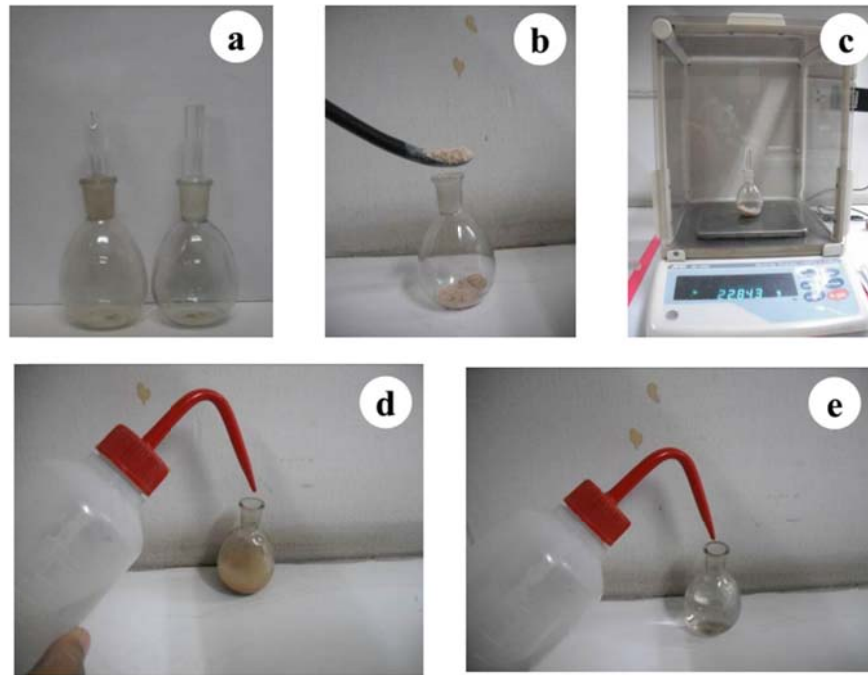
Figure 2.4 (a) Pycnometer or specific gravity bottle 25 ml, (b) sample filled into pycnometer, (c) recorded the weight, (d) distilled water added to fill the pycnometer with sample, (e) pycnometer was filled with distilled water only.

Density of sediment samples (g/m^3) calculated from specific gravity of sediment sample multiplied by density of water (g/m^3). For example, sample KB_5_2 with 23.882 g mass of empty clean pycnometer, 29.452 g mass of empty pycnometer and dry sediment sample, 52.208 g mass of pycnometer, dry sediment sample and water, 48.788 g mass of pycnometer and water, specific gravity is (23.822 – 29.452)/(23.822 – 29.452 – 52.208 + 48.788) = 2.59, density is 2.59 × 1.00 = 2.59 g/m^3.

The bulk density of a sample was obtained by measuring the dimensions of a geometric sample container filled with the sediment and by this getting the volume and weight of the dry sample, calculated from Equation 2.2.

2.4 Porosity analysis
Theory

Porosity is an intrinsic property of every material, the symbol most often used for porosity is ϕ. It refers to the amount of empty space within a material, exists between the grains of minerals and influences most physical sediment properties, e.g., elastic wave velocity, electrical resistivity, and density (Schön, 2011). Porosity is a measure of the total void spaces in a material, and is the volume of voids over the total volume, between 0 and 1. The value for total porosity can be calculated from

$$\phi = \left(1 - \frac{\rho_b}{\rho_m}\right) \times 100\% \qquad (2.5)$$

or defined by the ratio of the volume of its pores V_p to the total volume of the body

$$\phi = \frac{V_p}{V} \times 100\% \qquad (2.6)$$

Methodology

Porosity measurement, the first, the sediment samples filled into beaker and recorded volume. Then, slowly and carefully pour the water into the beaker until the water just reaches the top of the sediment sample, recorded how much water was used. Calculate the porosity by dividing the volume of water was used by the total volume of the sediment sample, expressed as percentage.

2.5 Grain Size Analysis

For analyzing the grain size distribution of the unconsolidated sediment, the distributions of the coarse particles (gravel and sand, larger than 75 μm) were determined by sieve analysis. Fine particles (silt and clay, smaller than 75 μm) were analyzed by the hydrometer method. Grain sizes can occur in a wide range of sizes from micrometer to centimeters, and the assumption is that the particles are roughly circular with the diameter measured. This test method used ASTM D 422- Standard Test Method for Particle-Size Analysis of Soils (AASHTO T88 - Standard Method of Test for Particle Size Analysis of Soils).

2.5.1 Sieve analysis

Theory

Usually data on sand and gravel fractions have been obtained from sieve analysis, which has marked theoretical and experimental limitations in the way it provides size data. Sieving sorts on the basis of smallest cross-sectional diameter (the plane of the intermediate and short axes- the diagonal length between mesh corners determines the intermediate axis length). Since most sedimentary particles are not spherical, the number of particles that pass through a given sieve is time dependent; there will always be more grains that could pass through a given sieve if they were to land with just the right orientation on the mesh (Blott and Pye, 2001).

Methodology

The sieve analysis followed ASTM C136 - Standard Test Method for Sieve Analysis of Fine and Coarse Aggregates (AASHTO No. T 27 Sieve Analysis of Fine and Coarse Aggregates). The dry sediments sample was mixed and reduced to an amount suitable for testing and selected sieves with suitable openings to get the information required for the material to be tested. The sieves were set in order of decreasing size of opening from top to bottom (see Figure 2.5) and weighed samples are poured into a top sieve which has the largest screen opening. The stack of sieves was then shaken by a mechanical sieve shaker, usually for a fixed amount of time. After the shaking is complete the sediment samples on each sieve weighed and recoded show in Taber 2.1. The weight of the sample of each sieve is then divided by the total weight to give a percentage retained on each sieve. This method done at Department of Civil Engineering, Faculty of Engineering, Prince of Songkla University.
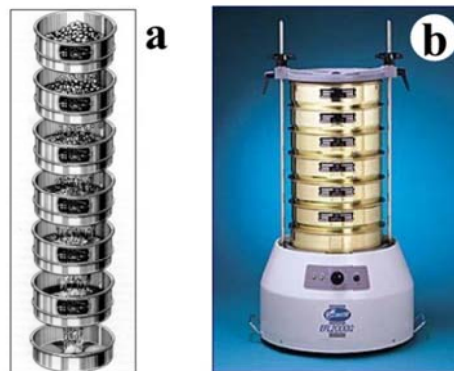
Figure 2.5 (a) sieves (solidswiki.com/images/1/1b/Analysis_sieve.gif), (b) mechanical sieve shaker (www.qclabequipment.com/efl230.jpg).

Table 2.1 Sieve analysis determination of sample (KB_5_2).

Sieve No.	Weight of Sample Retained (g)	Cumulative Weight of Sample Retained (g)	Cumulative Retained (%)	Percent Passing (%)
1 1/2″	0.00	0.00	0.00	100.00
1″	20.00	20.00	4.49	95.51
3/8″	63.00	83.00	18.65	81.35
#4	67.00	150.00	33.71	66.29
#10	78.00	228.00	51.24	48.76
#40	112.00	340.00	76.40	23.60
#200	45.00	385.00	86.52	13.48
Pan	60.00	445.00	100.00	0.00

The results of the grain size analyses were presented in a semi logarithmic plot known as particle-size distribution curves. In the semi logarithmic scale, the particle sizes were plotted on the log scale, the percent finer was plotted in arithmetic scale show in Figure 2.6.
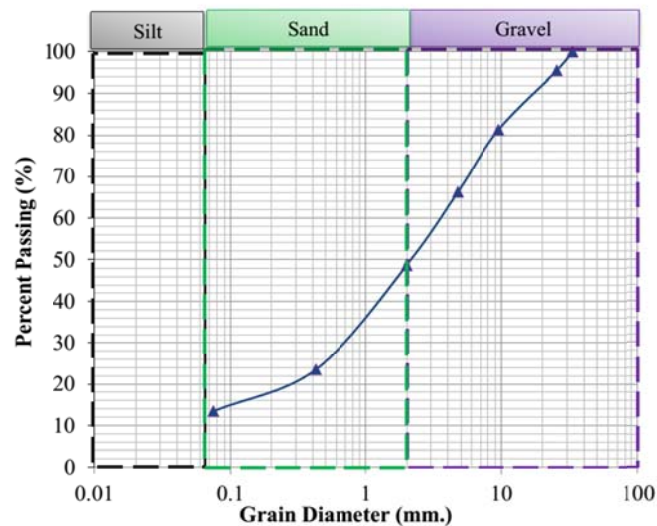
Figure 2.6 Sieve analysis determination of sample (KB_5_2), black square is sand, green square is granular, red square is pebble size.

2.5.2 Hydrometer analysis

Theory

The hydrometer analysis were used to determine the particle size distribution in a soil that is finer than 0.075 mm, which is the smallest standard size opening in the sieve analysis. The procedure was based on the sedimentation of soil grains in water. It was expressed by Stokes Law, which the velocity of the soil sedimentation was based on the soil particles shape, size, weight, and viscosity of the water. Thus, the hydrometer analysis measured the change in specific gravity of a soil-water suspension as soil particles settle out over time. This method followed ASTM D 422-Standard Test Method for Particle-Size Analysis of Soils (AASHTO T88 - Standard Method of Test for Particle Size Analysis of Soils).

Methodology

In the hydrometer method the first step was to remove the organic matter in the chemical pretreatment of many of sediments show in Figure 2.7, determined and recorded the weight, with 50 g of dry sediment samples and 100 g for sandy

sediments, and then transferred into a beaker, added 5 ml of 30 % Hydrogen peroxide (H_2O_2) and then distilled water. Adding was slowly as it will help to prevent excessive foaming. Then put the beaker on a hot plate (temperature 90 °C) and under a fume hood, while observing the samples closely for several minutes if there are much gas bubbles. Then hydrogen peroxide was added (5 ml for one time) and repeated until little or no reaction occurs. Then the sediment samples were dried at 105°C for about 1-2 days; the weight of the dry sediments samples was recorded again.
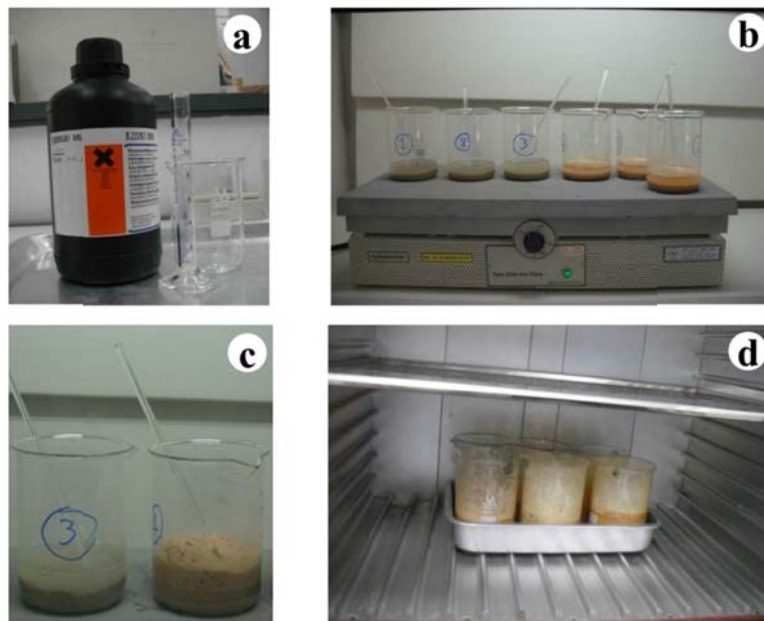
Figure 2.7 (a) 30 % Hydrogen peroxide, (b) beaker on hot plate and under a fume hood, (c) gas bubbles of sample, (d) sediment samples were dry.

The next steps are shown in Figure 2.8. First, 100 ml of 5 % calgon (50 grams of sodium hexametaphosphate ($Na_6(PO_3)_6$) and 8.3 grams of sodium carbonate (Na_2CO_3) per 1 liter of distilled water) as well as distilled water were added to the sediment samples. The sediment solution was transferred to a dispersion cup (metal milkshake cup) and shaken for about 1 min, then the sediment solution was transferred to a cylinder and water was added up to the 1 liter-mark. Then a plunger was moved up and down through the cylinder for 25-30 plunges; the plunger was removed quickly but gently. In the next step the the hydrometer (ASTM NO. 152H, with Bouyoucos scale in g/L) was put into the sediment solution immediately after the plunger was removed from the cylinder and a stop watch was started. A reading of the hydrometer and temperature was done at 50 seconds, and again after 2 hours as shown

in Table 2.2. A 100 ml mixture of the 5% calgon and 900 ml of distilled water was put in a 1,000 ml cylinder; this mixture is a blank. Here the reading of the hydrometer and temperature was also recorded at 50 seconds and again after 2 hours. This method was done at the Department of Earth Science, Faculty of Natural Resources, Prince of Songkla University.
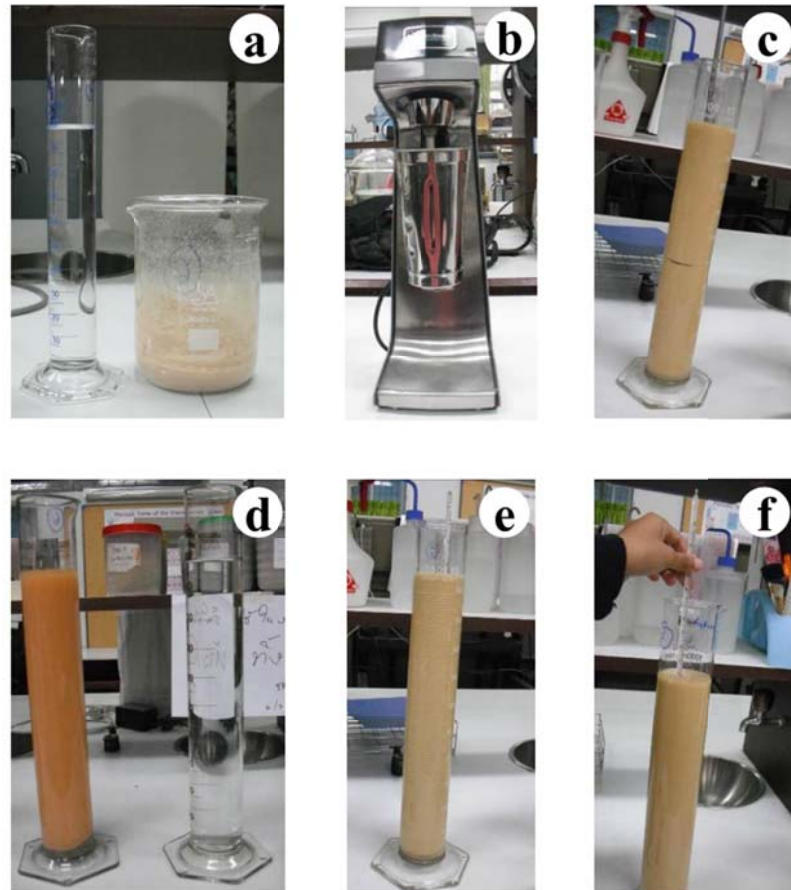
Figure 2.8 (a) 100 ml of 5 % calgon and sediment sample, (b) metal milkshake cup and shaker, (c) moved plunger up and down through the cylinder, (d) sediment solution and blank, (e) reading of the hydrometer, and (f) reading of the temperature.

The value of the hydrometer reading of the sediment solution correction (R_S^*) at time 50 seconds or 2 hours (g/L) is as follow

$$R_S^* = R_S + 0.36(T - 20) \qquad (2.7)$$

where, T is reading temperature of sediment solution at time 50 second or 2 hours (g/L), with 20 is ASTM 152H hydrometers calibrated at 20 °C directly in terms of

sediment solution concentration, R_S is density of sediment solution at time 50 seconds or 2 hours (g/L) from

$$R_S = R - R_C \qquad (2.8)$$

where R is the hydrometer reading of the sediment solution at time 50 seconds or 2 hours (g/L), R_C is calgon from temperature correction at time 50 seconds or 2 hours (g/L)

$$R_C = A - 0.5(T - B) \qquad (2.9)$$

where, A is the hydrometer reading of calgon at time 50 seconds or 2 hours (g/L), T is temperature reading of the sediment solution at time 50 seconds or 2 hours (g/L), B is temperature reading of calgon at time 50 second or 2 hour (g/L).

Table 2.2 Hydrometer analysis of sample (KH_3_2).

Name	Weight (g)	Reading hydrometer at 50 sec (g/L)	Reading temperature at 50 sec (g/L)	Reading hydrometer at 2 hr (g/L)	Reading temperature at 2 hr (g/L)
calgon	-	10.00	23.00	10.00	20.00
KH_3_2	49.43	46.00	24.00	37.50	21.50

For example, sample KH_3_2 with calgon from temperature correction at time 50 seconds is 10.00–0.5 (24.00–23.00)=9.50 g/L; calgon from temperature correction at time 2 hours = 10.00–0.5 (21.50–20.00)=9.25 g/L; density of sediment solution at time 50 seconds is 46.00 – 9.50 = 36.50 g/L; density of sediment solution at time 2 hours is 37.50–9.25=28.25 g/L; the reading of the hydrometer of the sediment solution correction at time 50 seconds is 36.50+0.36 (24.00–20)=37.94 g/L; and the reading of the hydrometer of the sediment solution correction at time 2 hours is 28.25+0.36 (21.50–20)=28.79 g/L. The results of the grain size analyses are presented in percentage of clay, silt and sand follow

clay fraction:

$$\% \, \text{clay} = \left(\frac{R_S^{*}{}_{at\,2hr}}{\text{weight of dry sample(g)}} \times 100 \right) \qquad (2.10)$$

silt fraction:

$$\% \text{ silt} = \frac{R_S{}^*_{at50s} - R_S{}^*_{at2hr}}{\text{weight of dry sample(g)}} \times 100 \tag{2.11}$$

sand fraction :

$$\% \text{ sand} = 100 - \left(\frac{R_S{}^*_{at50s}}{\text{weight of dry sample(g)}} \times 100 \right) \tag{2.12}$$

For example, sample KH_3_2 the percentage of clay is (28.79/49.43) × 100% = 58.24%, the percentage of silt is [(37.94 − 28.79)/49.43] × 100% = 18.51%, and the percentage of sand is 100 − [(37.94/49.43) × 100%] = 23.24%. The amount of each particle fraction, sand, silt and clay, determines the sediment texture and present in textural triangle for sediment textural analysis classification (USDA, 1987), for example, sample KH_3_2 is clay as shown in Figure 2.9.
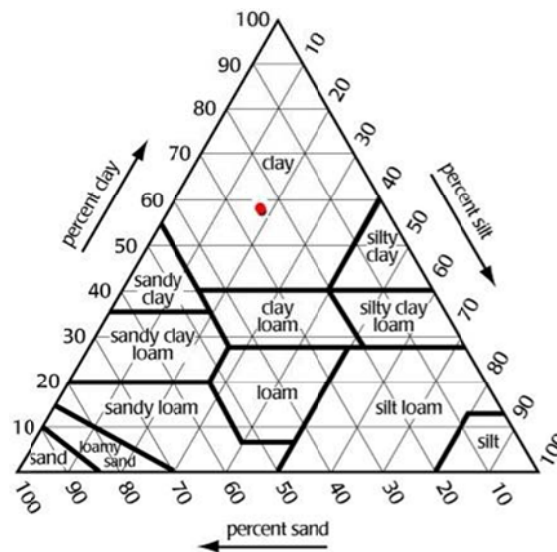
Figure 2.9 Triangle with the textural classification, red circle is sample of KH_3_2.

2.6 X-Ray Diffraction

Theory

X-ray diffraction (XRD) is the most widely used technique for mineral identification, particularly for minerals of very small size, where X-rays are diffracted by the atomic layers in crystals. As each different mineral has a distinct set of atomic layer spacing (called d spacing), a suite of measurements can be used to identify the mineral (Harris and White, 2008). All crystalline minerals in a sample can be identified from one XRD scan, provided that they are present in sufficient abundance;

however, XRD will not detect non-crystalline components (e.g., the allophane clays) in a sample because they have no regular atomic planes. The relationship between the wavelengths of the X-ray used, the angle between the incident and the diffracted X-rays, and the distance between the atomic layers causing the diffraction is given by the Bragg's law equation

$$2d \sin \theta = n\lambda \qquad (2.13)$$

where, d is the atomic layer spacing (in angstrom units) between the diffracting planes, θ is half the angle between the incident X-ray and the diffracted X-rays, n is an integer ($n =1$ for first-order diffraction peaks, 2 for second-order peaks, etc.), λ is the wavelength of the radiation used, for $Cu_{k\alpha}$ radiation ($\lambda = 1.5418$ Å) (Lewis and McConchie, 1994).

Methodology

Samples for the powder diffraction studies were finely ground (< 5 µm) and completely homogeneous. The fine powder was prepared for analysis by packing the powder into the well (about 2 mm deep) of a sample holder designed to fit into the goniometer. This method was done at the Scientific Equipment Center, Prince of Songkla University and the X-ray diffractometer as shown in Figure 2.11 was X' Pert MPD, PHILIPS, Netherlands.

Information gained from diffraction angles and relative peak intensities were used to establish structural details of the minerals using the International Powder Diffraction File (PDF) database (see Figure 2.10), complied by the Joint Committee for Powder Diffraction Standards (JCPDS) show in Table 2.3.
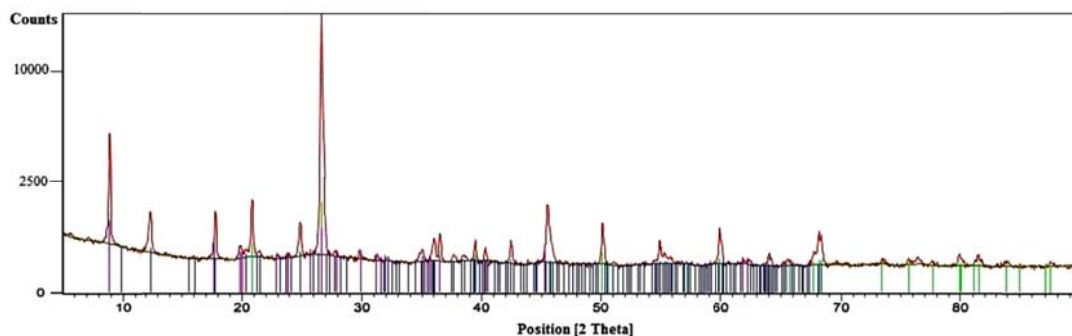
Figure 2.10 International Powder Diffraction File (PDF) database of KB_5_2.

Table 2.3 Joint Committee for Powder Diffraction Standards (JCPDS) of KB_5_2.

Sample Name	JCPDF No.	Chemical Name	Chemical Formula
KB_5_2	03-065-0466	Quartz low, syn	SiO_2
	01-080-0886	Kaolinite 1\ITA\RG	$Al_2(Si_2O_5)(OH)_4$
	00-026-0911	Illite-2\ITM\RG#1[NR]	$(K,H_3O)Al_2Si_3AlO_{10}(OH)_2$

Figure 2.11 X-ray Diffractometer, PHILIPS, The Netherlands.

2.7 Scanning electron microscopy

Theory

The scanning electron microscope (SEM) uses electrons instead of light to form an image (Schweitzer, 2010). Accelerated electrons carried significant amounts of kinetic energy, and this energy is dissipated as signals produced by electron-sample interactions. These signals include secondary electrons, backscattered electrons (BSE), diffracted backscattered electrons (EBSD), photons (characteristic X-rays that are used for elemental analysis and continuum X-rays), visible light (cathodoluminescence–CL), and heat. Secondary electrons can show morphology and topography on samples and backscattered electrons are for illustrating contrasts in composition in multiphase samples. X-ray generation is produced by inelastic collisions of the incident electrons with electrons in discrete orbitals (shells) of atoms in the sample (Swapp, 2013).

Method

As SEM utilizes vacuum conditions and uses electrons to form an image, special preparations must be done to the sample. All water must be removed from the samples because the water would vaporize in the vacuum. All metals are conductive and require no preparation before being used. All non-metals need to be made conductive by covering the sample with a thin layer of conductive material. This is done by using a device called a sputter coater. The sputter coater uses an electric field and argon gas show in Figure 2.12 (b). The sample is placed in a small chamber that is at a vacuum. Argon gas and an electric field cause an electron to be removed from the argon, making the atoms positively charged. The argon ions then become attracted to a negatively charged gold foil. The argon ions knock gold atoms from the surface of the gold foil. These gold atoms fall and settle onto the surface of the sample producing a thin gold coating (Schweitzer, 2010). This method was done at the Scientific Equipment Center, Prince of Songkla University and a Scanning Electron Microscope, Quanta 400, FEI, Czech Republic was used (see Figure 2.12 (c)).
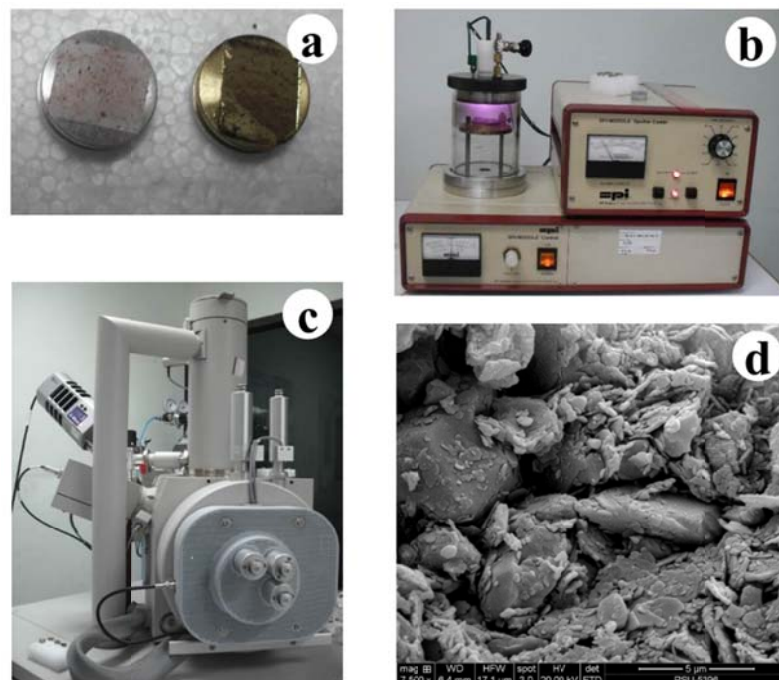
Figure 2.12 (a) Sample before and after gold coating, (b) sputtering equipment, (c) Scanning Electron Microscope, Quanta 400, (d) image of sample of KH_1_2.

Backscattered electron images in the SEM displayed compositional contrast that results from different atomic number elements and their distribution. Energy Dispersive Spectroscopy (EDS) allows one to identify what those particular elements

are and their relative proportions. Initial EDS analysis usually involves the generation of an X-ray spectrum from the entire scan area of the SEM. Below is a secondary electron image of a sample and the corresponding X-ray spectra that was generated from the entire scan area. The Y-axis shows the counts and the X-axis shows the energy level of those counts show in Figure 2.13. The EDS software is from Oxford (England).
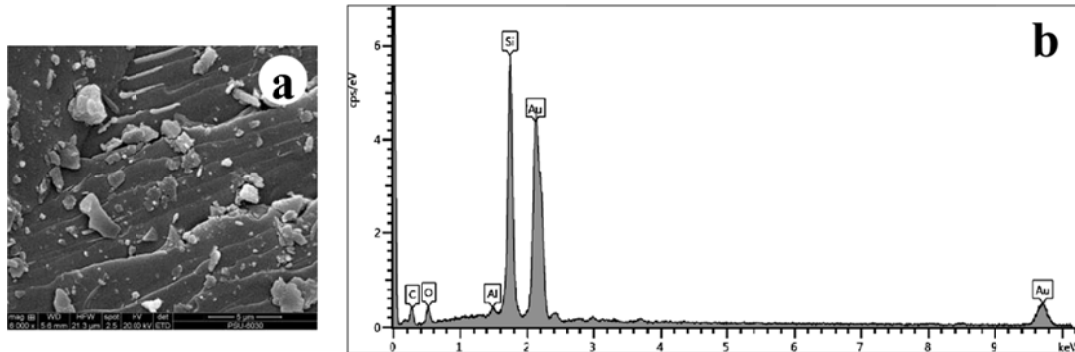
Figure 2.13 (a) SEM image of sample of KB_6_3, (b) graph of KB_6_3 from EDS software (Oxford, England).

2.8 Hydraulic conductivity

Theory

Hydraulic conductivity (K) is a property that provides information about the speed water moves through a material. It is directly related to the porosity and permeability of the material and the density of the water (Herod, 2011). Darcy's law states that the velocity water flows through a material is dependent on the material, which it flows through and the hydraulic gradient, which is the difference in water level between two points of measurement divided by the distance between them (Herod, 2011).

$$Q = -KA\left(\frac{h_{in1} - h_{out}}{L}\right) \tag{2.14}$$

where Q is the discharge or the amount of water that flows out of a material over a set amount of time, K is the hydraulic conductivity, A is the cross sectional area perpendicular to the flow, L is flow path length, h is hydraulic head, Δ is denotes the change in h over the path L and $(h_{in}-h_{out})/L$ is the hydraulic gradient (i) (Herod, 2011). Figure 2.14 shows the Darcy's experiment.
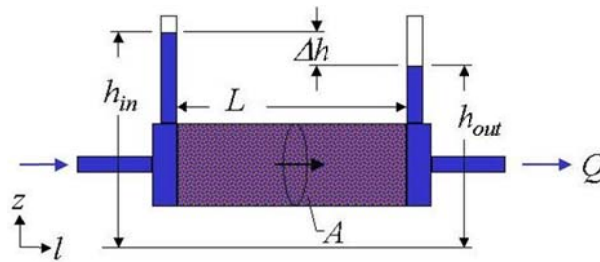
Figure 2.14 Darcy's experiment (Brown, 2013). Z represents vertical and l horizontal dimension direction.

Permeability characterizes the ability of sediment to transmit a fluid. It connects the fluid flow rate with the applied pressure gradient and the fluid viscosity and controlled by the connected passages of the pore space. For a given hydraulic head gradient, a higher the permeability means a higher fluid velocity. Permeability as defined by Darcy's law is in fact a property of both the soil and the fluid (Barends, 2013).

$$K = \frac{kv}{\mu} \qquad (2.15)$$

where κ is the intrinsic permeability in m², K is the hydraulic conductivity in m/s, v is the volumetric weight of the fluid and μ is the dynamic viscosity of the fluid.

The hydraulic conductivity of sediment depends on several factors e.g. fluid viscosity, pore size distribution, grain size distribution; void ratio, roughness of mineral and degree of sediment saturation. Other major factors that affect the permeability of clays are the ionic concentration and the thickness of layers of water held to the clay. Two standard laboratory tests are used to determine the hydraulic conductivity of sediment, the constant head test (for coarse grained sediment) and the falling head test (for fine grained sediment) (e.g., Das, 2006).

Measurement

A falling head permeability test device was designed and built at the Department of Physics, Faculty of Science, Prince of Songkla University, shown in Figure 2.15 and 2.16, following ASTM D5084-03 Standard Test Methods for Measurement of Hydraulic Conductivity of Saturated Porous Materials Using a Flexible Wall Permeameter. First, the inside diameter of the upper and lower chambers were measured, and then the average inside diameter of the chambers calculated and recorded. A porous stone was placed on the inner support ring in the base of the chamber; then a filter paper was placed on top of the porous stone and the chamber on top of the filter paper. The mixed sediment sample was poured into the

lower chamber until full; the top surface of the sediment samples was leveled and a filter paper, the upper porous stone, the support ring and upper chamber were placed as shown in Figure 2.16. The sediment samples length and diameter inside the standpipe was measured and recorded. Water flows from the standpipe through the sediment. The initial head difference h_1 at time t=0 was recorded, and water flows through the sediments specimen such that final head difference at time $t=t_1$ is h_2, temperature and time were recorded. The flow rate of the water through the specimen at any time t can be given by

$$K = \frac{aL}{At} In \frac{h_1}{h_2} \qquad (2.16)$$

where, K is Hydraulic conductivity in cm/sec, a is cross-section of tube in cm^2, L is height of soil sample in cm, A is cross-section of soil sample in cm^2, t is time of test in second, h_1 is height of water table at time t_0 in cm, h_2 is height of water table at time t_1 in cm.

Accordingly, the inside diameter of the chambers was 9.7 cm, the inside diameter of the standpipe 0.58 cm, 73.90 cm^2 was the area of the sediment sample (A), and 0.26 cm^2 the area of the standpipes (a). For example, sample KH_1_2, the length of the sediment samples 11.60 cm, 244.2 seconds was the recorded time, 4 cm the height of the water table at time t_0, 120 cm the height of water table at time t_1, therefore 6.0×10^{-3} cm/sec was the hydraulic conductivity for this sample following Equation 2.16.
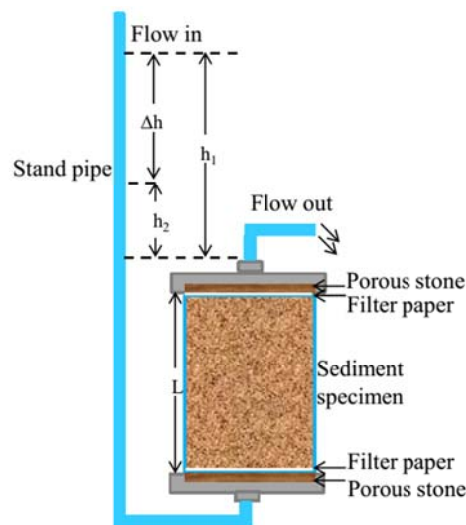
Figure 2.15 Schematic diagrams of falling head permeability test.
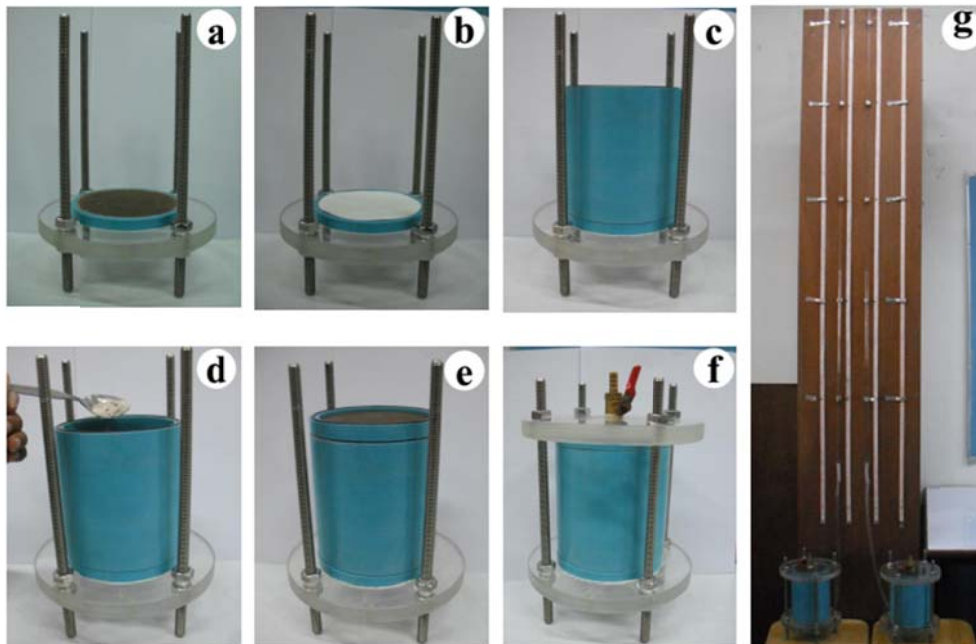
Figure 2.16 Steps of measurement the hydraulic conductivity: (a) Fist placed one porous stone on the inner support ring in the base of the chamber, (b) placed a filter paper on top of the porous stone, (c) placed chamber on top the filter paper, (d) poured sediment samples into the lower chamber, (e) placed the filter paper, porous stone and support ring on top surface of the sediment samples, (f) placed top of chamber, and (g) shows the assembled falling head permeability test.

2.9 Electrical resistivity

The electrical resistivity ρ (in unit Ohm-m) relates the electrical potential and current to the geometrical dimension of the specified region; it is the inverse of the conductivity. Assuming a homogeneous cylindrical solid of length L in meters and cross section area A in square meters, having resistance R in ohms between the end faces, the resistivity can be expressed by the follow equation (Telford et al., 1990)

$$\rho = \frac{RA}{L} \tag{2.17}$$

2.9.1 Electrical resistivity laboratory measurement

Electrical resistivity measurements in the laboratory were modified from the ASTM G187 - Standard Test Method for Measurement of Soil Resistivity Using the Two-Electrode Soil Box Method (AASHTO T 288-91 Standard Method of Test for

Determining Minimum Laboratory Soil Resistivity). The sediment box has a length of 0.078 m; 0.052 m was the width, and 0.065 m the height, so 0.003 m^2 the area, and 0.043 m of area divided by the width. This method using the sediment box was tested with a salt (NaCl) solution with different concentrations. Figure 2.17 shows the comparison between the resistivity from the laboratory using the sediment box and resistivity from Schlumberger (2000). For a range of different NaCl concentrations both values show a good similarity.
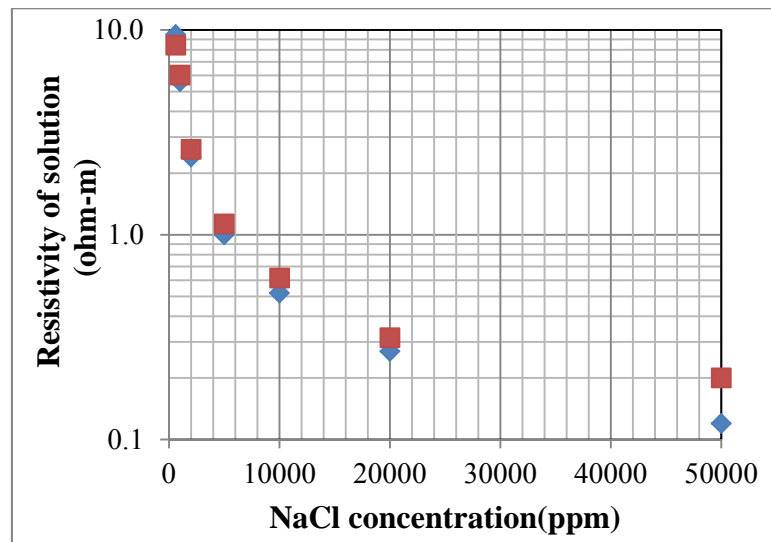
Figure 2.17 Comparisons between resistivity from laboratory for a NaCl solution (red square) and resistivity from Schlumberger (2000) for a NaCl solution (blue diamond).

Sediment samples were compacted in the box with the weight recorded. Two voltage electrodes were connected to the sediment sample through electrically conductive aluminum foil at both ends of the box. Cables were connected with the sample, a power source and a current and voltage meter. Current and voltage were measured and converted into apparent resistivity shown in Figure 2.18, recorded value of current and calculated electrical resistivity from Equation 2.18. The electrical resistivity was determined under laboratory conditions at room temperature, around 28 °C, with increasing water saturation from 0 to 100% of the sample in several steps, around 14-15, as following

$$\rho = \left(\frac{V}{I}\right)\left(\frac{A}{s}\right)$$

(2.18)

where ρ is electrical resistivity in Ohm-m, V is electrical potential in volt, I is electrical current in ampere, A is cross sectional area in m^2, s is length in m. For example, for sample KH_1_2, 0.078 m is the length, 0.003 m^2 is the area, 0.0050 A of is the electrical current, and 10 volt was the electrical potential. Therefore, the resistivity is (10/0.005) × (0.003/0.078) = 86,499 Ohm-m calculated from Equation 2.18.
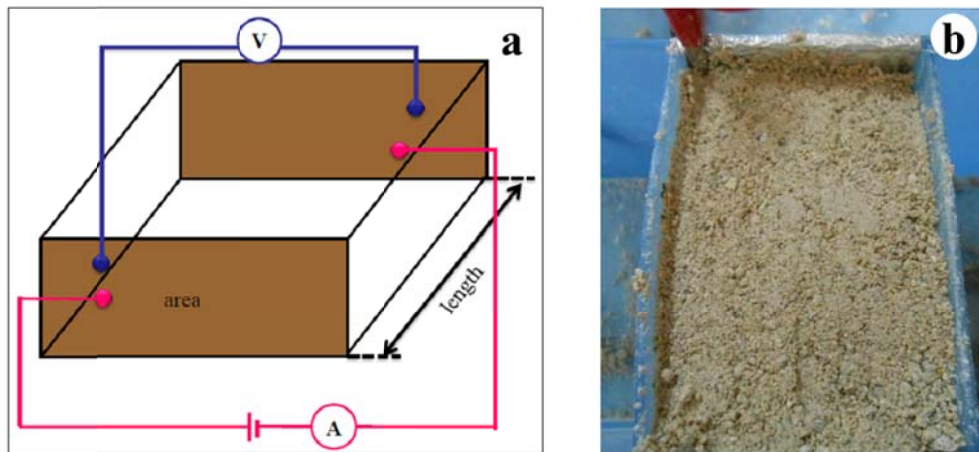
Figure 2.18 (a) Schematic diagram of the electrical laboratory measurements, (b) photo of the sediment samples in the box.

The results of the electrical resistivity were presented in a semi logarithmic plot, where the electrical resistivity was plotted on the log scale, and the water saturation was plotted in arithmetic scale as show in Figure 2.19.
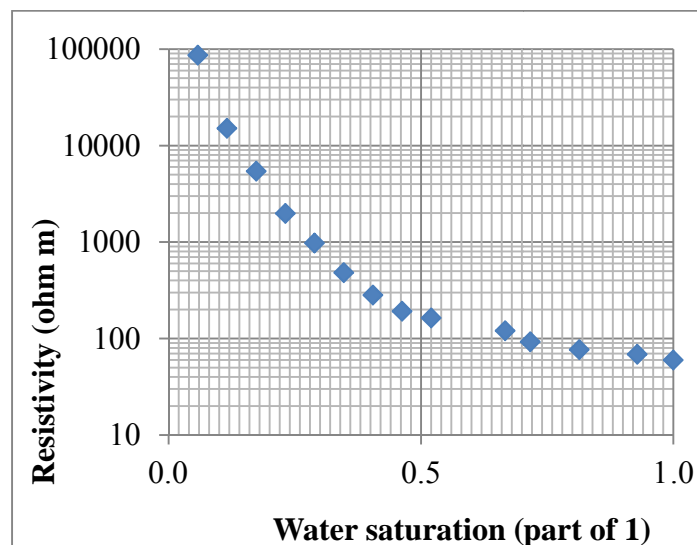
Figure 2.19 Correlation between electrical resistivity and water saturation of KH_1_2.

2.9.2 Electrical resistivity modeling

The resistivity of a saturated porous rock can be expressed by Archie's law (Telford et al., 1990) as below

$$\rho = aS^{-n}\phi^{-m}\rho_w \qquad (2.19)$$

where S is degree of the water saturation, ϕ is porosity, ρ_w is the resistivity of water, m is the tortuosity factor (m are used like porosity exponent, shape factor, or cementation degree), n is saturation exponent, a is the constant (reflects the influence of mineral grains on current flow) (Kirsch, 2006).

For the interpretation of the resistivity data the factors saturation, porosity and clay content (clayey material is characterized by low electrical resistivity) were identified as crucial. For the conductivity of clay bearing sandstones and sediments following model of Sen et al. (1988) has been used, with

$$\sigma = S^n\phi^m a^{-1}[\sigma_w + AQ_v/(1+CQ_v/\sigma_w)] \qquad (2.20)$$

where, σ is soil/sediment conductivity in S/m (σ =1/ρ), S is the degree of the water saturation, ϕ is porosity, σ_w is the conductivity of water, m is the tortuosity factor, n is saturation exponent, a is the constant, A=1.94×m in (S/m)/(mol/l) and C =0.7/Q_v in S/m, Q_v (in mol/l) is the concentration of Na-exchange cations relative to the water saturated pore space, which depends on the cation exchange capacity (C_{ex}) in mol/g and the matrix specific density ρ_m. Q_v replaced by Q^*=Q_v/S (for partial saturation; see Günzel, 1994),

$$Q_v = C_{ex}\rho_m \frac{1-\phi}{\phi} \qquad (2.21)$$

The dependence of the exchange capacity C_{ex} on the relative clay and silt content (mineral composition of clay) P_{clay} and P_{silt} is estimated by a relationship found by Günzel (1994), with

$$C_{ex} = 0.47(P_{clay} + 0.2P_{silt}) \qquad (2.22)$$

For example, Archie's law was used with sample KB_8_2, with 9% degree of the water saturation, 35% porosity, 0.02 Ohm-m resistivity of water, and a, m and n were changed, which moved up or down of the fitted curve. Constant a was kept at 1 if possible, with mainly n and m changed until the laboratory data points and the modeled line overlapped. For this sample, finally, a was 1, m was 2.1 and n was 1.3, with 68,731 Ohm-m resistivity calculated from Equation 2.19 (see Figure 2.20).
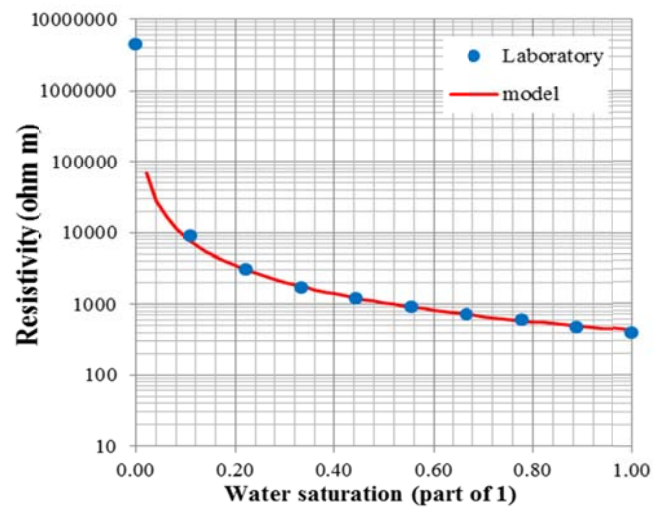
Figure 2.20 Correlation between electrical resistivity and water saturation of KB_8_2, blue circle is resistivity from laboratory and red line is resistivity model using Archie's law.

For example, modified Archie's law was used for sample KH_1_2 with 6% degree of the water saturation, 44% porosity, 0.02 Ωm conductivity of water, A is 1.94×m, 28.9 % P_{clay}, 18.6 % P_{silt}, 2.52 g/cm^3 mineral density, C_{ex} is 0.47 (0.289 + 0.186) = 0.153 calculated from equation 2.22, Q_v is 0.153 × 5.52 ×((1 − 0.44)/0.44) = 0.485 mol/l calculated from Equation 2.21. It was tried to keep a at 1 if possible, with m and n were changed moving up or down the curve until data points and modeled line overlapped (see Figure 2.22 and 2.23). For this this sample a is 1, m is 1.25 and n is 2.55, and with 63,261 Ohm-m of resistivity calculated from equation 2.20 (see Figure 2.21).
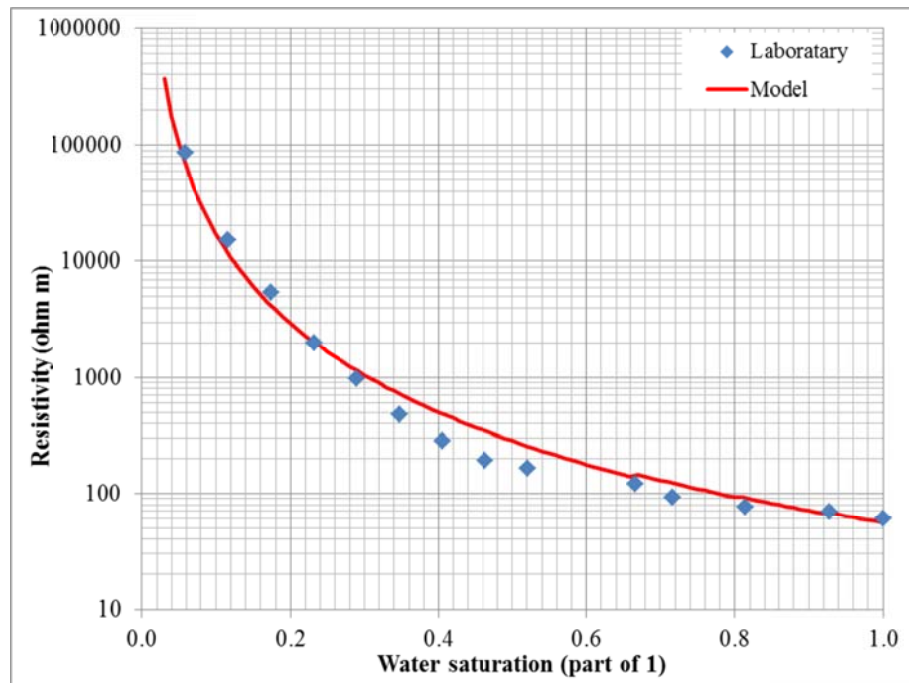
Figure 2.21 Correlation between electrical resistivity and water saturation of KH_1_2, blue circle is resistivity from laboratory and red line is resistivity model calculated using modified Archie's law.
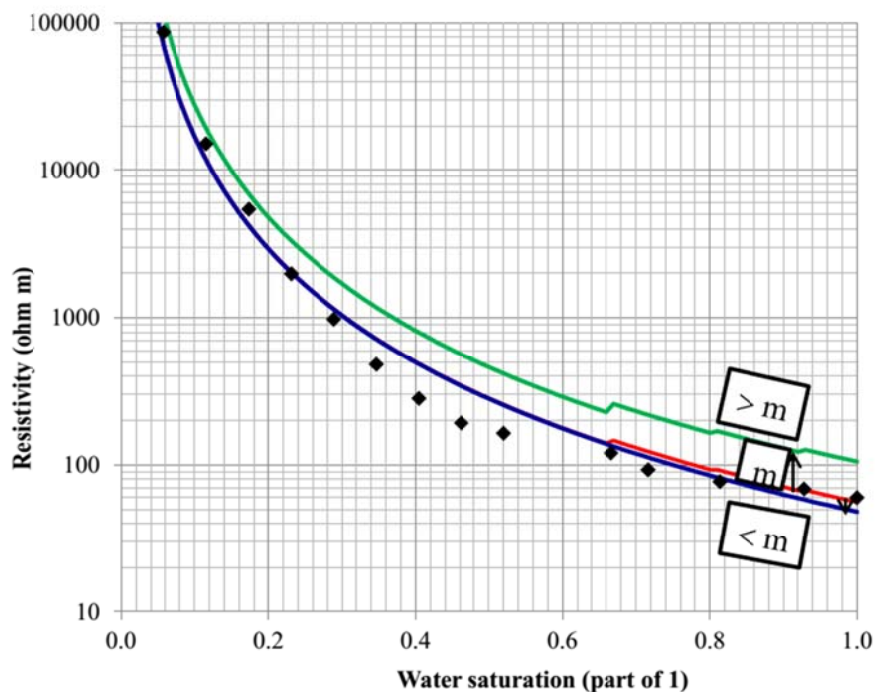
Figure 2.22 Correlation between electrical resistivity and water saturation of KH_1_2, black circle is resistivity from laboratory, red line is the resistivity calculated model

with m=1.25, blue line is the resistivity model when m is lower than 1.25 and the green line is the resistivity model when m is larger than 1.25.
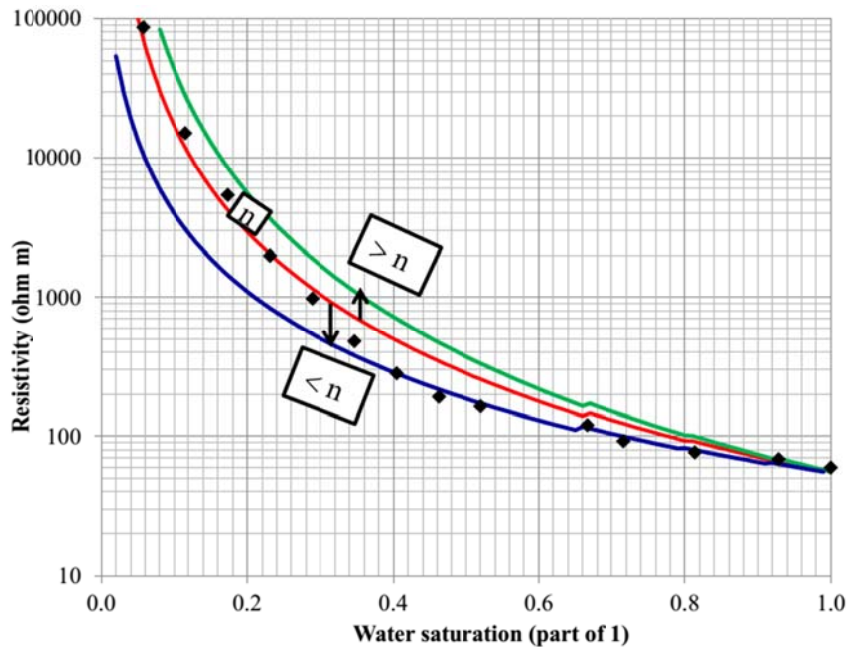
Figure 2.23 Correlation between electrical resistivity and water saturation of KH_1_2, black circle is resistivity from laboratory, red line is resistivity model with n=2.55, blue line is resistivity model when n is lower, and green line is resistivity model when n is higher than 2.55.

2.10 Ultrasonic velocity method

Theory

There are two groups of seismic waves, surface waves and body waves, with the latter ones being utilized in seismic surveys. The velocity of the propagation of body waves, compressional and shear wave velocity, in any solid earth material can be determined as a function of the density (ρ) and the elastic constants of the material.

Compressional waves (the longitudinal, primary or *P*-wave) propagate in the medium in the same direction as the direction of wave propagation, *P*-wave velocity (V_p) is given by

$$V_P = [(k + \tfrac{4}{3}\mu)/\rho]^{\frac{1}{2}} \tag{2.23}$$

where κ is bulk modulus in Pa, μ is shear modulus in Pa, and ρ is density in kg/m^3.

Shear waves (transverse, secondary or *S*-wave) propagate in the medium in the direction perpendicular to the direction of wave travel, *S*-wave velocity (V_s) is given by

$$V_S = (\mu / \rho)^{\frac{1}{2}} \qquad (2.24)$$

Compressional waves always travel faster than shear wave in the same medium and shear waves do not propagate through the liquids and gases because liquids and gases offer no resistance to shear deformation, so $\mu = 0$ (Sheriff and Geldart 1995).

Ultrasonic velocity method is a non-destructive testing method based on measuring the velocity. The velocity of these waves traveling in a solid material depends on the density, porosity and elastic properties of the material. Ultrasonic has two piezoelectric sensors coupled to the object at constant pressure. One of the transducers is stimulated using an ultrasonic pulser and the other is used as a receptor sensor. This method measures the propagation wave characteristics induced by microstructural factors. Compressional wave velocity (V_P) and shear waves velocity (V_S) were measured using polarized parametric which acquired and digitalized waveforms to be displayed manipulated and stored the data. The transducer is contact with the sample so that the vibrations are transferred to the sample. The wave travel through the sample and are picked up by the receiver show in Figure 2.24.
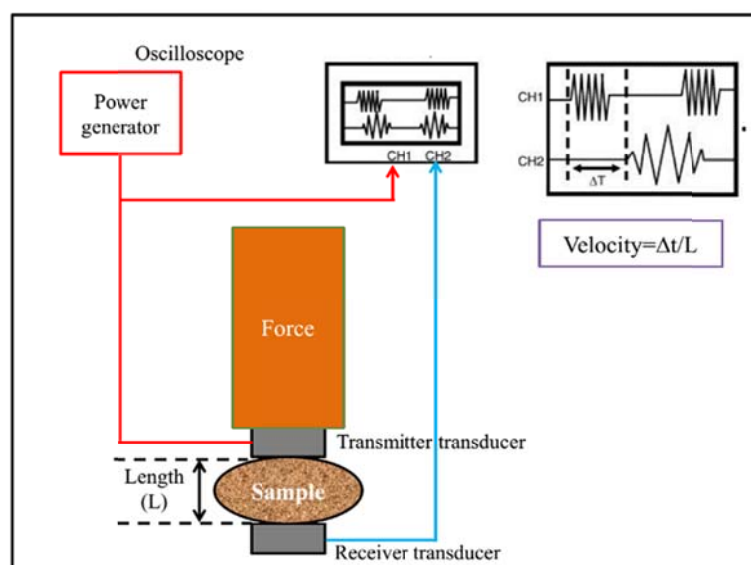
Figure 2.24 Schematic diagrams of the seismic laboratory measurements.

Methodology

For the seismic laboratory measurements transducers with 63 kHz for the P-wave and 33 kHz for the S-waves were used, together with Sonic Viewer-170, OYO, using a uniaxial pressure of 0.122 MPa for better contact as shown in Figure 2.25. First, the sediment sample was in a plastic bag which had holes so that any excessive air or water could flow out, by this avoiding any build-up of pore pressure. The sample as placed between the transducers and from this the sample length was determined. Weight was placed on the top transducers to increase the vertical pressure aiming to get clear signals.

Next, Sonic Viewer-170 was connected with power supply, set the power switch on, connected the Sonic Viewer-170 to P-wave transducer. The gain was set at 10-50, filter was set as high cut 1 MHz and low cut 30 KHz, no pre-trigger was used, the sampling range was100-500 nano sec. Before the sample was set up the determination of the zero point is required. Here the transducers were set on each other, a measurement was taken and the cursor key was moved to the position of the first break and by this fixing the time as zero point. Then, the transducers were connected to the samples as illustrated in Figure 2.25 and the P-wave velocity was measured by identifying the first break. For S wave transducer as similar procedure was carried out. Here the gain was 50-500, the filter a high cut 200 kHz and low cut 500 Hz,no pre-trigger, and a sampling range of 100-500 nano sec. The ultrasonic velocity was determined under laboratory conditions with increasing water saturation from 0 to 100% of the sample in 6-12 steps. The wave velocity is calculated by using the time taken by the pulse to travel the measured distance between the transmitter and the receiver. The pulse velocity is given by the formula

$$v = \frac{s}{t} \tag{2.25}$$

where, v is velocity (km/s), s is length of sample (cm) and t is delta time (μs). For example, V_P of KH_1_2, 39.56 cm distance, 58.50 μs time, 767 km/s of V_P. This method was done at the School of Geotechnology, Institute of Engineering, Suranaree University of Technology, in Nakhon Ratchasima. Uncertainty comes with the identification of the first break by moving the cursor key in discrete steps. One step in the cursor results in different velocities. For example, V_P of KB_7_2, 80.0 μs time at the first break gives 516 km/s for V_P, whereas for the step 78.0 μs time 530 km/s of V_P will be calculated. The difference is small.
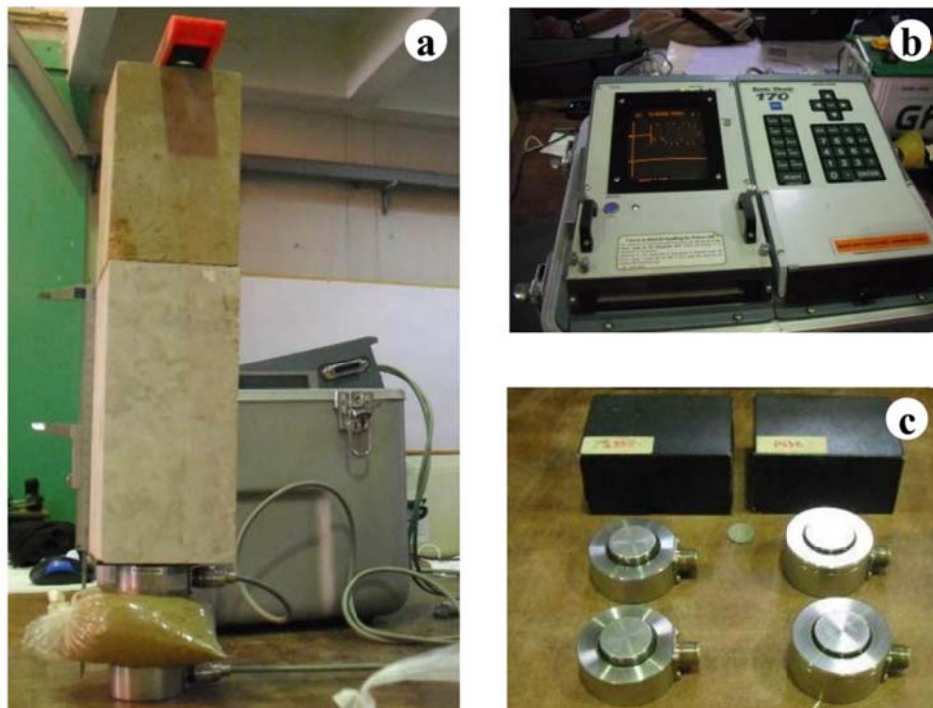
Figure 2.25 (a) Equipment set up in laboratory, (b) Sonic Viewer-170, (c) transducers 63 kHz of P wave and 33 kHz of S waves.

2.11 Elastic analysis

Theory

The elastic properties of substances are characterized by elastic modulus or constants which specify the relation between the stress and the strain. A stress is measured as force per unit area, a compressive stress if it acts perpendicular to the area and a shear stress if it acts parallel to it. A system of compressive stresses changes the volume but not the shape of a body; one of shear stresses changes the shape but not the volume. The strains in a body are deformations which produce restoring forces opposes to the stresses. Tensile and compressive stresses give rise to longitudinal and volume strains which are measured as angle of deformation. It is usually assumed that the strains are small and reversible, that is, a body resumes its original shape and size when the stresses are relieved. Hooke's law states that the stress is proportional to the strain, the constant of proportionality being known as the elastic modulus or elastic constant.

The main two elastic constants for studying elastic wave propagation in the earth are the bulk modulus (κ) and the shear modulus (μ). Shear modulus denoted by G, or S, or μ, is defined as the ratio of shear stress to the shear strain, unit is the Pascal (Pa).

$$\mu = \frac{F/A}{\Delta x/l} = \frac{Fl}{A\Delta x} \tag{2.26}$$

where F is the force which acts, A is area on which the force acts, Δx is transverse displacement, l is initial length. The bulk modulus B or k of a substance measures the substance's resistance to uniform compression. It is defined as the ratio of the infinitesimal pressure increase to the resulting relative decrease of the volume. Its SI unit is the Pascal,

$$k = \frac{\Delta P}{\Delta V/V} \tag{2.27}$$

where, ΔP is the pressure change, ΔV is the volume change, and V is the volume.

Methodology

From the velocity and bulk density the elastic moduli can be calculated, where V_P is the compressional (P) wave velocity in m/s, V_S is shear (S) wave velocity in m/s, and ρ is the density in kg/m³ (Sheriff and Geldart, 1995), as following

Young's modulus (*E)*

$$\rho V_S^{\;2}\left(\frac{3V_P^{\;2}-4V_S^{\;2}}{V_P^{\;2}-V_S^{\;2}}\right) \tag{2.28}$$

Poisson's ratio (σ)

$$\frac{V_P^{\;2}-2V_S^{\;2}}{2(V_P^{\;2}-V_S^{\;2})} \tag{2.29}$$

Bulk modulus (*k)*

$$\rho\left(V_P^{\;2}-\frac{4}{3}V_S^{\;2}\right) \tag{2.30}$$

Shear modulus (μ)

$$\rho V_S^{\;2} \tag{2.31}$$

For example, the elastic modulus of KH_1_2 with 676 m/s P wave velocity, 261 m/s S wave velocity, 1.35 g/cm³ bulk density at 0% water saturation, the Young's modulus is 259 MPa from Equation 2.25, the Poisson's ratio is 0.46 MPa from Equation 2.26, the bulk modulus is 495 MPa from Equation 2.27, and the shear modulus is 92 MPa from Equation 2.28.

3. Results and Discussion

3.1 Fieldwork

For this study unconsolidated sediments from difference layers from bedrock to the top soil layer were taken from two location of the Khao Khohong mountain range in Hat Yai District, Songkhla Province. The two sample locations comprise different bedrock lithology; the first location is mainly granite at a mountain site in different states of weathering show in Figure 3.1. Granite intrusion in local rock, some area is hornfels and some area is granite.
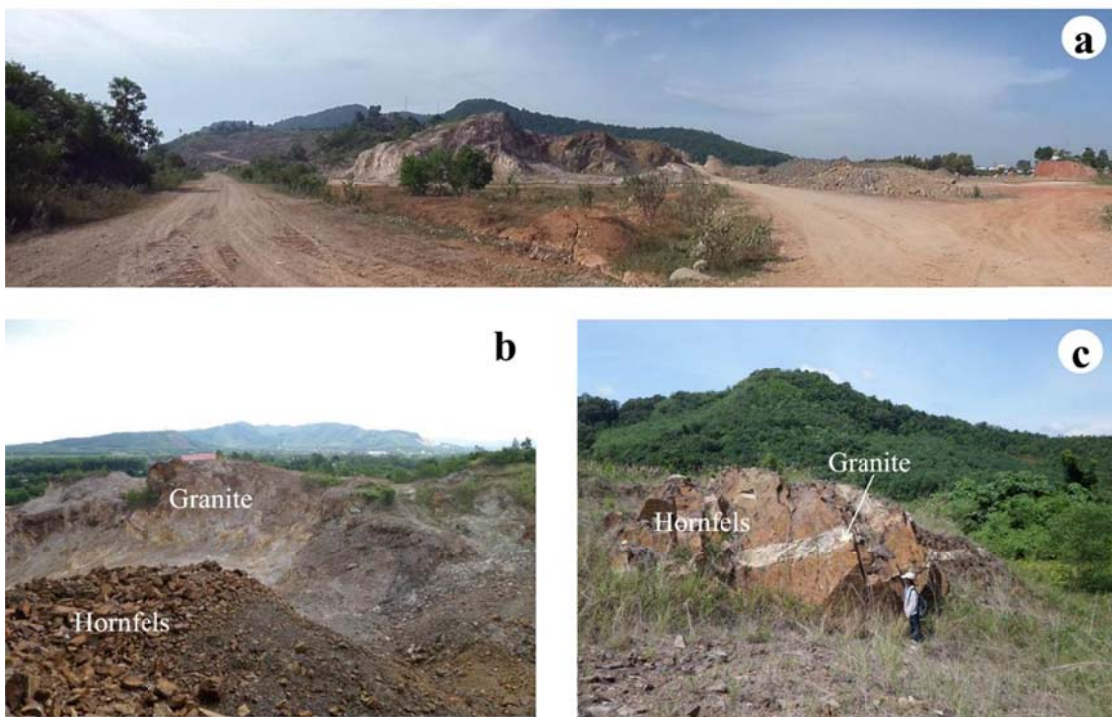
Figure 3.1 (a) Location with mainly granite, view to NE (b) out crop of granite and hornfels, (c) granite intrusion in hornfels.

The second location is mainly sandstone with different layers from bedrock to top soil show in Figure 3.2; this area is east of Prince of Songkla University. Outcrop had three maim layer, top layer is topsoil; they are organic matter giving them a darker color. Second layer is unconsolidated sediments, they are clay, silt, sand, gravel and rock fragment, and bottom layer is bedrock, sandstone and red mudstone.

Figure 3.2 Location with mainly sandstone. View to North.

Layering in the outcrop is dipping east to southeast; field measurements with a compass given 120/30 P, 110/30 P, and 128/30 P (dip direction/dip angle/plane). Faults and joints dipping north to west, with compass values of 270/60 P, 275/75 P, 270/55 P, 008/70 P, 295/57 P, and 342/85 P. Data are shown in Stereo Net plot by Stereo Net version 2.03 shows in Figure 3.3 as pole points or normal of the planes.
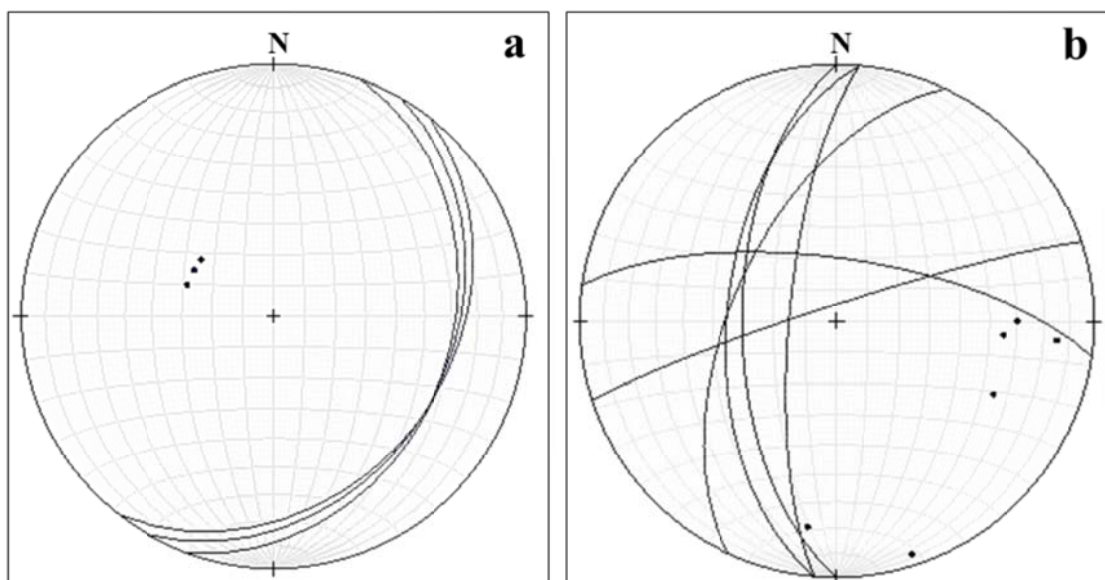
Figure 3.3 Stereo Net plot, lower hemisphere, of (a) the layering, and of (b) faults and joints of the sandstone site. For each plane great circle and pole is shown.

3.2 Sample description

     Altogether 21 sediment samples were collected at both sites; nine samples from the area with mainly granite shown in Figure 3.4 and 3.5 and listed in Table 3.1, and 12 samples the sandstone site shown in Figure 3.6 and 3.7 and listed Table 3.2.
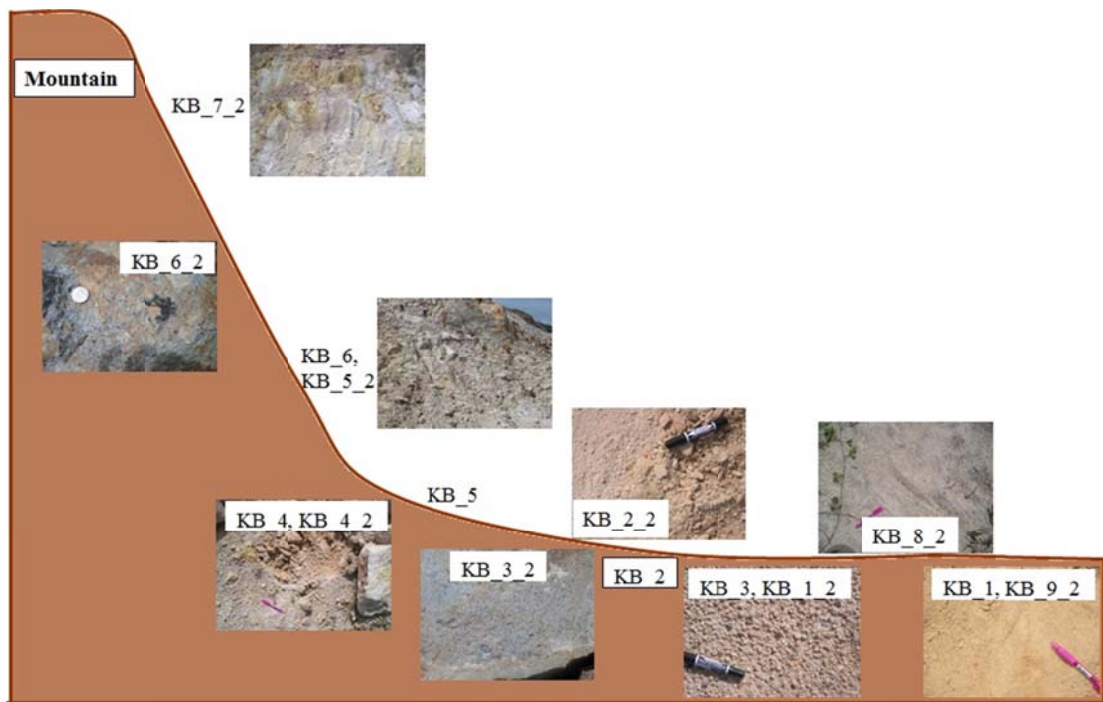
Figure 3.4 Photos of the sediment samples from the granite location and their location relative to the mountain.

Table 3.1 Sediment samples from main granite location.

UTM	Location	Name Sample		Type
		Sampling 1	Sampling 2	
0666806 0779853	Mountain		KB_7_2	sediment
	Foothill	KB_6	KB_5_2	sediment
			KB_6_2	rock
0666802 0779972	Below the mountain	KB_2		sediment
		KB_4	KB_4_2	sediment
		KB_5		sediment
			KB_2_2	sediment
			KB_3-2	weathered granite
0667044 0780058 0666795 0779991	Surface (on the way)	KB_1	KB_9_2	soil (sand)
		KB_3	KB_1_2	sediment
			KB_8_2	sediment

     The sediment samples from the granite site comprise samples from the mountain where the granite rock (KB_6_2) is already weathered and not a rock anymore (KB_5_2 and KB 6_2), see also Figure 3.4. Further samples are mainly

weathering products of the granite that are already transported some distance of up to about 100 m from the mountain (see Table 3.1).
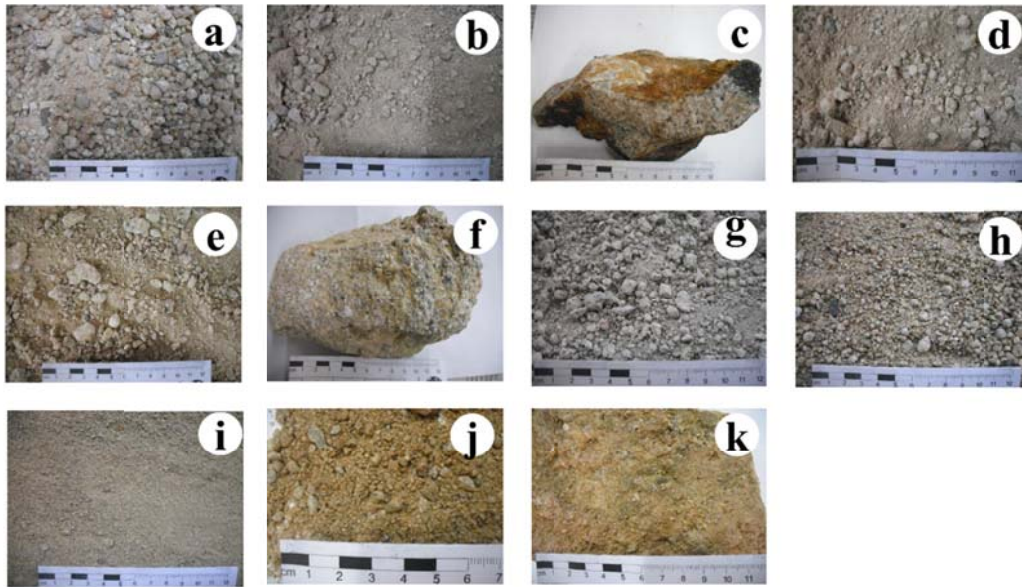
Figure 3.5 Photos of the sediment samples from main granite location; sample (a) KB_1_2, (b) KB_2_2, (c) KB_3_2, (d) KB_4_2, (e) KB_5_2, (f) KB_6_2, (g) KB_7_2, (h) KB_8_2, (i) KB_9_2, (j) KB_2, and (k) KB_5.

The macroscopic color of the samples shown in Figure 3.5 vary between mainly gray to ochre (e.g. Figure 3.5j and k). The grain size visible varies between the samples, mainly due to their location in relation to the mountain and as the result of transport phenomena. For example, sample KB_9_2 (Figure 3.5i) has macroscopically almost no larger grain and this sample has the furthest distance from the mountain (see Figure 3.4). In sample KB_1_2 (Figure 3.5a) quartz grain are clearly visible as they are relatively inert to chemical weathering. The grain shape of these minerals is relatively rough with almost no signs of abrasion indication a very short transportation distance from the source, which is in agreement with the sampling location relative to the mountain.
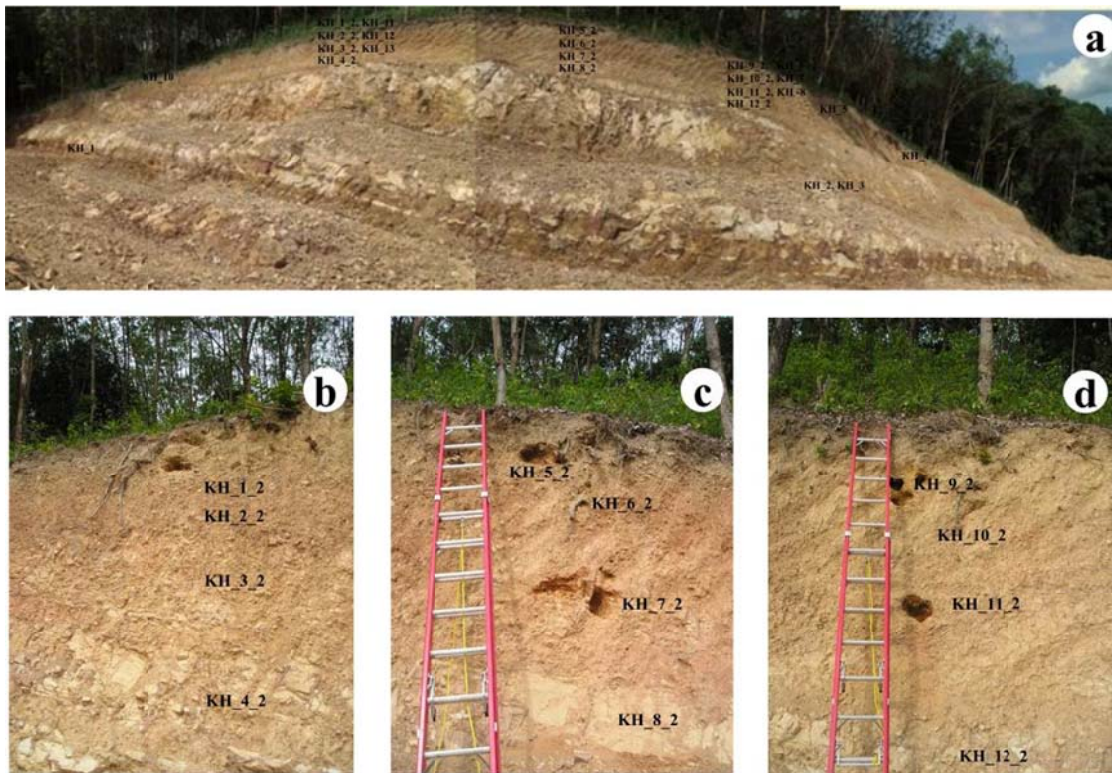
Figure 3.6 Photos of the sediment samples from the sandstone site. a) provides an overview of the site, view to West; whereas b) to d) are detailed images of the sample locations.

Table 3.2 Sediment samples the sandstone site.

Location		Name Sample		Type
		Sampling 1	Sampling 2	
Left profile	Top soil	KH_10	KH_1_2	soil
	Yellow gravel layer	KH_11	KH_2_2	sediment
	Sediment layer	KH_12	KH_3_2	sediment
	Soft rock	KH_13		sediment
	Hard rock		KH_4_2	rock
Central profile	Top soil		KH_5_2	soil
	Yellow gravel layer	KH_6	KH_6_2	sediment
	Sediment layer	KH_7	KH_7_2	sediment
	Soft rock	KH_8		sediment
	Hard rock		KH_8_2	rock
Right profile	Top soil		KH_9_2	soil
	Yellow gravel layer	KH_5	KH_10_2	sediment
	Sediment layer		KH_11_2	sediment
	Hard rock		KH_12_2	rock
Deeper	N of hard rock	KH_1		red mudstone
	S of hard rock	KH_2		sandstone
	S of hard rock	KH_3		sandstone
	Next to KH_2,3 (south)	KH_4		sandstone
On the way	Slope mountain	KH_9		hornfels
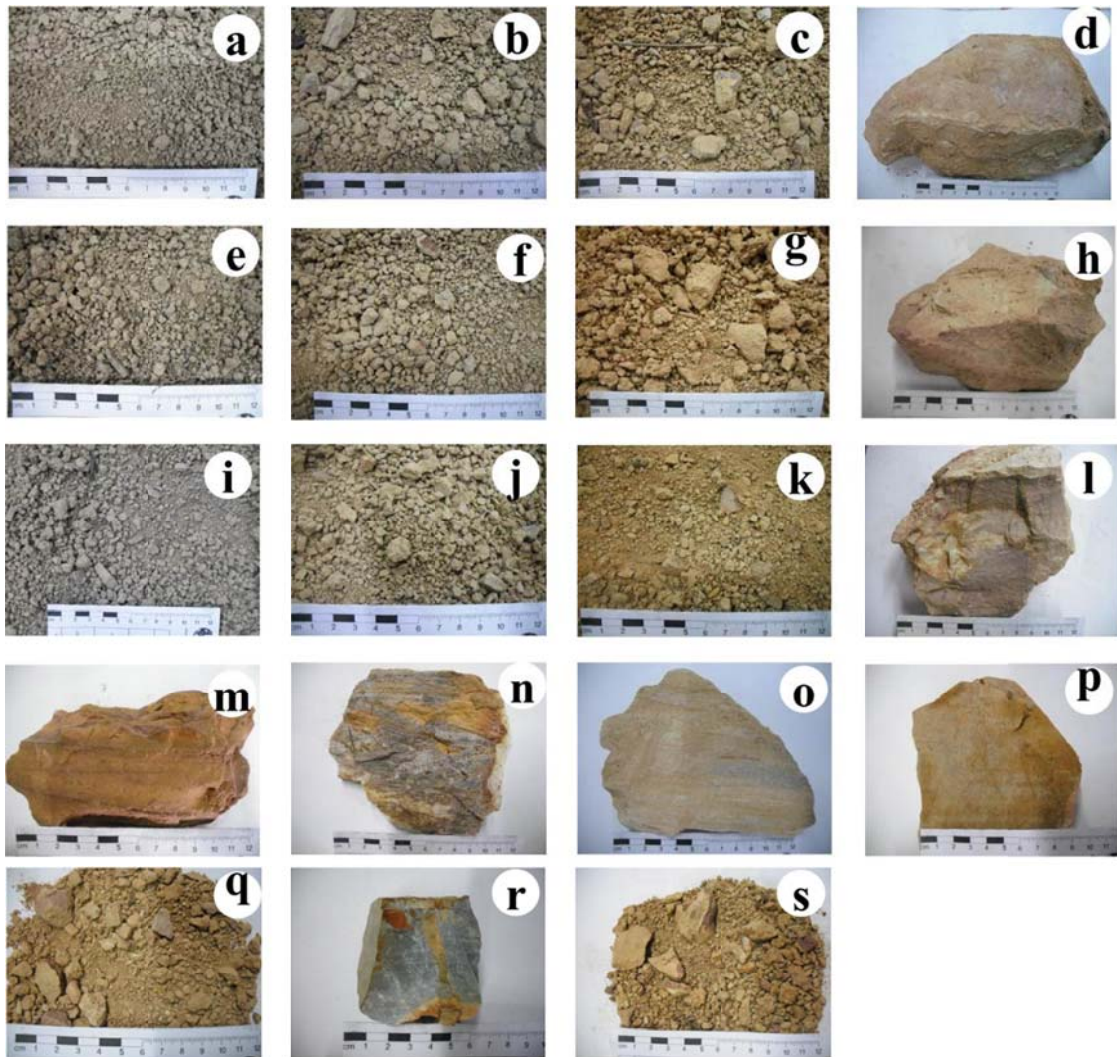
Figure 3.7 Photos of the sediment samples from main granite location; sample (a) KH_1_2, (b) KH_2_2, (c) KH_3_2, (d) KH_4_2, (e) KH_5_2, (f) KH_6_2, (g) KH_7_2, (h) KH_8_2, (i) KH_9_2, (j) KH_10_2, (k) KH_11_2, (l) KH_12_2, (m) KH_1, (n) KH_2, (o) KH_3, (p) KH_4, (q) KH_8, (r) KH_9 and (s) KH_13.

The sediment samples from the sandstone site are all weathering products of the underlying sandstone (e.g., sample KH_4_2, see Table 3.2). The regolith above the hardrock shows macroscopically different layers as the result of the weathering and near surface processes. The differences are mainly visible through changes in color and texture, as larger grain sizes decreases until the surface. The top soil (e.g. KH_1_2, see Table 3.2) is clearly visible through the darker color as the result of decomposed organic material. The thickness of the samples varies at the different locations inside the outcrop. At the third sample site, KH_9_2 to KH_12_2 the upper

two layers show some syncline shape as the result of a small "river" bed oriented perpendicular to the outcrop face (Figure 3.6d).

Roots from plants and trees are found from the top down into the hardrock, although the number decreases towards the hardrock. The outcrop area has tree vegetation with in-between smaller plants. At three different locations inside the outcrop samples from the different layers were taken (see Figure 3.6), usually four samples including the underlying hardrock (Table 3.2). A few other samples were taken at other locations indicated in Figure 3.6a.

The samples from the sandstone site also have grey to ochre color as shown in Figure 3.7. The macroscopically visible "grain" size varies related to the sample location; however they are more aggregates than single grains. The size of the aggregates can be a few centimeters. No quartz minerals are visible like in the samples from the granite site.

3.3 Density and Porosity

The values of the mineral density of the samples from the granite site are around 2.5 to 2.6 g/cm^3 (Figure 3.8), which reflects the main minerals with quartz (2.648 g/cm^3), Kaolinite (2.594 g/cm^3) and Illite (2.660 g/cm^3) (see Section 3.5; data from Schön, 2011). The bulk density values are much smaller, around 1.5-1.8 g/cm^3, thus reflecting the porosity of the samples with 30 to 40%, which is common for such sediments (e.g. Schön, 2011). Higher bulk density correlates with lower porosity values and vice versa (Figure 3.8).
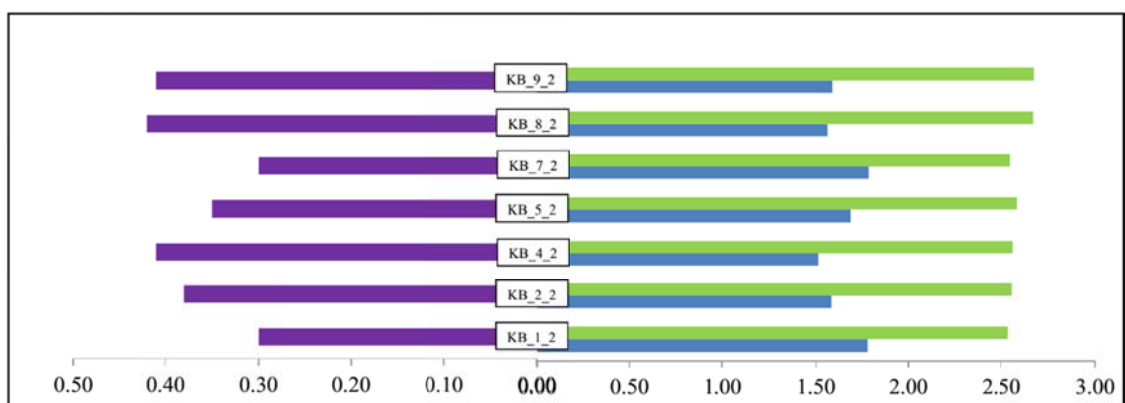
Figure 3.8 Granite site: density and porosity of the samples; green: mineral density (in g/cm^3), blue: bulk density (in g/cm^3), and purple: porosity (%).
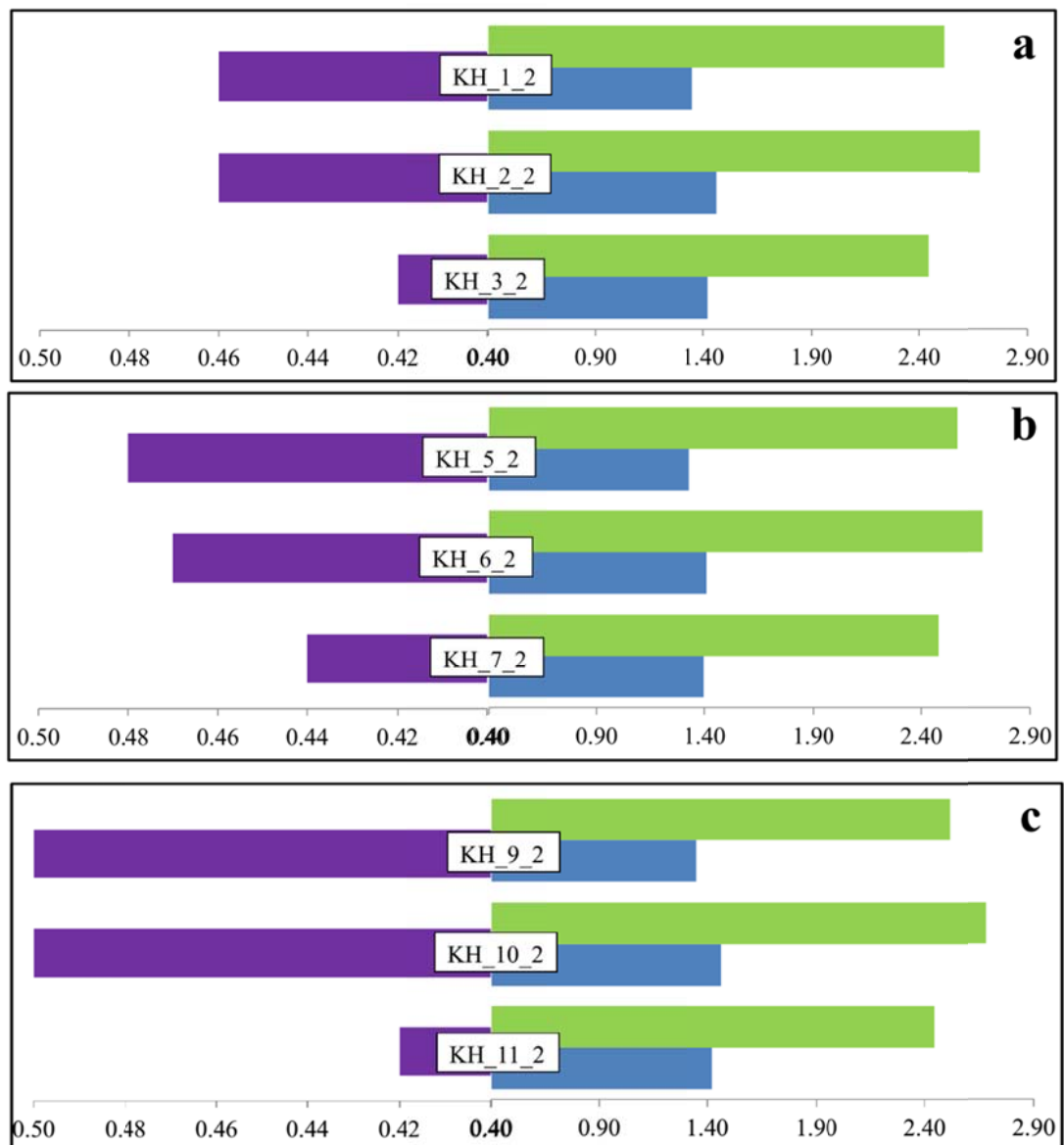
Figure 3.9 Sandstone site: density and porosity of the samples; green: mineral density (in g/cm^3), blue: bulk density (in g/cm^3), and purple: porosity (%). a, b, and c reflect the three profiles in the outcrop with samples from top to bottom.

The values of the mineral density of the samples from the sandstone site are around 2.45 to 2.68 g/cm^3 (Figure 3.9), which here also reflects the main minerals with quartz (2.648 g/cm^3), Kaolinite (2.594 g/cm^3) and Illite (2.660 g/cm^3) (see Section 3.5; data from Schön, 2011). The bulk density values are much smaller, around 1.3-1.5 g/cm^3, thus reflecting the porosity of the samples with 42 to 50%, which is common for such sediments (e.g. Schön, 2011). Higher bulk density correlates with lower porosity values and vice versa (Figure 3.9), however it is not always clear. At all three sites the porosity of the upper two layers are much higher

than of the third layer indicating that the weathering process increases the porosity and thus decreasing the bulk density.

3.4 Grain size distribution

The grain size distribution curves of the samples from the granite site are shown in Figure 3.10 and 3.11. All seven samples show a similar curve type, however the ratio of gravel to sand to silt and to clay changes. The main part of all samples is sand, and they all show a clear fine (silt, clay) part, except sample KB_8_2.

The samples from the sandstone site are shown in Figure 3.12 to 3.14. Each figure presents one location with three different layers from top to bottom. The shape of the grain size distribution curves for these samples are different than for the samples from the granite site. This is the result of a larger clay content of these samples, and therefore thus reducing the part of sand and silt.

For all three sites the grain size distribution shows a trend towards smaller grain sizes from the bottom to the top layer. At two sites the gravel part gets a larger portion for the bottom layers (Figure 3.12 and 3.14). As the gravel portion of the top layer was reduced the sand part gained mainly from it; whereas the clay part remains almost the same for all three layers. This change in grain size distribution reflects well the weathering of the sandstone, as through these processes the grain size reduces from bottom to the top.
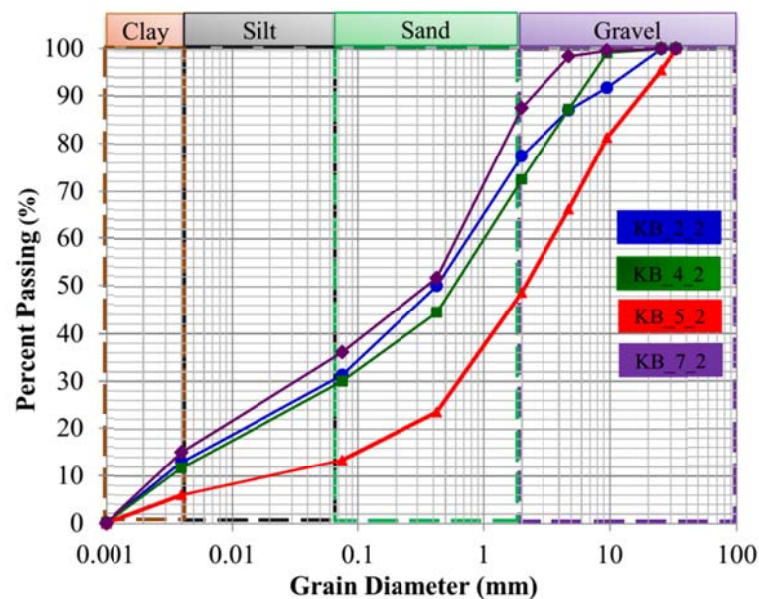
Figure 3.10 Granite site: Grain size distribution; blue- KB_2_2, green - KB_4_2, red - KB_5_2, and purple - KB_7_2.
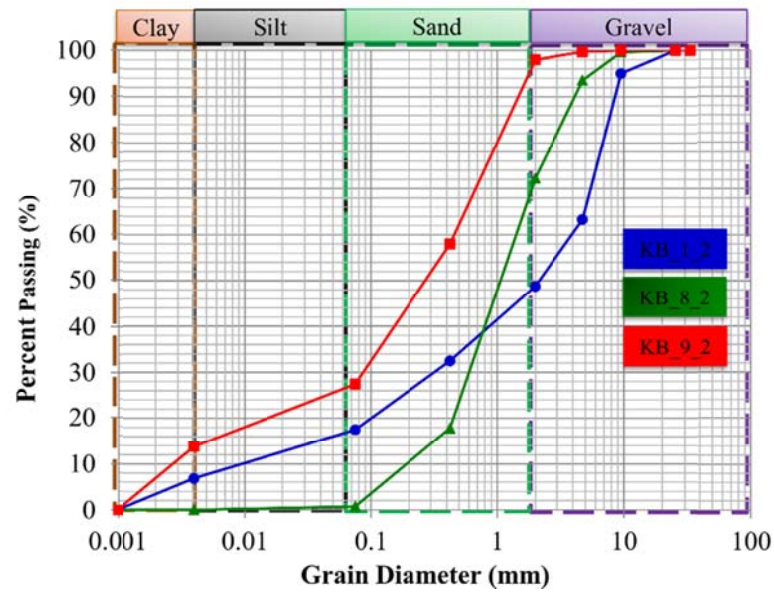
Figure 3.11 Granite site: Grain size distribution, blue - KB_1_2, green - KB_8_2, and red - KB_5_2.
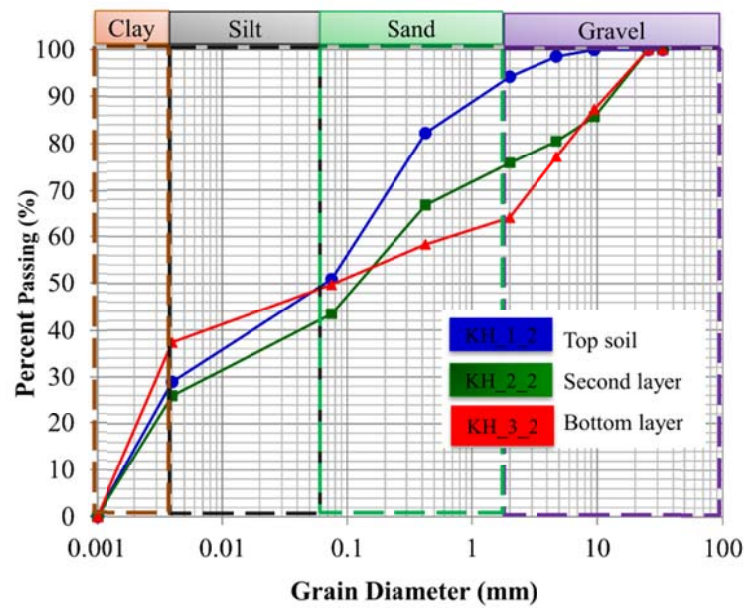
Figure 3.12 Sandstone site: Grain size distribution; blue - KH_1_2, green - KH_2_2, and red - KH_3_2.
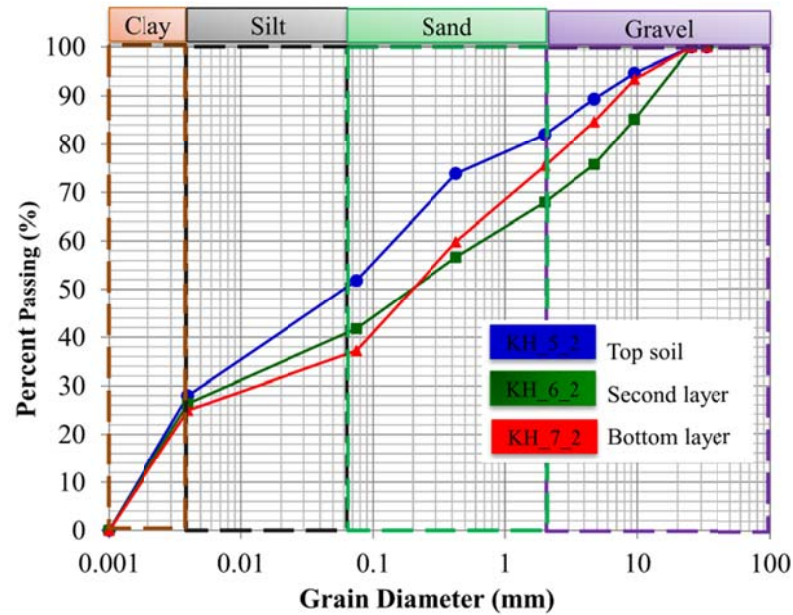
Figure 3.13 Sandstone site: Grain size distribution, blue - KH_5_2, green - KH_6_2, and red - KH_7_2.
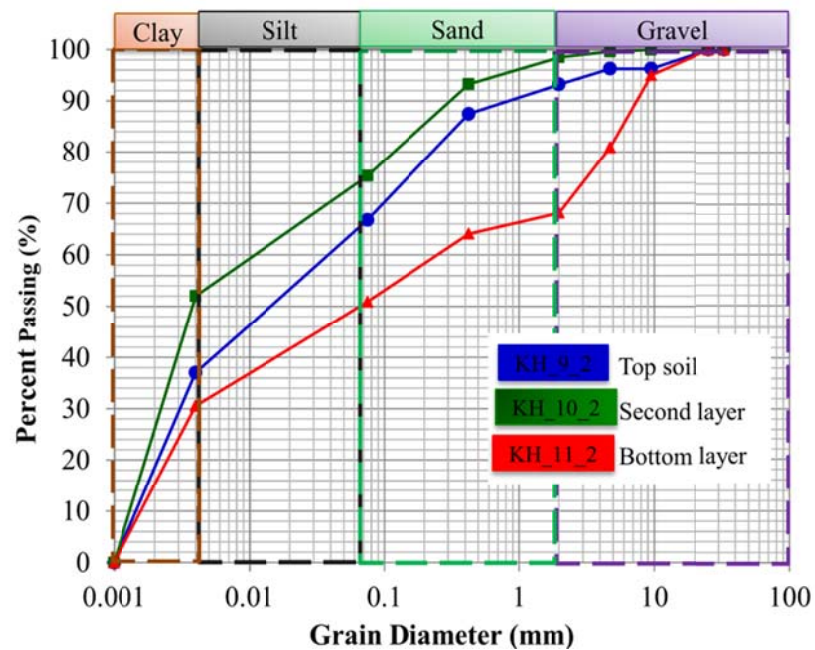
Figure 3.14 Sandstone site: Grain size distribution, blue - KH_9_2, green - KH_10_2, and red - KH_11_2.

With the data from the grain size distribution a texture analysis of the soil samples can be done using the triangle of sand, silt, and clay (see USDA, 1987); note that the gravel part is not used and therefore the three values change accordingly as

their sum must be 100. The data for the samples from the granite site are plotted in Figure 3.15. Samples here are in the field of sand and mainly sandy loam. Therefore, despite different weathering or transportation stages most of the samples still remain in the same field.
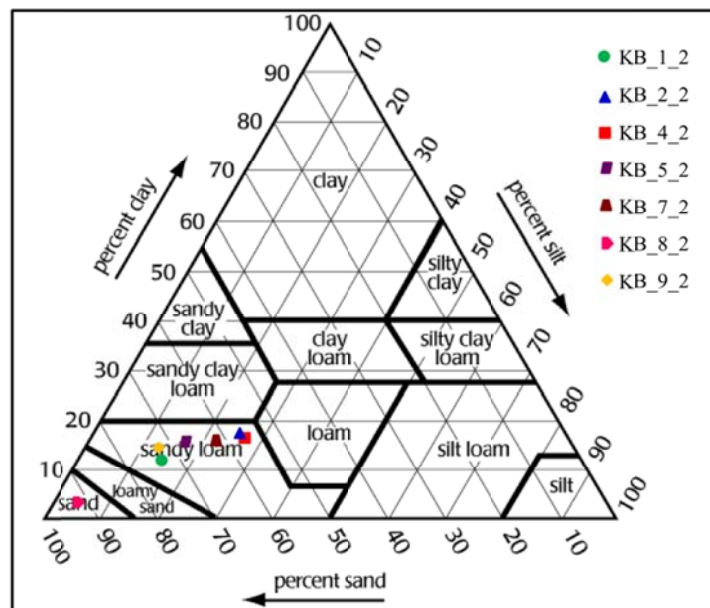
Figure 3.15 Triangle with the textural classification of main granite.
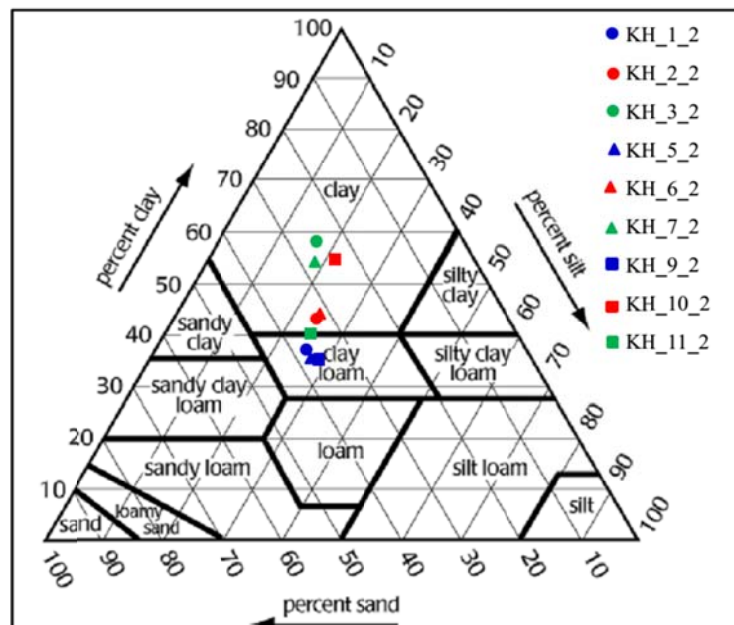
Figure 3.16 Triangle with the textural classification of main sandstone.

The textural classification of the samples from the sandstone site shows mainly clay loam to clay samples (Figure 3.16). Interesting here to observe is that samples from the top layer all plot in the clay loam filed. The middle and bottom layers are all in the clay field. This is due to the fact that gravel is not part of this diagram (see above).

3.5 Composition

The XRD-derived composition of the samples is listed in Table 3.3 for all samples from both sites, granite (KB) and sandstone site (KH). The main minerals are quartz and several clay minerals, kaolinite, illite, and montmorillonite. In one sample hematite was found (KH-13). The clay minerals are the products of chemical weathering of mainly feldspar minerals in the granite and in the sandstone as well.

Table 3.3 Composition of unconsolidated sediment samples from XRD.

Sample Name	JCPDF No.	Chemical Name	Chemical Formula
KB_1_2	01-085-0798	Quartz	SiO_2
	01-078-1996	Kaolinite 1\ITA\RG	$Al_2(Si_2O_5)(OH)_4$
	00-026-0911	Illite-2\ITM\RG#1[NR]	$(K,H_3O)Al_2Si_3AlO_{10}(OH)_2$
KB_4_2	01-085-0504	Quartz	SiO_2
	01-080-0885	Kaolinite 1\ITA\RG	$Al_2(Si_2O_5)(OH)_4$
	00-026-0911	Illite-2\ITM\RG#1[NR]	$(K,H_3O)Al_2Si_3AlO_{10}(OH)_2$
	00-007-0330	Illite-Momtmorillonite, regular	$K-Al_4(SiAl)_8O_{20}(OH)_4 \cdot xH_2O$
KB_5_2	03-065-0466	Quartz low, syn	SiO_2
	01-080-0886	Kaolinite 1\ITA\RG	$Al_2(Si_2O_5)(OH)_4$
	00-026-0911	Illite-2\ITM\RG#1[NR]	$(K,H_3O)Al_2Si_3AlO_{10}(OH)_2$
KB_9_2	01-085-0796	Quartz	SiO_2
	01-076-0918	Microcline maximum	$KAlSi_3O_8$
	00-026-0911	Illite-2\ITM\RG#1[NR]	$(K,H_3O)Al_2Si_3AlO_{10}(OH)_2$
KB_2	01-085-0796	Quartz	SiO_2
	01-089-6538	Kaolinite Illite-2\ITM\RG#1[NR]	$Al_2(Si_2O_5)(OH)_4$
	00-026-0911		$(K,H_3O)Al_2Si_3AlO_{10}(OH)_2$
KB_5	03-065-0466	Quartz low, syn	SiO_2
	01-080-0886	Kaolinite 1\ITA\RG	$Al_2(Si_2O_5)(OH)_4$
	00-026-0911	Illite-2\ITM\RG#1[NR]	$(K,H_3O)Al_2Si_3AlO_{10}(OH)_2$

Table 3.3 Composition of unconsolidated sediment samples (cont.).

KH_1_2	01-085-1053	Quartz, syn	SiO_2
	01-080-0886	Kaolinite 1\ITA\RG	$Al_2(Si_2O_5)(OH)_4$
KH_2_2	01-078-2315	Quartz	SiO_2
	01-080-0886	Kaolinite 1\ITA\RG	$Al_2(Si_2O_5)(OH)_4$
	00-026-0911	Illite-2\ITM\RG#1[NR]	$(K,H_3O)Al_2Si_3AlO_{10}(OH)_2$
KH_3_2	01-085-0504	Quartz	SiO_2
	00-026-0911	Illite-2\ITM\RG#1[NR] Kaolinite	$(K,H_3O)Al_2Si_3AlO_{10}(OH)_2$
	01-080-0886	1\ITA\RG	$Al_2(Si_2O_5)(OH)_4$
KH_6_2	01-083-2565	Quartz, syn	SiO_2
	01-080-0885	Kaolinite 1\ITA\RG	$Al_2(Si_2O_5)(OH)_4$
	00-026-0911	Illite-2\ITM\RG#1[NR]	$(K,H_3O)Al_2Si_3AlO_{10}(OH)_2$
KH_7_2	01-085-1053	Quartz, syn	SiO_2
	01-080-0885	Kaolinite 1\ITA\RG	$Al_2(Si_2O_5)(OH)_4$
KH_10_2	01-085-0504	Quartz, syn	SiO_2
	01-080-0885	Kaolinite 1\ITA\RG	$Al_2(Si_2O_5)(OH)_4$
KH_1	01-083-2465	Quartz low, syn	SiO_2
	01-089-6538	Kaolinite	$Al_2(Si_2O_5)(OH)_4$
	00-026-0911	Illite-2\ITM\RG#1[NR]	$(K,H_3O)Al_2Si_3AlO_{10}(OH)_2$
KH_2	01-079-1910	Quartz, syn	SiO_2
	01-080-0885	Kaolinite 1\ITA\RG	$Al_2(Si_2O_5)(OH)_4$
KH_3	01-086-1560	Quartz low	SiO_2
	01-089-6538	Kaolinite	$Al_2(Si_2O_5)(OH)_4$
KH_4	01-087-2096	Quartz low	SiO_2
	01-080-0886	Kaolinite 1\ITA\RG	$Al_2(Si_2O_5)(OH)_4$
	00-026-0911	Illite-2\ITM\RG#1[NR]	$(K,H_3O)Al_2Si_3AlO_{10}(OH)_2$
KH_8	01-087-2096	Quartz low	SiO_2
	01-080-0885	Kaolinite 1\ITA\RG	$Al_2(Si_2O_5)(OH)_4$
KH_9	01-083-2465	Quartz low, syn	SiO_2
KH_13	01-085-0504	Quartz	SiO_2
	00-073-2234	Hematite	Fe_2O_3
	01-080-0885	Kaolinite 1\ITA\RG	$Al_2(Si_2O_5)(OH)_4$

3.6 Microstructures

With the SEM microstructures of the samples were observed and shown in Figure 3.17a-i to 3.20a-f, with samples dry shown in Figure 3.17a-i to 3.19 a-i and

after full saturation with water in Figure 3.20. In the SEM pictures clay minerals (C), quartz (Q) and pores (P) were identified as well as the overall arrangement of the grains.
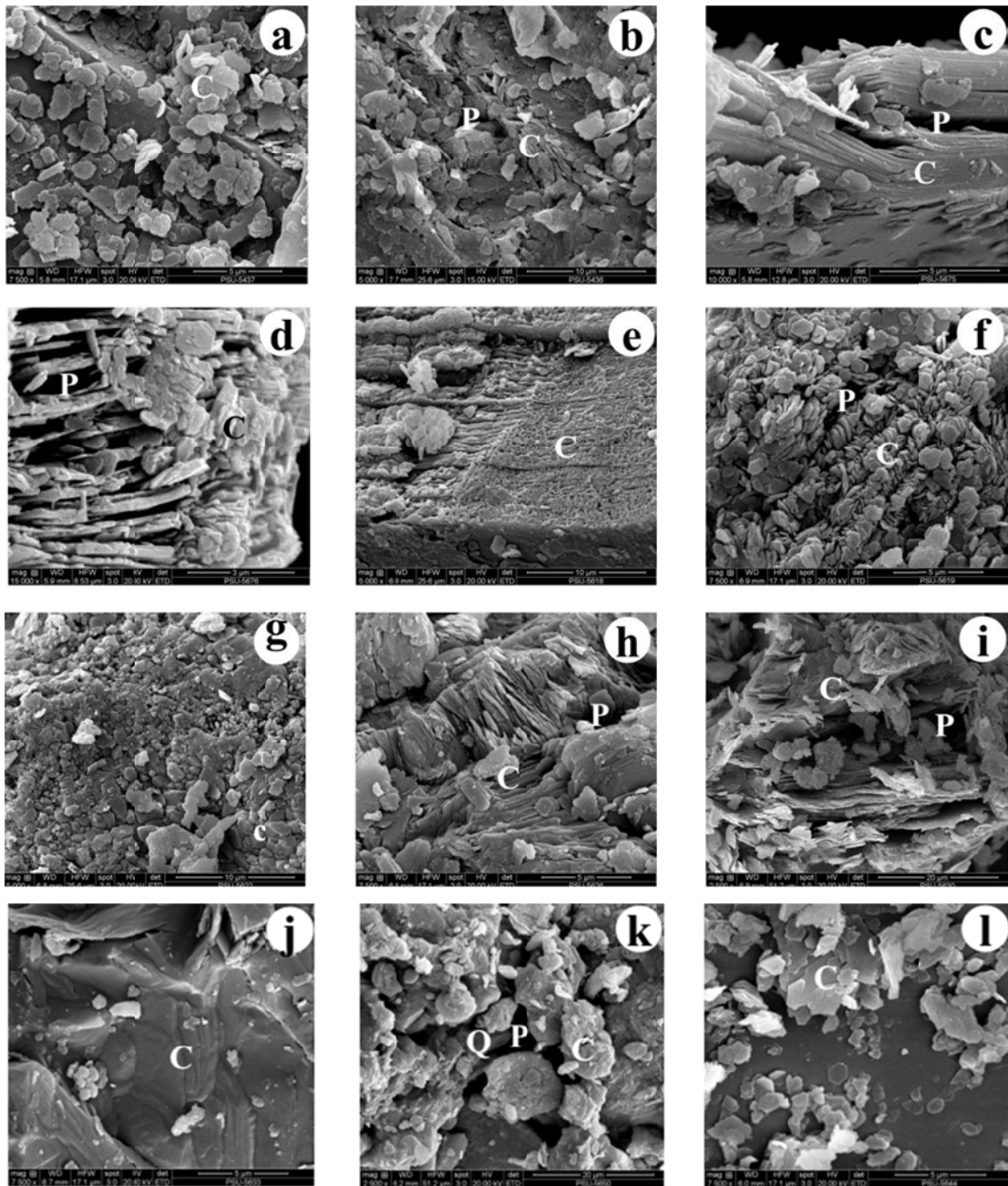
Figure 3.17 Micro structure of samples from granite site, (a) – (d) sample KB_1_2, (e)-(f) sample KB_4_2, (g)-(i) sample KB_5_2, (j) sample KB_6_2, (k) sample KB_7_2, (l) sample KB_9_2. C-clay, Q-quartz, and P-pore.

In several samples from the granite site the clay minerals are clearly visible, often a number of these platy minerals stack as a pack of cards (see Figure 3.17c, d, e, and f). In some cases the staking is not perfect thus creating pores between the clay minerals (see Figure 3.17c, d). Non-compacted quartz grains as shown in Figure 3.17k also create small pores between the grains.
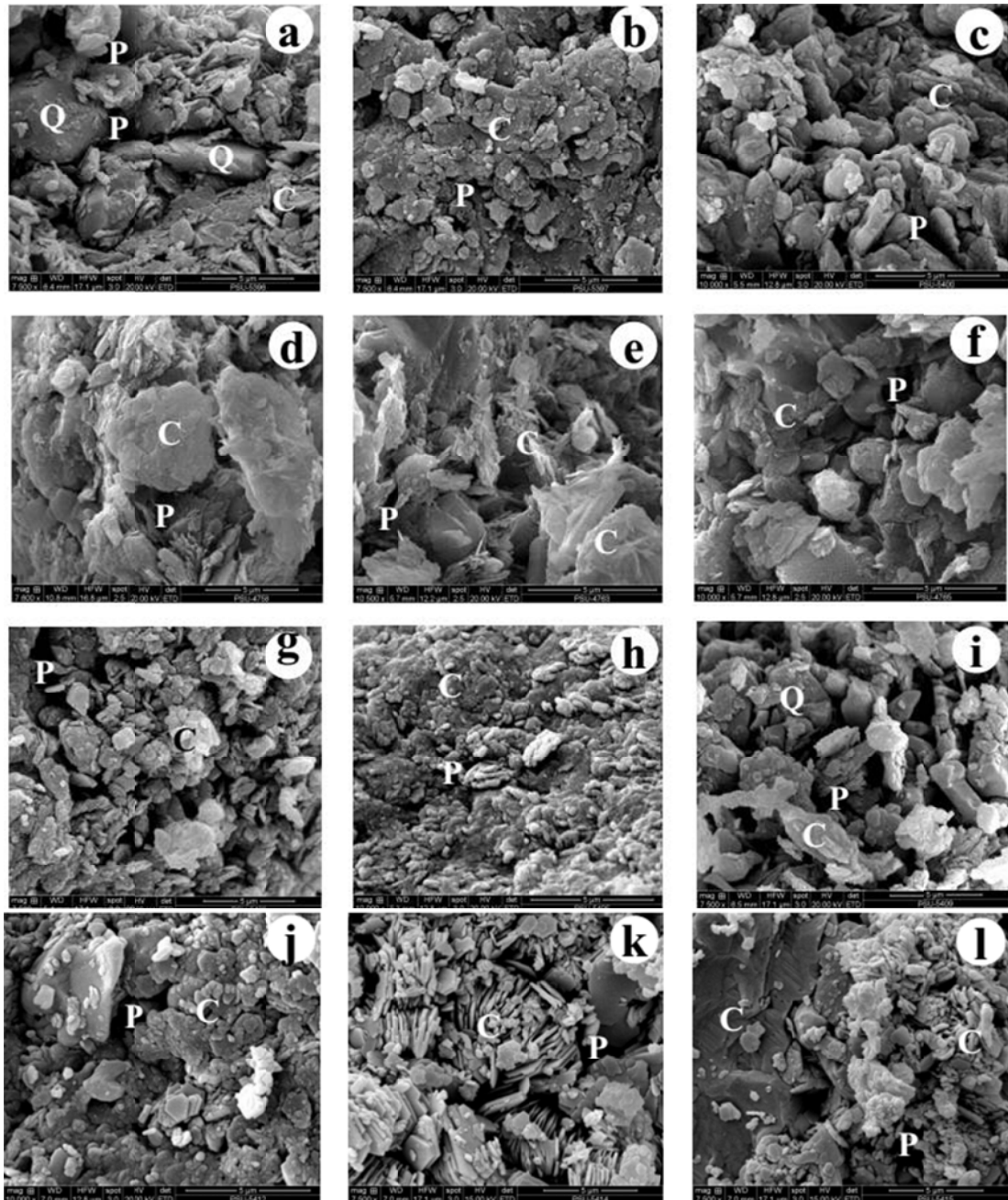
Figure 3.18 Microstructures of samples from the sandstone site, (a) – (c) sample KH_1_2, (d)-(f) sample KH_2_2, (g)-(i) sample KH_3_2, (j) – (l) sample KH_4_2. C-clay, Q-quartz, and P-pore.
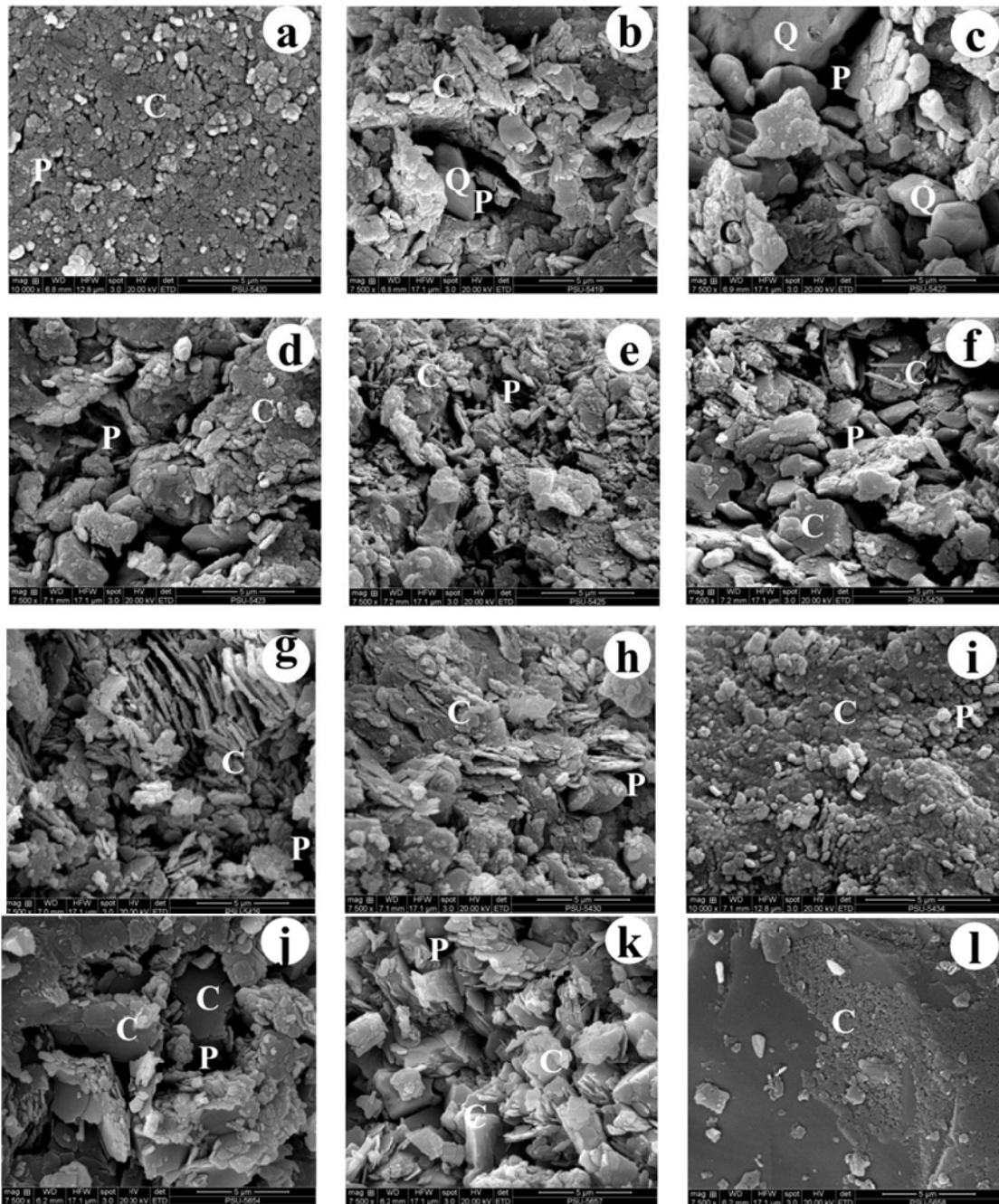
Figure 3.19 Microstructures of samples from the sandstone site, (a) – (c) sample KH_5_2, (d)-(f) sample KH_6_2, (g)-(i) sample KH_7_2, (j) – (l) sample KH_8_2. C-clay, Q-quartz, and P-pore.

The samples from the sandstone site show less staked clays as they are originated from a sedimentary rock (Figure 3.18-3.19), except in Figure 3.18k, but here the stacked clay minerals are overall chaotically arranged. Figure 3.18a and 3.19c show that the clay minerals surrounding the quartz minerals. It seems that the

quartz minerals a somehow "coated" with clay minerals and therefore they are often not visible. Pores are created through the non-compact arrangement of clay and quartz minerals, for example 3.19b shows how a clay mineral stays in a pore and by this prevents it from easy closure.
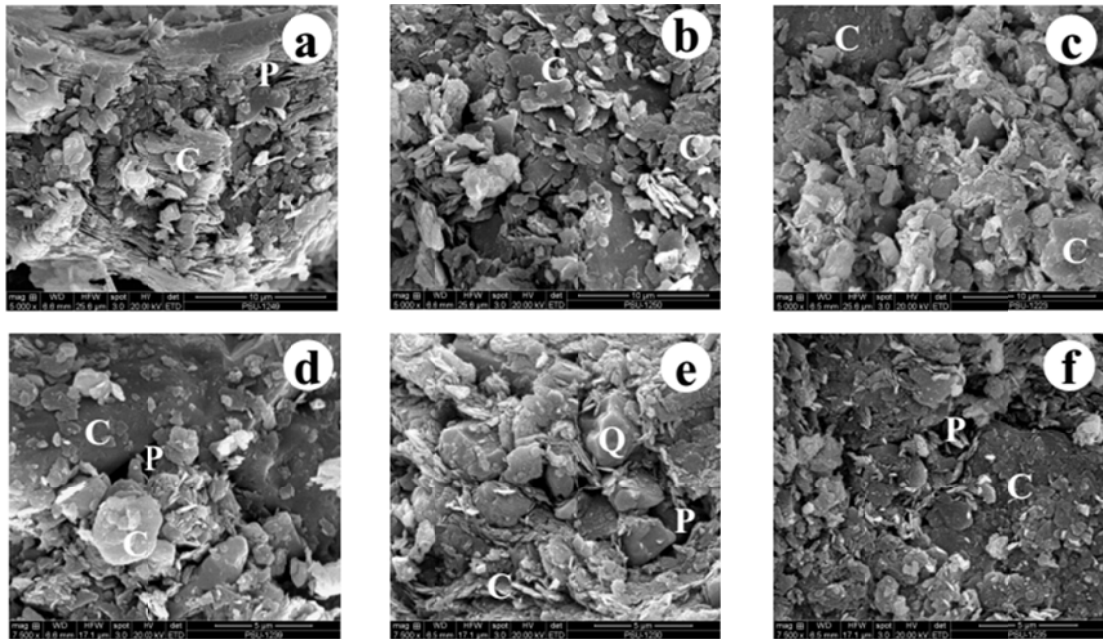
Figure 3.20 Microstructures of samples after fully saturated with water, (a)-(b) sample KB_4_2, (c) sample KH_1_2, (d) sample KH_5_2, (e) sample KH_6_2, and (f) sample KH_7_2. C-clay, Q-quartz, and P-pore.

Figure 3.20 shows selected samples from both sites after full water saturation and compaction. Less large pores are visible than in the images of Figure 3.17 to 3.19. Additionally, the clay minerals are now surrounding the quartz minerals and forming layer in-between (Figure 3.20e) and thus leaving less open space (pores) available.

For selected samples an element analysis was done with the SEM EDX system shown in Figure 3.21. Gold (Au) peaks are from the coating of the samples. The main element for all samples is Si (silicium), as all minerals are silicates. Clay minerals can be separated from the quartz minerals through their Al-peaks and for some samples also additional Fe- and K-peaks, iron and potassium, respectively.
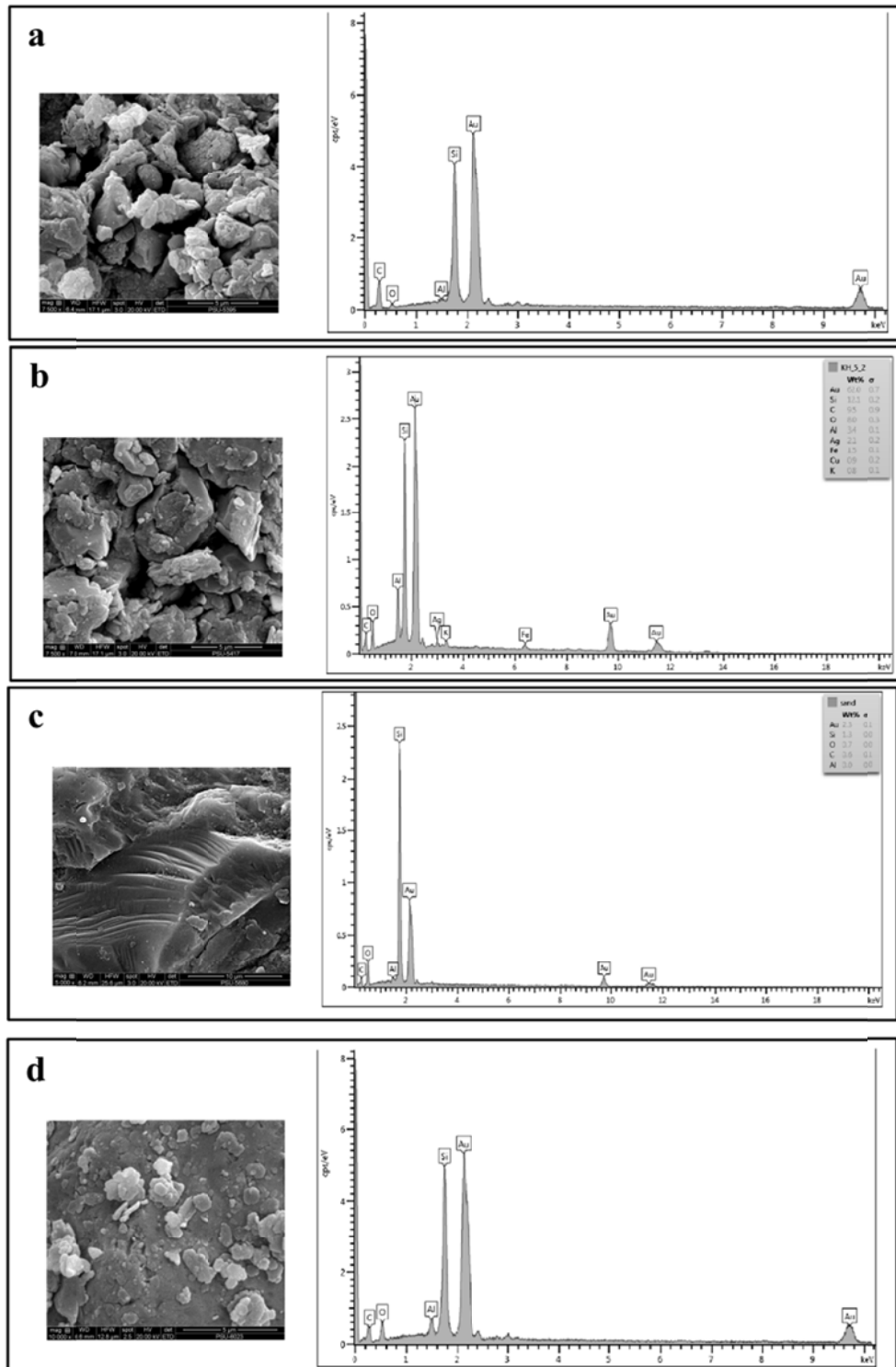
Figure 3.21 Composition of selected areas of the samples by EDX, (a) KH_1_2, (b) KH_5_2, (c) beach sand, (d) KB_1_2, e) KB_6_2, and (f) KB_7_2. Au is from the coating.
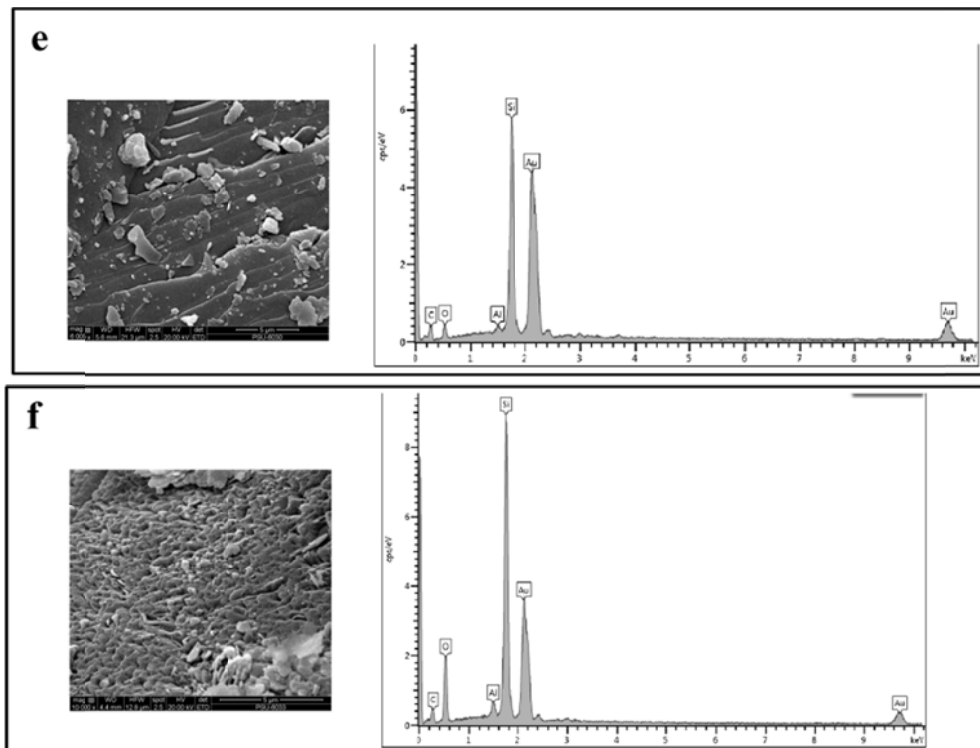
Figure 3.21 (cont.) Composition of selected areas of the samples by EDX, (a) KH_1_2, (b) KH_5_2, (c) beach sand, (d) KB_1_2, e) KB_6_2, and (f) KB_7_2. Au is from the coating.

3.7 Hydraulic conductivity

The hydraulic conductivity of selected samples is shown in Figure 3.22 for samples from the granite site and in Figure 3.23 for samples from the sandstone site. In general the values are comparable to published values (see for e.g. Schön, 2011). The values of the hydraulic conductivity for samples from the granite site vary from about 10^{-4} to 10^{-2} m/s, whereas the variation for the samples from the sandstone site is much smaller, from about 10^{-3} to 10^{-2} m/s.

The differences in the hydraulic conductivity can be mainly attributed to the grain size distribution of the samples (see Section 3.4). For the granite site samples sample KB_8_2 has the highest hydraulic conductivity and the sample is classified as sand, as the fine part is almost absent (see Figure 3.11 and 3.15). With increasing fine (clay) content the hydraulic conductivity decreases with sample KB_2_2 and KB_4_2 showing the lowest values (compare Figure 3.15).

The differences in the hydraulic conductivity for the samples from the sandstone site do not correlate well with the grain size distribution. Also there is no clear evidence that the hydraulic conductivity increases from the bottom to the top layer or vice versa. The absolute differences between the samples are relatively small.
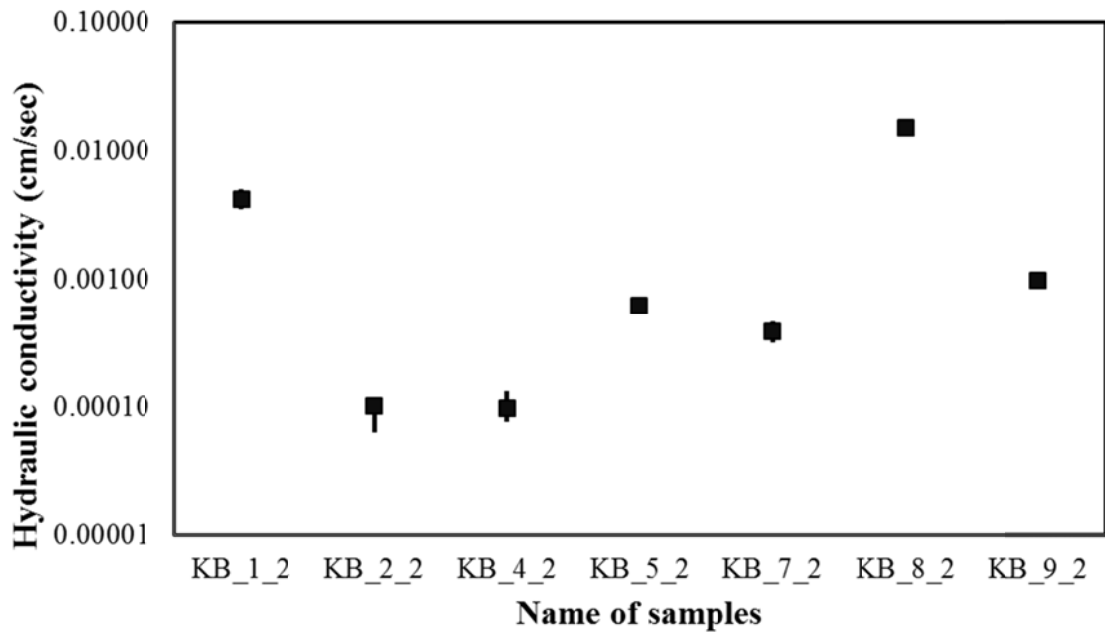
Figure 3.22 Hydraulic conductivity of the samples from the granite location.
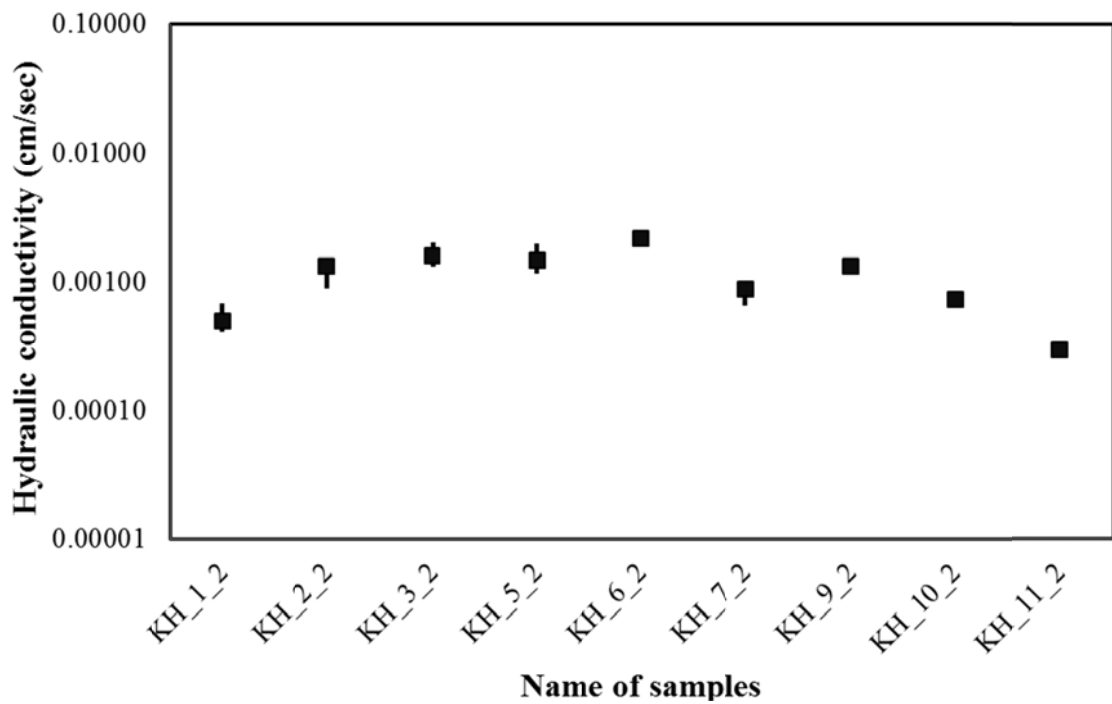
Figure 3.23 Hydraulic conductivity of the samples from the sandstone location.

3.8 Electrical resistivity

The electrical resistivity with increasing water saturation for the samples from the sandstone site are shown in Figure 3.24, with the three profiles from bottom to top, altogether nine samples. In Figure 3.25 the values for seven samples from the granite site and one beach sand sample are presented. In general the resistivity decreasing with increasing water saturation following Archie's law and the modified Archie's law (see Section 2.9.2). For all samples the laboratory values and the modeled data show a good agreement when the constants a, m, and n changed accordingly.

For almost all samples the electrical resistivity at room dry conditions is about 100,000 ohm m and decreases with increasing water saturation down to about 100 ohm m, thus reflecting that the composition and porosity for most of the samples is close. However, for sample KB_5_2 and KB_8_2 the electrical resistivity at 100% water saturation is few hundred ohm m due to mainly larger grain sizes than the other samples, which means also less clay.

For the samples from the sandstone site it is obvious that for two profiles the samples at the bottom have a higher resistivity than the layers above and that the top layer has the lowest resistivity; in all cases independent from water saturation (Figure 3.24a-b). The profile in Figure 3.24c however does not fit into this scheme.
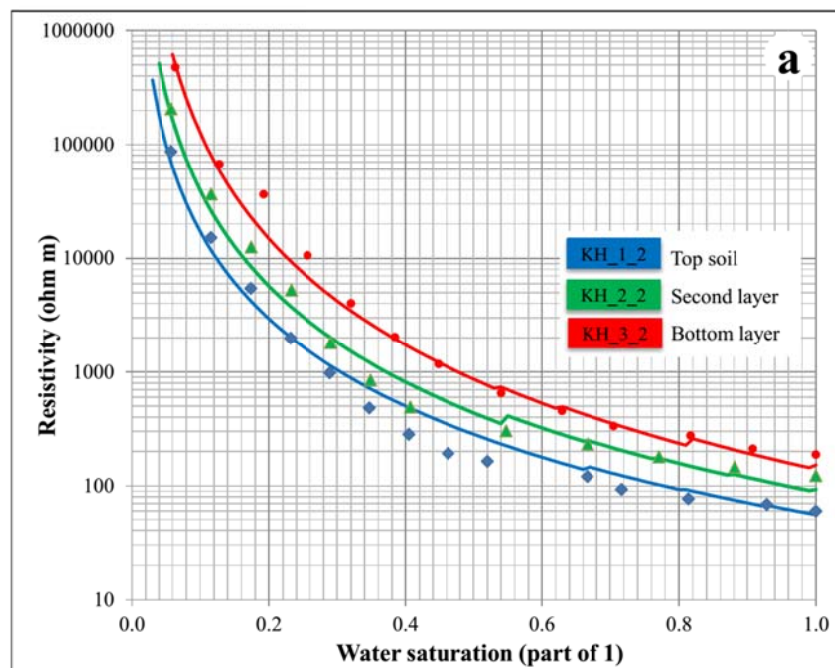
Figure 3.24 Resistivity of samples from the sandstone location (a) left profile, (b) central profile, and (c) right profile.
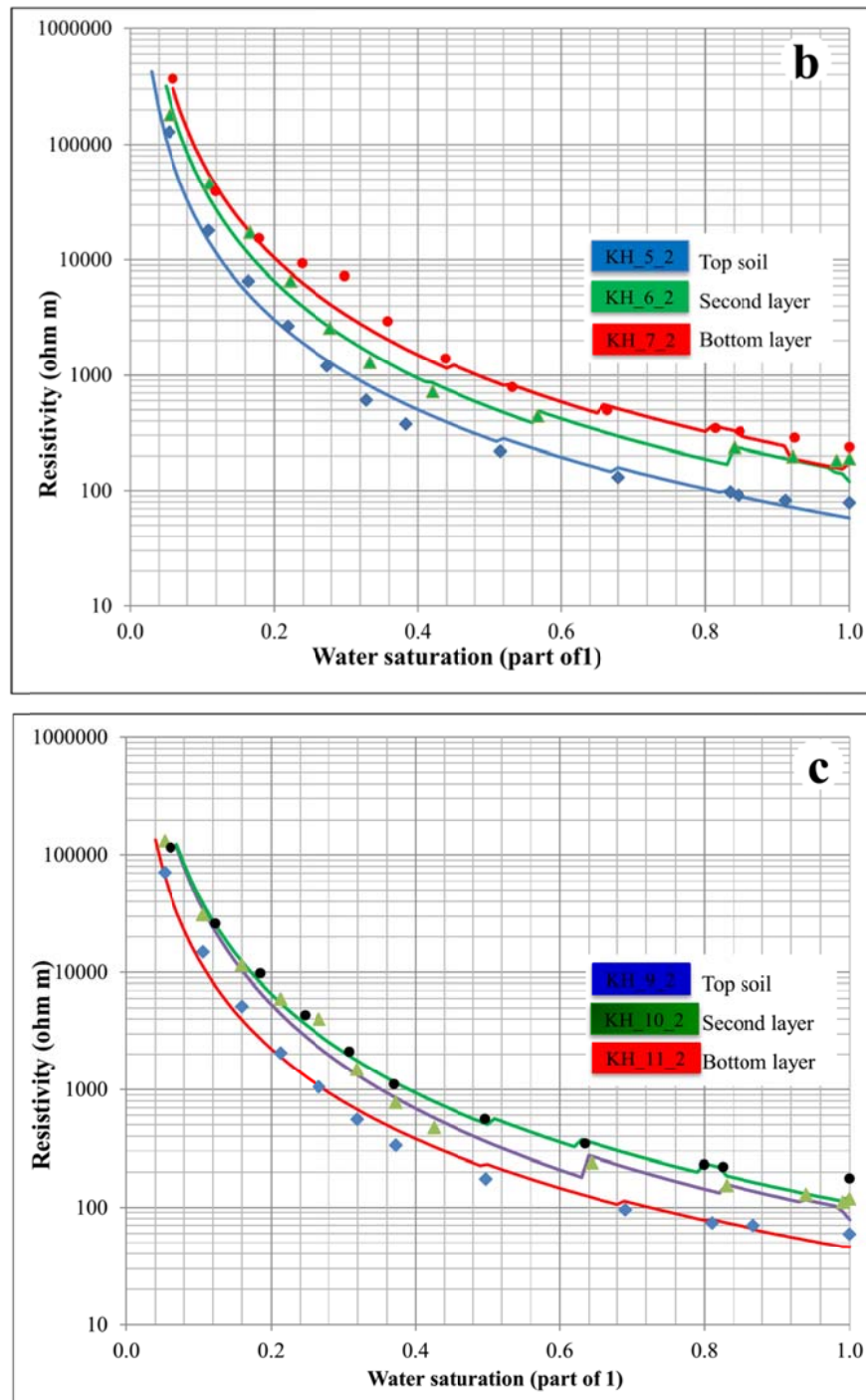
Figure 3.24 (cont.) Resistivity of samples from the sandstone location (a) left profile, (b) central profile, and (c) right profile.
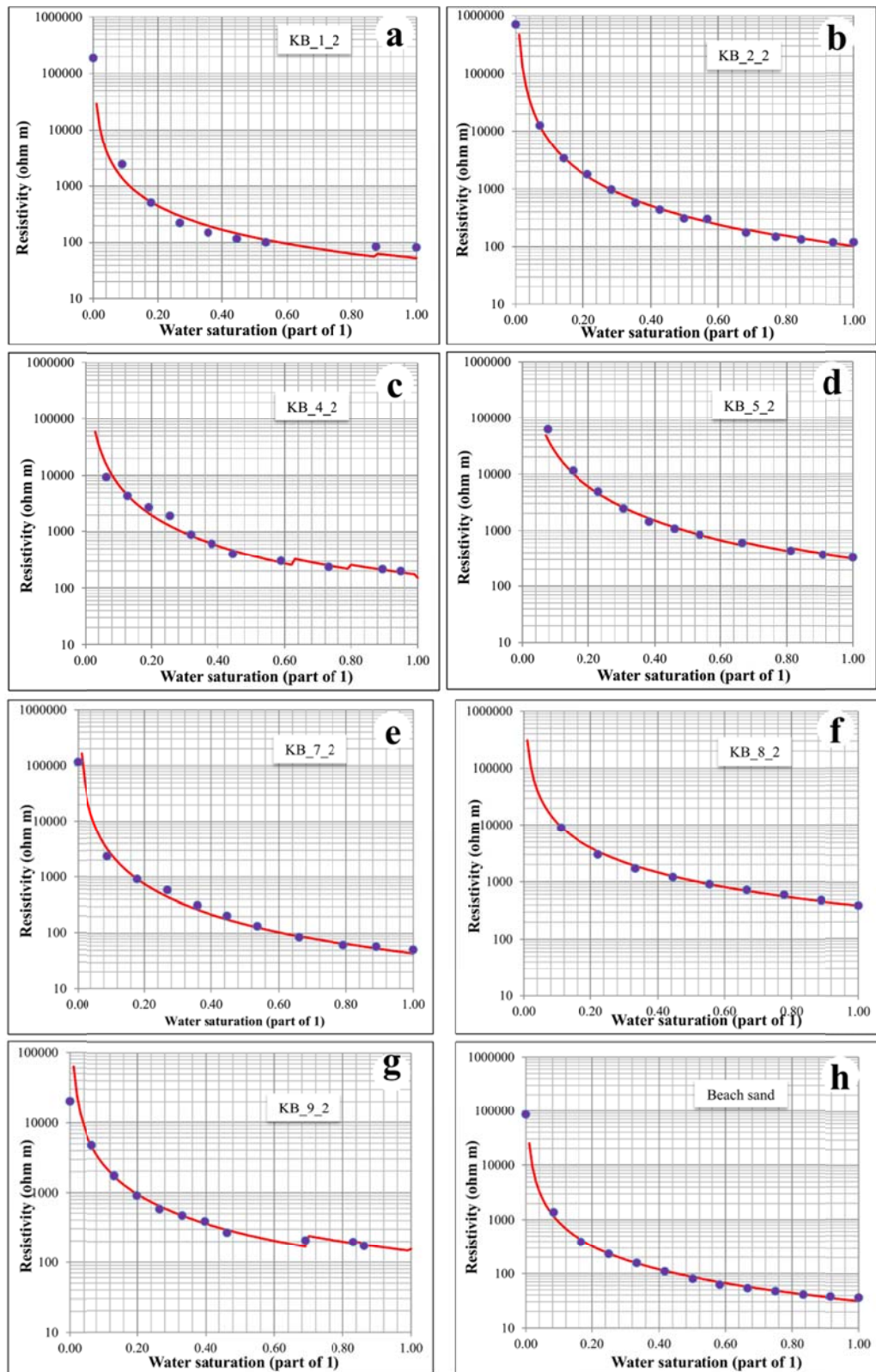
Figure 3.25 Resistivity of granite location, (a) sample KB_1_2, (b) sample KB_2_2, (c) sample KB_4_2, (d) sample KB_5_2, (e) sample KB_7_2, (f) sample KB_8_2, (g) sample KB_9_2, and (h) beach sand.

3.9 Seismic velocities

The seismic velocities, P- and S-wave velocities, for the samples with increasing water saturation are shown in Figure 3.26 for beach sand, which was used as some kind of reference, in Figure 3.27 for samples from the granite site and in Figure 3.28 for samples from the sandstone site. For all samples and in compliance with Hook's law the P-wave velocities are in general higher than the S-wave velocities.
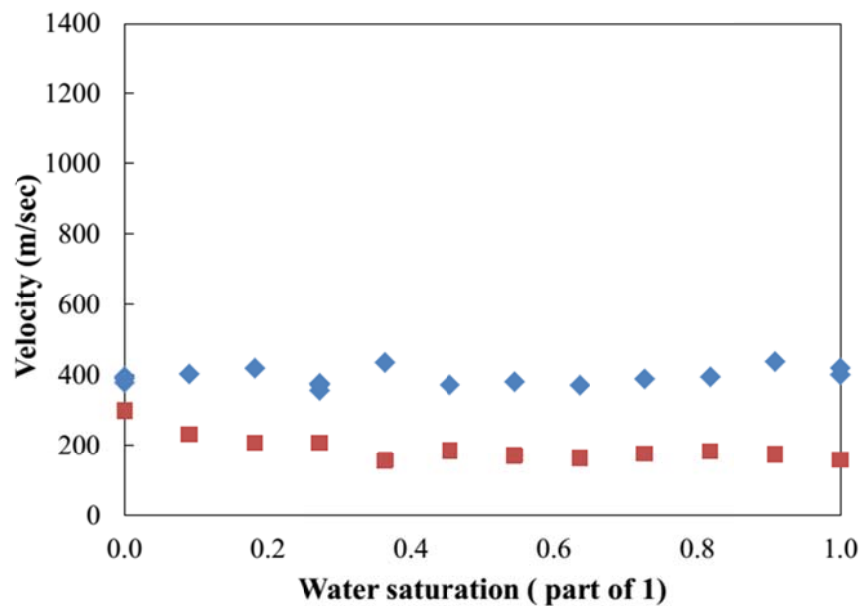
Figure 3.26 Velocity of beach sand. Vp: diamond (blue), Vs: square (red).

The beach sand composes mainly of sand (98%) with less clay (2%) and with a grain size of almost all grains between 0.1 and 1 mm, equal to sand, and has a porosity of 40%. The P-wave velocity is around 400 m/s, Vs is around 200 m/s, which is accordance with published values (Figure 3.26; see Schön, 2011). Further, the S-wave velocities decrease slightly with increasing saturation, because Vs is determined by the stiffness (shear modulus) of the granular skeleton and the bulk density, which depends on the grain density and the degree of saturation (see Equation 2.24).
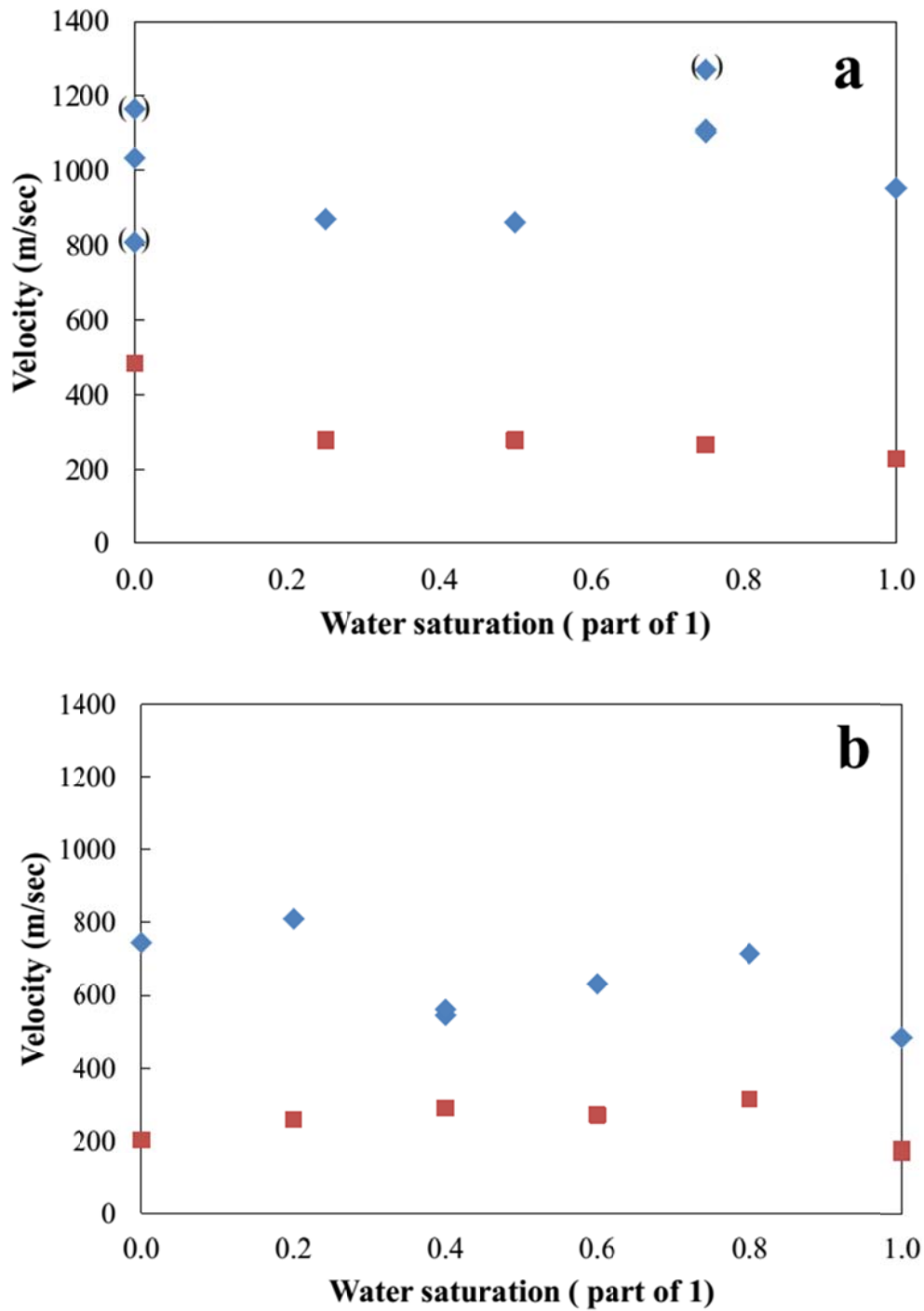
Figure 3.27 Velocity of main granite location, (a) sample KB_1_2, (b) sample KB_4_2, (c) sample KB_7_2, and (d) sample KB_9_2. Vp: diamond (blue), Vs: square (red).
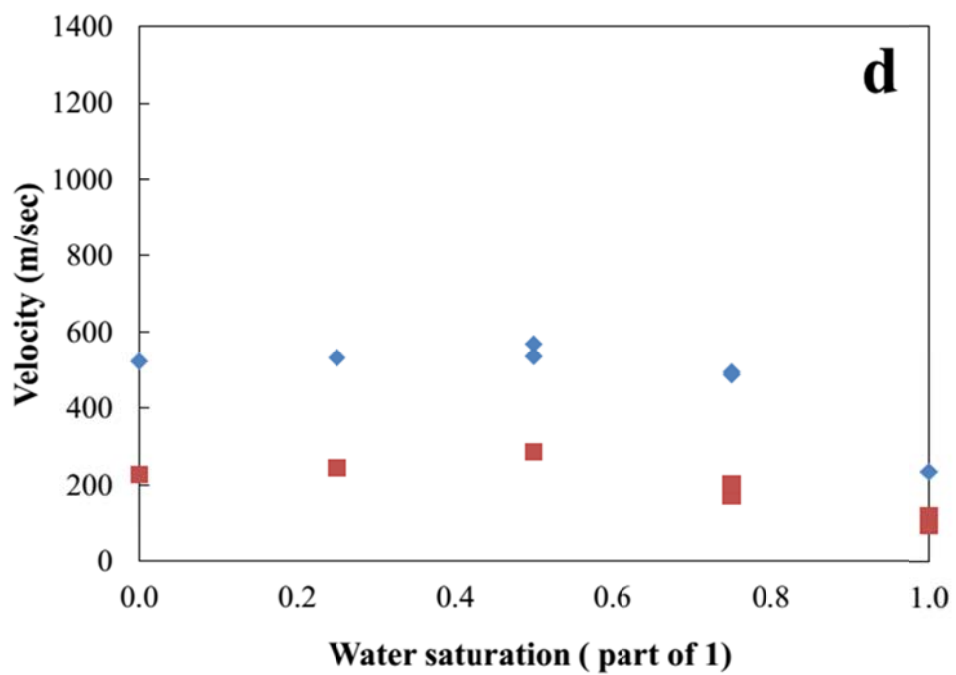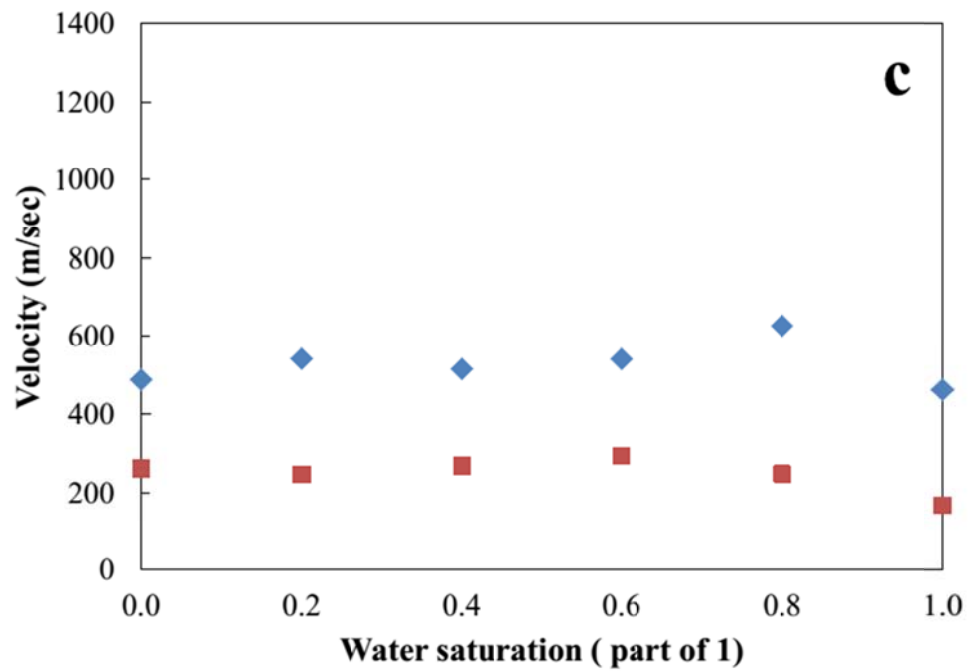
Figure 3.27 (cont.) Velocity of main granite location, (a) sample KB_1_2, (b) sample KB_4_2, (c) sample KB_7_2, and (d) sample KB_9_2. Vp: diamond (blue), Vs: square (red).

The seismic velocities with increasing water saturation for four samples from the granite site are shown in Figure 3.27a-d. The P-wave velocities at dry conditions are in the range of 500-800 m/s whereas the S-ware velocities for the same condition range between 300 and 500 m/s; published data provide similar values (e.g. Schön, 2011). Some data points seem not to reflect the overall trend of the velocities with increasing saturation highlighting the difficulties in the measurements of such samples.

For three samples, KB_1_2, KB_4_2, and KB_7_2, it seems that Vp keeps almost constant before 80% water saturation, then increase at 80%, and then towards 100% water saturation decrease significantly, for sample KB_7_2 for example below the initial value. For sample KB_9_2, the increase is already at around 50% water saturation and after that the decrease is significant. The shear wave velocities mainly decrease with decreasing water saturation, however the gradient of decrease at almost 100% water saturation is for most samples significant larger (see Figure 3.2b-d). For the general decrease the explanation given for the beach sand also hold here.

The seismic velocities with increasing water saturation for four samples from the sandstone site are shown in Figure 3.28a-d. The P-wave velocities at dry conditions are in the range of 700-900 m/s and by this slightly higher. The S-ware velocities for the same condition range between 220 and 500 m/s; also in accordance to published data (e.g. Schön, 2011).

Both Vp and Vs decrease with increasing water saturation. For the shear wave velocities the explanation provided for the beach sand also applies here. However, the gradient of decrease is larger towards a saturation of 100%. For the P-wave velocities the values also decrease significantly towards 100% water saturation, but some samples exhibit an increase before at around 40-50% water saturation (Figure 3.28b-d).

The behavior of the P-wave velocity might be explained by the macroscopic visible change of the sediment with increasing water saturation shown in Table 3.4 and 3.5. With increasing water saturation first some grains stick together, and at about 80% all grains stick together correlating with increased Vp values. After that the sediments exhibit liquid behavior which correlates with a sharp drop in the P-wave and S-wave velocities.
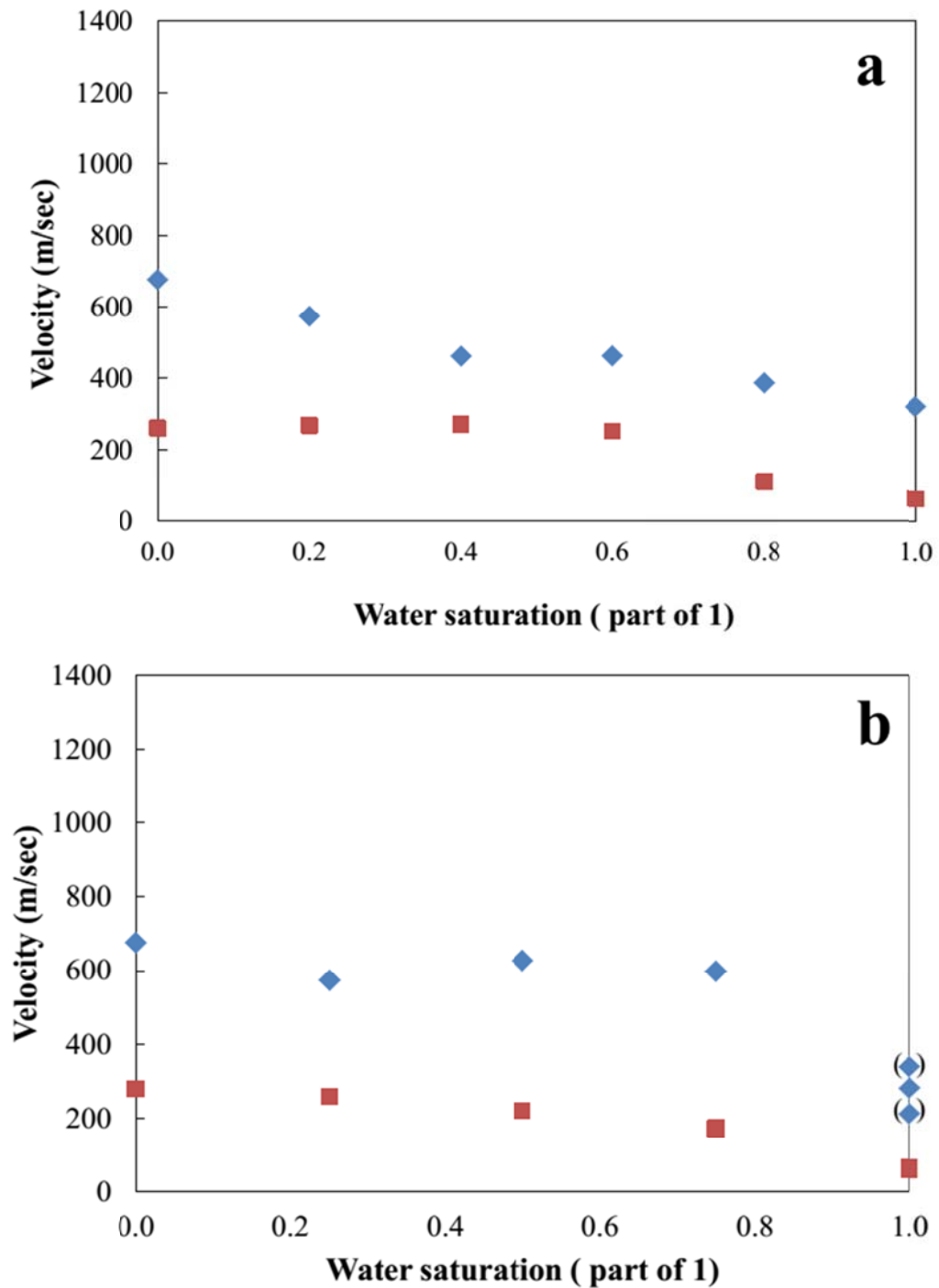
Figure 3.28 Velocity of samples from the sandstone location, (a) sample KH_1_2, (b) sample KH_2_2, (c) sample KH_3_2, and (d) sample KH_7_2. Vp: diamond (blue), Vs: square (red).
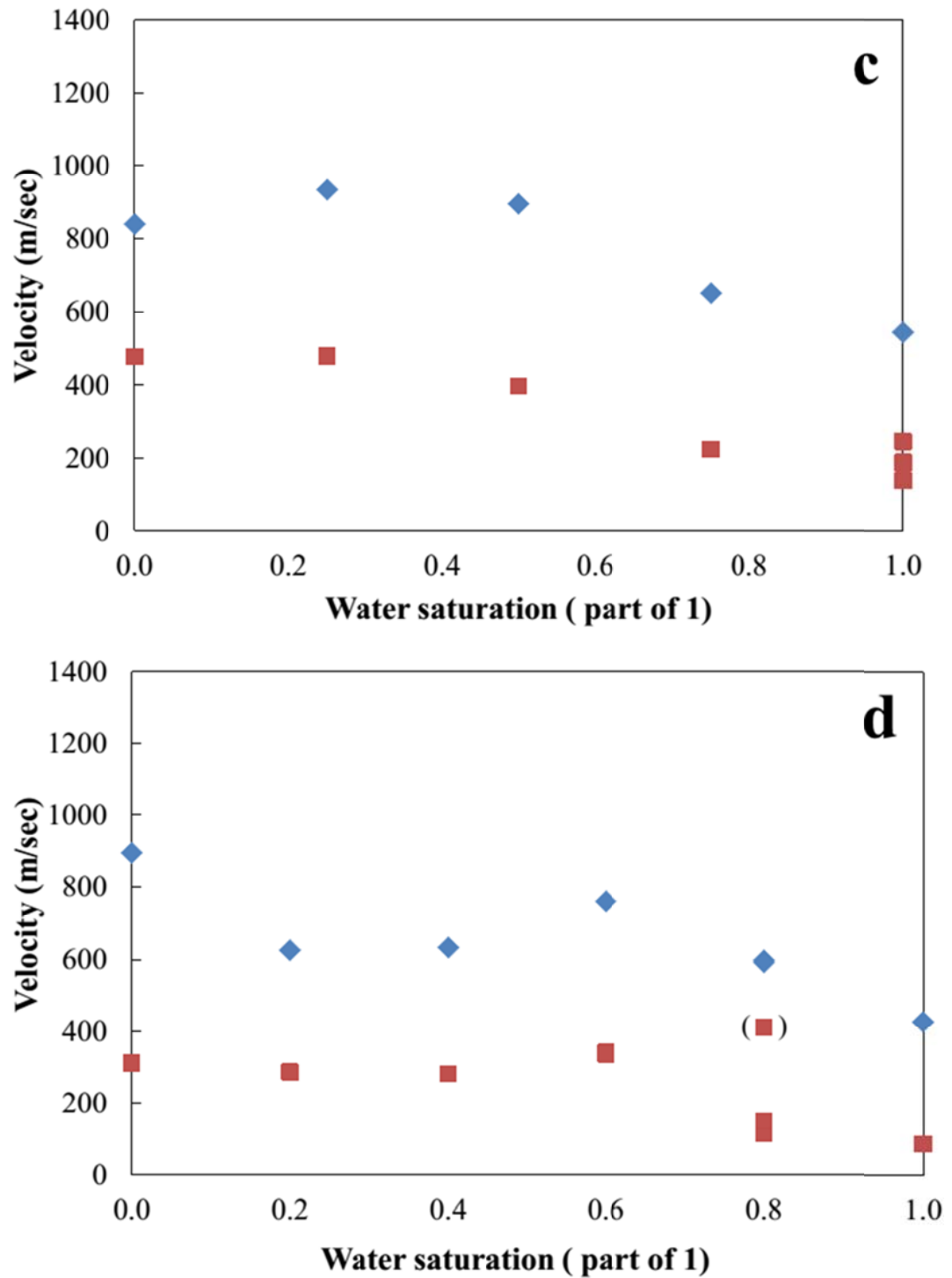
Figure 3.28 (cont.) Velocity of samples from the sandstone location, (a) sample KH_1_2, (b) sample KH_2_2, (c) sample KH_3_2, and (d) sample KH_7_2. Vp: diamond (blue), Vs: square (red).

Table 3.4 Images, macroscopic description and seismic velocities with increasing water saturation for sample KH_2_2.

	Water (%)	Description	V_P (m/s)	V_S (m/s)
	0.00	Crumble	767	279
	0.14	Some grain connect, some grain crumble		
	0.29	Some grain connect, small grain connect	573	258
	0.43	More grain connect, big grains now		
	0.57	Grain connect, start sticking together	627	220
	0.71	Grain connect, big grain, start to get hard, sticky		
	0.86	Plastic, all grains stick together, very hard, tight	598	171
	1.00	Liquid behavior, soft, water coming out	277	62

Table 3.5 Images, macroscopic description and seismic velocities with increasing water saturation for sample KB_7_2.

	Water (%)	Description	V_P (m/s)	V_S (m/s)
	0.00	Crumbly, no agglomeration	488	261
	0.14	Some grain connect, some grain crumble		
	0.29	Some grain connect, small aggregates formed	542	246
	0.43	More grain connect, bigger aggregates formed	516	268
	0.57	Grain connect, begin to stick together	542	294
	0.71	Grain connect, sticky, beginning to get hard		
	0.86	Plastic, grain are together, hard, tight	627	247
	1.00	Liquid behavior, water coming out, soft	462	164

3.10 Elastic parameter

From the seismic velocities, Vp and Vs, and the bulk density values for different saturation levels the four elastic parameters were calculates, bulk modulus, and shear modulus (or stiffness), as well as the Young's modulus and the Poisson's ratio.

The elastic parameters of the beach sand sample are shown in Figure 3.29. The bulk modulus increases with increasing saturation which is related to the decrease in the air content. Air content has a strong effect in decreasing the bulk modulus (see Santamarina et al., 2001). The shear modulus on the other hand decreases with increasing water content, which is significant at around 30% saturation. This is related to the density increase by the water saturation (e.g. Salgado et al., 2000). The Young's' modulus shows a similar behavior than the shear modulus, the curve is decreasing from 0.2 to around 1.2 at 305 saturation and until 100% it remains flat. Whereas the Possion's ratio increase until 30% saturation and from there remains almost flat at about 0.4.
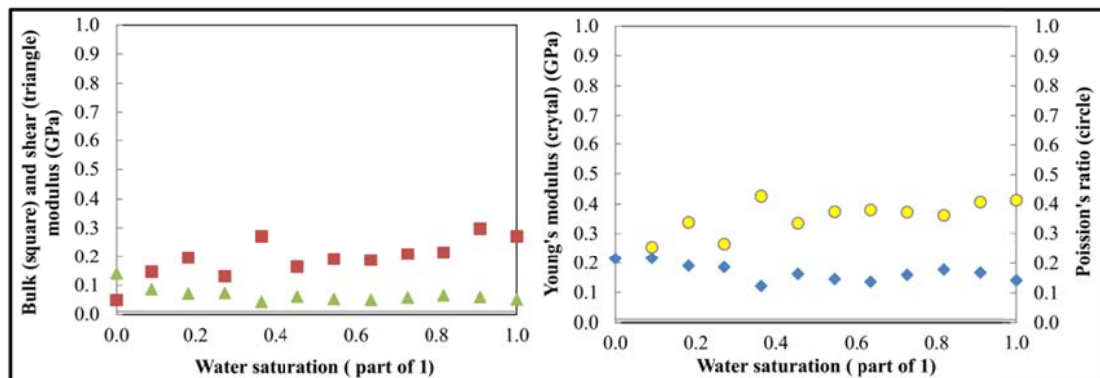
Figure 3.29 Elastic parameter of beach sand, red square: bulk modulus, green triangle: shear modulus, blue crystal: Young's modulus, yellow circle: Poisson's ratio.

The elastic parameters of the four samples from the granite site are shown in Figure 3.30a-d. The bulk modulus at low water saturation levels shows not a clear distribution for all samples. At about 50-70% it increases at with higher saturation approaching 100% it drops significantly. The shear modulus decreases with increasing water saturation with very low values at almost 100% water saturation. The explanation for the beach sand can also applied here. The Young's modulus decreases more or less with increasing water saturation and end with very low values at 90-100% (see Figure 3.30).
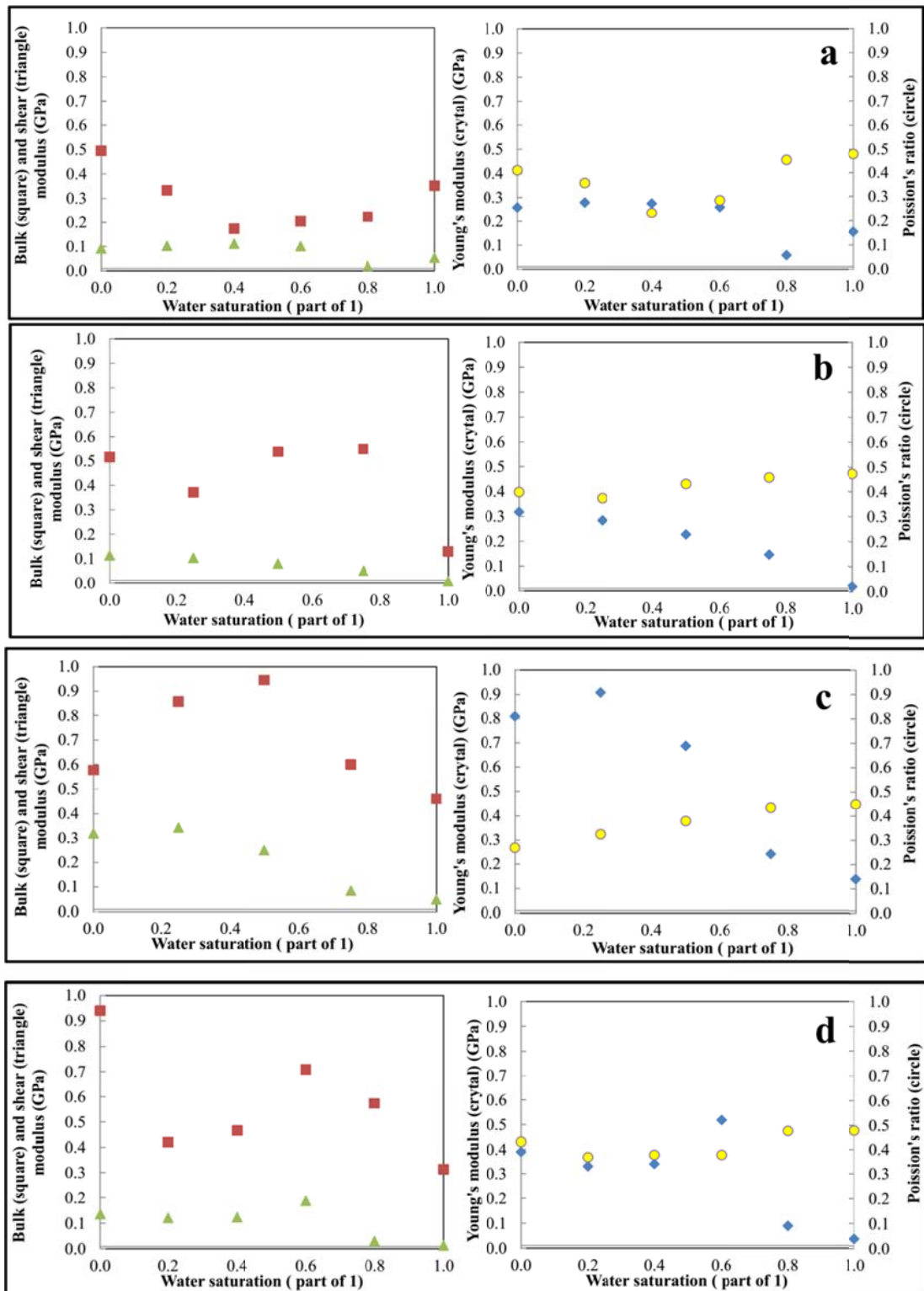
Figure 3.30 Elastic parameter of the samples from the granite location. Red square: bulk modulus, green triangle: shear modulus, blue crystal: Young's modulus, yellow circle: Poisson's ratio. Sample (a) KB_1_2, (b) KB_4_2, (c) KB_7_2, and (d) KB_9_2.
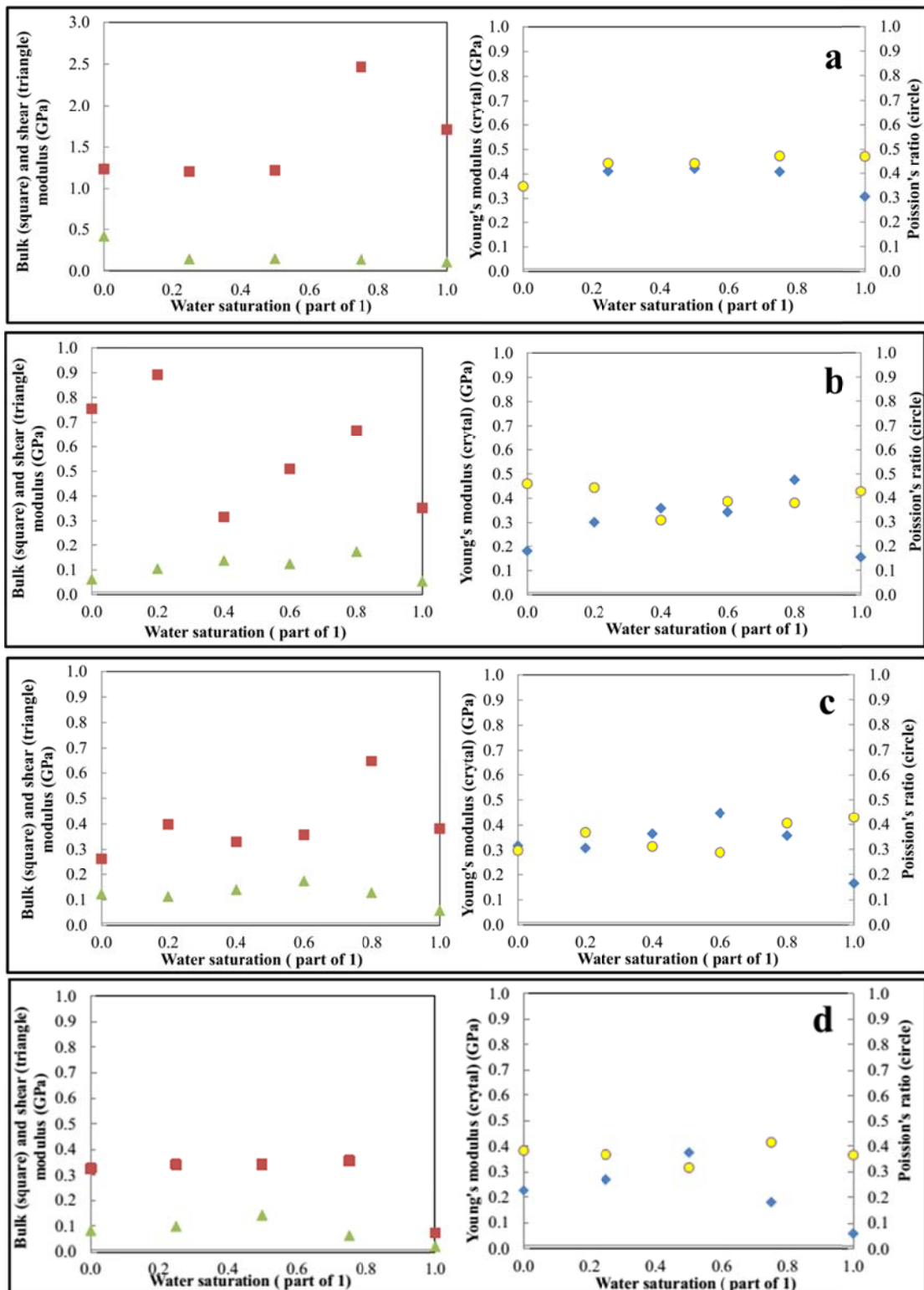
Figure 3.31 Elastic parameter of samples from the sandstone location. red square: bulk modulus, green triangle: shear modulus, blue crystal: Young's modulus, yellow circle: Poisson's ratio, Sample (a) KH_1_2, (b) Kh_2_2, (c) KH_3_2, (d) KH_7_2.

The Poisson's ratio for all samples shown in Figure 3.30 increase from around 2.7-4.0 at low saturation values to almost 0.5 indicating a perfectly incompressible material that deforms elastically at small strains (Poisson's ration = 0.5) (see Santamarina et al., 2001).

The elastic parameters of the four samples from the sandstone site are shown in Figure 3.31a-d. The bulk modulus for all samples does not show a clear trend; it might be concluded that in general there is no change taken into account uncertainties in the data points. The shear modulus decreased for all samples with increasing water saturation, but a significant decrease can be seen at around 60-80%. Comparable like for the samples form the granite site the Young's modulus decreases more or less with increasing water saturation and end with very low values at 90-100% (see Figure 3.31). The Poisson's ratio for the samples increases from around 3.0-4.5 at low saturation values to almost 0.5 indicating also here an almost perfectly incompressible material (see above), as shown macroscopically in Table 3.5.

4. Discussion and Conclusion

4.1 Relationships with electrical resistivity

As shown in Chapter 3 in general the electrical resistivity decreases when the water content increases which is in accordance with the theory of the modified Archie's equation. It can be seen that for a water content of 0-40% there is a larger gradient for the decrease of the electrical resistivity. The shape of the resistivity curve can be attributed to a combination of electrolytic conductivity of the pore fluid and colloidal conductivity processes related to the clay content. In sediments with clay content, the electrical charges located at the surface of the clay texture lead to less electrical resistivity than in coarse-textured soils because of the magnitude of the specific surface (Samouëlian et al., 2005). A large specific surface area supports the surface conductivity because a number of cations in clay minerals are higher valence; electrical charge of the clay mineral surface is negative. It is compensated by the concentration of cations in the pore water in the mineral surface. This process is the cation exchange capacity (CEC). The calculation of the resistivity of clayey material is not trivial, since the electrical current flow is possible through clay minerals as well as through pore fluid (Kirsch, 2006).

Result from the resistivity measurements versus increasing water saturation are shown in Figure 3.24 for the three samples, KH_1_2, KH_2_2, and KH_3_2 in semi-log graph. The shape of the curve for all three samples is similar, but the absolute values are different, with the resistivity values showing following order: KH_3_2 > KH_2_2 > KH_1_2. However, for the three samples here the clay content is relatively similar, which might not explain the differences in the absolute resistivity values.

However, the three samples in Figure 3.24 show significant difference in the gravel and sand grain size distribution. Sample KH_3_2 has a gravel content of 36% and a sand content of 15%, sample KH_2_2 has 24% and 36%, and sample KH_1_2 has 6% and 47%, respectively. A higher resistivity correlates with a higher content in gravel and vice versa. The larger gravel grains might obstruct the electrical pathway more than the sand grains and might also have an effect on the clay distribution in the sample (see Figure 4.1). This would explain that the differences are more or less independent from the saturation degree.
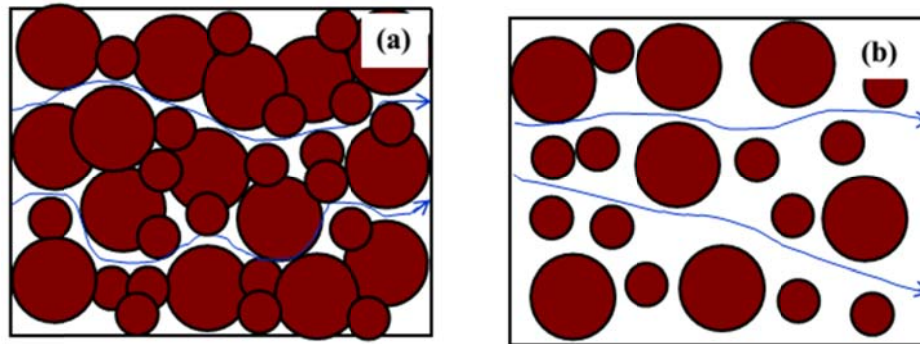
Figure 4.1 Relationship between the grain size and electrical current. a) Higher content of larger grain size, b) lower content of larger grains size, white areas represent smaller grain sizes.

In Figure 3.24 the lines represent the calculations of the electrical resistivity using average parameters from the laboratory measurements: clay content (percent of clay and silt), porosity, matrix density, and conductivity of the water used. In order to fit a curve with the experimental values from the electrical resistivity measurements, the values m, n, and a in Equation 2.20 were changed; it was tried not to change value a significantly. When m was increased, the curve changed to higher resistivity values at higher degrees of saturation and the curve changed to much higher resistivity values at lower degrees of saturation when n was increased. For the three samples shown in Figure 3.24 following order for the values m and n were obtained: KH_3_2 > KH_2_2 > KH_1_2. The tortuosity factor m increases with depth and with increasing larger grain size, making it more difficult for the electrical current to find a pathway, thus resulting in a higher resistivity. The increase in n value with depth might reflect the distribution of the pores associated with a larger portion of larger grains.

A summary of all m, n, and a values for nine samples from KH location and seven samples from KB location give following values: m=0.3-3.1, n=1.4-2.2, a = 0.8-1.0 for sediments from the granite site (KB), and m=1.0-3.9, n=2.5-3.2, a=1.0-1.1 for the sandstone site (KH) as shown in Figure 4.2. Values of m for KB and KH are overlapping, whereas values of n for KB are less than for KH, illustrating that these values change with sediment type, in general, and that one set of these values cannot be applied to all sediments types.
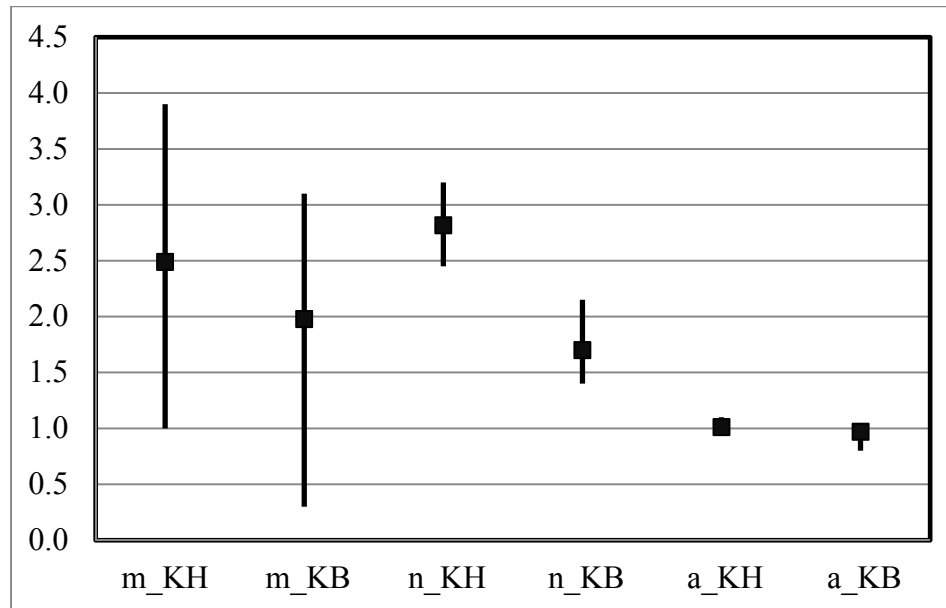
Figure 4.2. Comparison of m, tortuosity factor, n, saturation exponent, and *a*, a constant, of KH (9 samples) and KB (7 samples) location. Line reflects the range of all values; symbols represent the average value for each factor.

4.2 Relationships with elastic parameters

The measurement of seismic velocities of unconsolidated sediments with increasing water content is challenging, which is reflected by the P-wave velocity values. In general they do not change much with water saturation. Vp is primary controlled by the bulk modulus of the water, as well as by the porosity and the bulk modulus of the matrix grains (quartz, etc.).

The S-wave velocities in general are more consistent for both sample groups and the shear wave velocities have a direct effect on the small strain stiffness (see Equation 1.1). For clay bearing sediments the small strain stiffness depend on the composition of the soils, its structure, and shape and size distribution of the particles, as well as aging, altogether the nature of the soil (intrinsic variables); all these parameters have also an influence on cohesion and friction, the main properties related to the strength of the material (e.g. Salgado, 2000). Water is one of the most important instability factors for slopes as it decreases cohesion in soils and increases weight and pore water pressure in granular sediment (Santamarina et al., 2001).

The data from this study show that for the samples from the granite site as well as for the sandstone site the shear velocities significantly decrease at around 60-80% water saturation (Figure 3.27 and 3.28). This is reflected in a decrease in the

shear modulus at the same water saturation percentage (Figure 3.30 and 3.31). This also correlates with a decrease in the Young's modulus and an increase to almost 0.5 of the Poisson's ratio. All this indicated that at around 60-80% water saturation the mechanical properties of the sediment samples from both sites significantly changes, thus reducing the stiffness of the unconsolidated sediments. That this might not necessarily result in lower shear strength has been remarked by Salgado et al. (2000) that although the small scale stiffness dropped the shear strength parameter increased with increasing clay content. For the shear strength with increasing water content this might not behave in the same way and has to be determined in a geomechanical laboratory.

4.3 Relationships to slope stability

The results of the study have shown in Chapter 3, as well as in Section 4.1 and 4.2 that the unconsolidated sediments of the shallow subsurface exhibit differences in the nature of the sediments and in their properties. These differences have effect on the geomechanical properties as shown in Section 4.2 and Chapter 3. However, friction and cohesion are the main parameter of the shear strength that governs the slope stability. So, do these differences between different layers make the layer interfaces a preferred friction plane. Because the question is here where in a slope a friction plane can develop easily that is leading finally to the slope instability. Large scale laboratory testing would be required to answer this question

4.4 Relationships to a landslide early warning system

In a landslide early warning system one type of senor used is making use of the resistivity changes in the soil and sediments with increasing water saturation (see Section 1.5). From the results of the electrical resistivity measurements in this study it can be seen that above a water saturation of around 50-60% the values of the electrical resistivity are not changing significantly for field measurements. Further, it has to be noticed that the resistivity change of a sediment or soil mainly depends on the nature of this sediments; this can change with depth. Therefore, detailed investigation about the sediment at the depth of the sensor would be useful in order to increase its sensitivity.

4.5 Conclusions

The electrical resistivity of clay bearing unconsolidated sediments is a complex phenomenon. Laboratory measurements have shown that the electrical

resistivity decreases when the water content increases because of a combined effect from the electrolytic conductivity of the pore fluid and the colloidal conductivity from the clay mineral, and that the data follow current theory. However, the fitting parameter, m, n, and a, vary with different sediment type. With limited data the difference are clear. Further, the results of this study suggest that the grain size distribution has a significant effect on the absolute resistivity, independent from the water saturation.

This study has clearly demonstrated that soils and sediments are different in their nature depending on their source or base rock, here granite and sandstone. The nature of the sediments also changes or can change with different states of weathering and different distances of short transportation as shown here. The different nature of the sediments has an effect on the different properties. This has been demonstrated with the shear modulus and the other elastic parameters. These differences can have an effect on the cohesion and friction parameters of the shear strength, which at the end is controlling the slope stability. Therefore, further work has to be directed in more detailed geomechanical laboratory investigation of the shear strength parameter combined with detailed information about the nature of the sediments as done with this study. This will lead to a better understanding why and how slopes fail.

5. Utilization Possibilities

One of the main open issues in understanding slope failures leading to disastrous landslides is the role of pore water, especially its increase during and after heavy rain fall, because large amounts of rain are considered a main trigger for landslides. This study focused on the relationship between sediment characteristics, or the nature of the sediments, and electrical resistivity and seismic velocities as physical properties. Utilization of the results is possible in following ways, with

a) The geomechanical parameters derived from seismic velocities change significantly at about 60-80% water saturation indicating a possible change in the strength of the sediments. Future shear strength measurements with the parameters cohesion and friction might focus on this to see if there is a potential decrease of the shear strength. This then might be utilized for sensor calibration or development of news sensors for a landslide early warning system.

b) In a landslide early warning system another type of senor used is making use of the resistivity changes in the soil and sediments with increasing water saturation (see Section 1.5). From the results of the electrical resistivity measurements in this study it can be seen that above a water saturation of around 50-60% the values of the electrical resistivity are not changing significantly for field measurements. Further, it has to be noticed that the resistivity change of a sediment or soil mainly depends on the nature of this sediments, which can change with depth. From the results of this study it can be advised to carry out detailed investigation about the sediment at the depth of the sensor in order to increase its sensitivity.

c) The most shallow layers are of interest for farming and agricultural use. Precision agriculture is getting more and more attention where, for example, precise information about soil conditions are acquired and interpreted to choose the most suitable crops and to increase the yield. Electrical resistivity measurements are already applied, however the interpretation is often difficult. As the results of this study have shown the main parameters affecting soil resistivity, these parameters might be determined in order to enhance the interpretation of electrical field measurements.

6. References

American Society for Testing and Materials (ASTM). 1998. ASTM D 422- Standard Test Method for Particle-Size Analysis of Soils. In Annual Book of ASTM Standards. ASTM International, United States.

American Society for Testing and Materials (ASTM). 2001. ASTM C136 - Standard Test Method for Sieve Analysis of Fine and Coarse Aggregates. In Annual Book of ASTM Standards. ASTM International, United States.

American Society for Testing and Materials (ASTM). 2005. ASTM G187 - Standard Test Method for Measurement of Soil Resistivity Using the Two-Electrode Soil Box Method. In Annual Book of ASTM Standards. ASTM International, United States.

American Society for Testing and Materials (ASTM). 2010. ASTM D5084-03 Standard Test Methods for Measurement of Hydraulic Conductivity of Saturated Porous Materials Using a Flexible Wall Permeameter. ASTM International, United States.

American Society for Testing and Materials (ASTM). 2010. ASTM D854 - Standard Test Methods for Specific Gravity of Soil Solids by Water Pycnometer. In Annual Book of ASTM Standards. ASTM International, United States.

BBC, 2014. Japan landslides kill 32 in Hiroshima prefecture. Available at: http://www.bbc.com/news/world-asia-28862949 [accessed July, 5th 2014].

Beven, K. and German, P. 1982. Macropores and water flow in soils. Water Resources Research 18(5), 1311–1325.

Blott, S. J. and Pye, K. 2001. Gradistat: a grain size distribution and statistics package for the analysis unconsolidated sediment. Earth Surface Processes and Landforms 26: 1237–1248.

Brown, G. 2013. Darcy's Law Basics and More. http://biosystems.okstate.edu/darcy /laloi/basics.htm (Oct. 1, 2013).

Cho, G.C. and Santamarina, J.C. 2001. Unsaturated Particulate Materials—Particle-Level Studies. J. Geotech. Geoenviron. Eng. 127(1), 84–96.

Das, B.M. 2006. Principles of Geotechnical Engineering. Thomson Canada Limited, Canada.

de Blasio, F.V. 2011. Introduction to the physics of landslide: lecture notes on the dynamics of mass wasting (Chapter 2 Friction, Cohesion, and Slope Stability). Springer Science+Business Media, 23-52.

DiBiagio, E. and Kjekstad, O. 2007. Early Warning, Instrumentation and Monitoring Landslides. 2nd Regional Training Course, RECLAIM II, 29th January - 3rd February 2007

Fredlund, D.G and Rahardjo, H., 1993. Soil Mechanics for Unsaturated Soils. John Wiley & Sons, Inc., U.S.A.

Friedel, S., Thielen, A., Springman, S.M. 2006, Investigation of a slope endangered by rainfall–induced landslides using 3D resistivity tomography and geotechnical testing: Journal of Applied Geophysics 60, 100–114.

Gee, G.W. and Bauder, J.W. 1987. Particle – size Analysis. In Klute, A. (eds) Methods of Soil analysis Part 1- Physical and Mineralogical methods 2nd Edition, Soil Science Society of America and American Society of Agronomy, USA, 383-412.

Günzel, F. 1994. Geoelektrische Untersuchung von Grundwasserkontaminationen unter Berücksichtigung von Ton- und Wassergehalt auf die elektrische Leitfähigkeit des Untergrundes, PhD thesis Ludwig-Maximilians-Universität, München.

Harris, W. and White, G.N. (2008) X-ray Diffraction Techniques for Soil Mineral Identification. In Ulery, A. L. and Drees, L.R. (eds) Methods of Soil Analysis Part 5—Mineralogical Methods, Soil Science Society of America, Wisconsin, 81-116.

Hartge, K.H and Horn, R.1999. Einführung in die Bodenphysik. Enke, Stuttgart, Germany.

Herod, M. 2011. Groundwater Flow. http://globalgeology.blogspot.com/2011/06/-back-to-basics-on-groundwater.html (Oct. 1, 2013).

Immoor, L. 2006. Permeability, porosity and capillarity. http://jroberson.mssd14.wikispaces.net/file/view/Permeability,porosity,capilarity.pdf (Sep. 14, 2013).

Intrieri, E., Gigli, G., Mugnai, F., Fanti, R. and Casagli, N. 2012. Design and implementation of a landslide early warning system. Engineering Geology 147-148, 124-136.

Jarvis, N. 2007. A review of non–equilibrium water flow in solute transport in soil macropores; principles, controlling factors and consequences for water quality. European Journal of Soil Sciences 58(3), 523–546.

Kirsch, R. 2006. Groundwater Geophysics – a Tool for Hydrogeology. Springer-Verlag Berlin Heidelberg, Germany.

Lewis, D.W. and McConchie, D. 1994. Analytical sedimentology. Chapman & Hall, New York.

McNeill, J.D. 1980. Electrical conductivity of soil and rocks. Technical Note TN-5. Geonics Ltd.

MCOT news, 2011. Landlide kills teacher. 6 Jan 2011. http:\\www.mcot.news.net

Pagano, L., Picarelli, L., Rianna, G. and Urciuoli, G. 2010. A simple numerical procedure for timely prediction of precipitation-induced landslides in unsaturated pyroclastic soils. Landslides 7, 273–289.

Petley, D. 2012 Global patterns of loss of life from landslides. Geology. 40, 927-930.

Practical Sciences 2014. An overview of the zeta potential. Available online: http://particlesciences.com/docs/technical_briefs/TB_2012_2-Overview-of-Zeta-Potential.pdf [accessed 20 June 2014]

QAQC LAB. 2012. Equipment for quality control and R&D: sieve shaker. QAQC Lab. www.qclabequipment.com/efl230.jpg (Aug 11, 2014).

Qiu, J. 2014 Landslide risk rise up the agenda. Nature 511, 272–273.

Ramesh, M.V. 2014. Design, development, and deployment of a wireless sensor network for detection of landslides. Ad Hoc Networks 13, 2-18.

Revil, A. and Glover, P.W.J. 1998. Nature of surface electrical conductivity in natural sands, sandstones, and clays. Geophys. Res. Lett., 25(5), 691-694.

Reynolds, J.M. 1997. An introduction to applied and environmental geophysics. United Kingdom.

Salgado, R., Bandini, P. and Karim, A. 2000. Strength and stiffness of silty sand. Journal of Geotechnical and Geoenvironmental Engineering 126, 451-462.

Samouëlian, A., Cousin, I., Tabbagh, A., Bruand, A. and Richard, G. 2005. Electrical resistivity survey in soil science: a review, Soil & Tillage Research, Vol.83, pp.173–193.

Santamarina, J.C., Klein, K.A. and Fam, M.A. 2001. Soils and Waves, John Wiley & Sons, Chichester, UK.

Sassa, K., Nagai, O., Solidum, R., Yamazaki, Y. and Ohta, H. 2010. An integrated model simulating the initiation and motion of earthquake and rain induced rapid landslides and its application to the 2006 Leyte landslide. Landslides 7, 219–236.

Sawangsuriya, S. 2012 Wave Propagation Methods for Determining Stiffness of Geomaterials; Chapter 7. In P. Giovine, Wave processes in classical and new solids. InTech Publishers.

Schön, J.H. 1983. Petrophysik. Physikalische Eigenschaften von Gesteinen und Mineralen. Akademie-Verlag, Berlin, Germany.

Schön, J.H. 2011. Physical Properties of Rocks. Oxford, United Kingdom.

Schweitzer, J. 2010. Scanning Electron Microscope. http://www.purdue.edu/-rem/rs/sem. html (Oct. 1, 2013).

Selby. M.J. 1993. Hillslope materials and processes. Oxford University Press, Oxford.

Sen, P.N., Godde, P.A., Sibbit, A., 1988. Electrical conduction in clay bearing sandstones at low and high salinities. Journal of Applied Physics 63, 4832–4840.

Sharma, S.P., Anbarasu, . K., Gupta, S. and Sengupta, A. 2010. Integrated very low-frequency EM, electrical resistivity, and geological studies on the Lanta Khola landslide, North Sikkim, India. Landslides 7, 43–53.

Sheriff, R.E and Geldart, L.P. 1995. Exploration Seismology. Press Syndicate of University Cambridge, United Kingdom**.**

Siegesmund, S. and Dürrast, H. 2011. Physical and mechanical properties of rocks. In: Siegesmund, S. and Snethlage, R. (eds) Stone in Architecture, 4th Edition, Springer–Verlag Berlin Heidelberg, 97-225.

Solids Wiki. 2012. Analyzing sieves. http://solidswiki.com/images/-1/1b/Analysis_sieve.gif (Aug 11, 2014).

Springman, S., Jommi, C., Teysseire, P., 2003. Instabilities on moraine slopes induced by loss of suction: a case history. Geotechnique 53(1), 3–10.

Stadler, L., Hinkelmann, R. and Zehe, E. 2009. Two-phase flow simulation of water infiltration into layered natural slopes inducing soil deformation. Proceedings of the International Conference 'Landslide Processes', held in Strasbourg, France, from February 6 to 7, 2009. 197–201.

Stadler, L., Mayer, J., Hinkelmann, R. and Helming, R. 2008. A double continuum approach for two phase flow in porous media. Proceedings of the XVVII International Conference on Computational Methods in Water Resources, San Francisco, U.S.A., 14–18 July 2008.

Swapp, S. 2013. Scanning Electron Microscopy (SEM). http://serc.carleton.edu-/research_education/geochemsheets/techniques/SEM.html (Sep. 4, 2014).

Telford, W.M., Geldart, L.P. and Sheriff, R.E. 1990. Applied Geophysics. Press Syndicate of University Cambridge, United Kingdom.

The Nation, 2011. Land encroachers blamed. Nation Multimedia, 4 April 2011.

Uchida, T., Kosugi, K. and Mizuyama, T. 2001. Effects of pipe flow on hydrological processes and its relation to landslide: a review of pipe flow studies in forested head–water catchments. Hydrological Processes 15(11), 2151–2174.

USDA, 1987. Soil Mechanics Level I, Module 3: USDA Textural Soil Classification. US Department of Agriculture, p. 53.

Wikipedia. 2014. Geotechnical investigation. http://en.wikipedia.org/wiki/-Geotechnical_investigation (Aug. 11, 2014).

Wildenschild, D., Roberts, J.J. and Carlberg, E. 2000. Influence of microstructural properties on geophysical measurements in sand-clay mixtures. Geophysical Research Letters, 27/19, 3085-3088.

Yumuang, S. 2005. Evaluation of potential 2001 debris flow and debris flood in the vicinity of Nam Ko Area, Amphoe Lom Sak, Changwat Phetchabun, Central Thailand. PhD Thesis, Chulalongkorn University, Thailand.

Appendices

Appendix A

Suksawat, S. and Dürrast, H. Seismic velocities of unconsolidated sediments with clay. Proceedings of the Fifth Thailand Rock Mechanics Symposium (ThaiRock 2015), January 22-23, 2015, Romantic Resort & Spa, Khao Yai National Park, Thailand (abstract accepted for publication, full paper in preparation).

Appendix B

Suksawat, S. and Dürrast, H. Electrical resistivity of unconsolidated sediments with clay. THAI JOURNAL OF PHYSICS, SERIES 10, 2014 (in press).

Electrical resistivity of unconsolidated sediments with clay

S. Suksawat[1*], H. Dürrast[1,2]

[1] Department of Physics, Faculty of Science, Prince of Songkla University, HatYai 90112, Thailand
[2] Geophysics Research Center (GRC), Prince of Songkla University, HatYai 90112, Thailand

The shallow subsurface, a few hundred meters in depth, comprises mainly of unconsolidated sediments, a porous material, with gravel, sand, silt, clay, and rock fragments, and it is the source for groundwater as well as the region of landslide hazards, and the main resource in agriculture, soil. For geophysical investigations of this region electrical methods are the first choices, for example soil moisture content in agriculture or vertical electrical sounding in groundwater exploration. For this study disturbed samples of unconsolidated sediments from different layers from bedrock to the top soil layer were taken from two location of the Khao Khohong mountain range near Hat Yai District, Songkhla Province. The two sample locations comprise different bedrock lithologies, sandstone and granite. The dried samples were characterized as following: main composition (X-ray diffraction), grain size distribution (sieve analysis for sand and hydrometer method for clay and silt content), grain matrix density (water pycnometer), bulk density, porosity, as well as pore structure (scanning electron microscopy). The electrical resistivity was determined under laboratory conditions with increasing water saturation (0–100%) of the sample. In general, the electrical resistivity decreases with increasing water content, with a larger gradient until about 40% saturation and a lower one above. The electrical resistivity of clay bearing sediments is the combination of electrolytic (water) and colloidal (wet clay) conductivity. Therefore, we used the modified Archie equation proposed by Sen et al. (1988) to model the laboratory derived data: $\sigma = S^n \phi^m a^{-1} [\sigma_\omega + A Q_v/(1 + C Q_v/\sigma_w)]$, with Q_v replaced by $Q^* = Q_v/S$ (for partial saturation; Günzel, 1994) where σ is the sediment conductivity (inverse of the resistivity), σ_ω is the water conductivity, ϕ is the porosity, $A = 1.93 \times m$ (mho/m)(l/mol) and $CQ_v = 0.7$ (mho/m), m is the tortuosity factor (usually 2), S is the saturation degree, and n is the saturation index (usually 1.3), and a is constant (usually 1). In order to fit our experimental values for the electrical resistivity, respectively conductivity, with $m = 0.3$-3.1, $n = 1.4$-2.2 for sediments from the granite site, and $m = 1.0$-3.9, $n = 2.5$-3.2 for the sandstone site. The reduction in the tortuosity factor might show that larger grain sizes constrict the pathway of electrical current more than smaller grain size material resulting in higher resistivity values. Additionally, the larger grain size material might also result in a more uneven distribution of the clay content, which contributes significantly to the electrical pathway. The increase in the saturation index is mainly related to the too low resistivity values at lower water saturation values.

Keywords: Unconsolidated sediments, Resistivity, Clay, Water saturation

1. INTRODUCTION

Electrical resistivity method is one of the most used geophysical methods in shallow investigation, for example soil moisture content in agriculture, or as vertical electrical sounding in groundwater exploration. It is based on measuring the electrical potentials between one electrode pair while transmitting a direct current between another electrode pair [1]. Electrical resistivity is a parameter exhibiting a large range of values sensitive to various factors like the nature of material (e.g., gravel, sand, and clay), the water content and its conductivity, porosity, permeability, and the water or fluid saturation. The shallow subsurface is a few hundred meters in depth, comprises mainly of unconsolidated sediments, porous material, solid fragmental material from weathering of rocks, transported and deposited by air, but mainly by water, that form layers on the Earth's surface at normal temperature and pressure conditions; near surface in unconsolidated form, e.g., sand, gravel, silt, mud, alluvium [2]. Unconsolidated sediment characteristics are composition, grain size, grain shape, grain arrangement, as well as pore size and shape. Important physical properties of unconsolidated sediments are density (bulk and mineral density), porosity, water saturation, and electrical resistivity, but also seismic velocities [3].

1.1 Study area

For this study disturbed samples of unconsolidated sediments from different layers from bedrock to the top soil layer were taken from two location of the Khao Khohong mountain range in Hat Yai District, Songkhla Province. The two sample locations comprise different bedrock lithology, first, mainly granite at a mountain site in different states of weathering and second, mainly sandstone with different layers from bedrock to top soil. From the later site samples have been collected as a profile from the

---

*Corresponding author. E-mail: saowapa_suksawat@hotmail.com

top layer to the bottom layer (see Fig. 1). The top layer is top soil (KH_1_2), dark grey soil with roots, the second layer is yellowish brown unconsolidated sediment (KH_2_2), and bottom layer is brown unconsolidated sediment (KH_3_2). Below the last layer is bedrock, here a sand/siltstone (see Fig. 1).
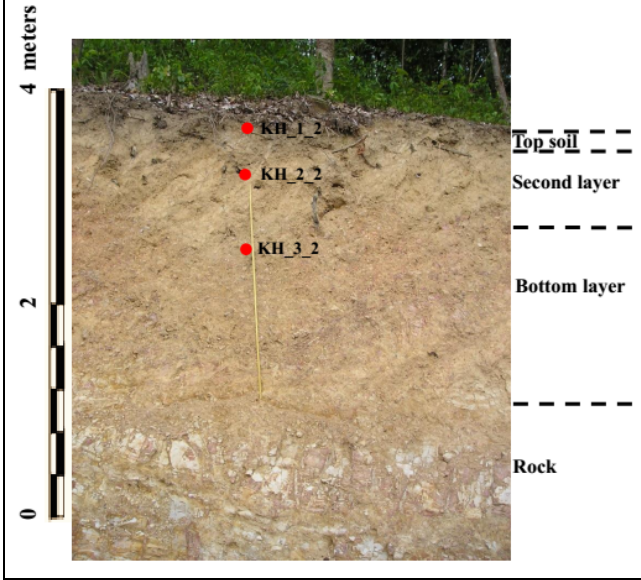

FIGURE 1. Samples of unconsolidated sediments from Khao Khohong Mountain. Bedrock is a sand/siltstone.

1.2 Electrical resistivity

The electrical resistivity (ρ, Ohm-m) of a homogeneous cylindrical solid of length L in meters and with a cross section area A in square meters, having resistance R in ohms between the end faces, is given as, [1]:

$$\rho = \frac{RA}{L} \qquad (1)$$

The resistivity of a saturated porous rock can be expressed by Archie's law [1] as below

$$\rho = aS^{-n}\phi^{-m}\rho_w \qquad (2)$$

where S is the degree of the water saturation, ϕ is porosity, ρ_w is the resistivity of pore fluid or water (it is temperature dependent), m is the tortuosity factor (m are used like porosity exponent, shape factor, or cementation degree), n is saturation exponent, a is the constant (reflects the influence of mineral grains on current flow) [4]. Eq. 2, or Archie equation, is valid only for clay free (clean) sediments as it describes the electrical resistivity of a sample only by the electrolytic conductivity of the pore filling water, respectively fluid.

However, for the interpretation of resistivity data of clay bearing material the factors saturation, porosity, and clay content were identified as crucial [5]. Clay minerals are hydrated minerals, which exhibit high porosity but quite low permeability values. Although clay minerals

themselves are not very conductive, their surfaces can generate an excess of cations in the pore fluid adjacent to the surfaces of the clay minerals. The result is a high conductivity space near to the clay surfaces, which can dominate the overall conductivity of the sediment even if the conductivity of the pore fluid is quite low. Following model for the conductivity of clay bearing sediments is proposed by [5]:

$$\sigma = S^n\phi^m a^{-1}\left[\sigma_w + AQ_v/\left(1 + CQ_v/\sigma_w\right)\right] \quad (3)$$

where, σ is Soil/sediment conductivity in S/m ($\sigma = 1/\rho$), S is degree of the water saturation, ϕ is porosity, σ_w is the conductivity of water, m is the tortuosity factor, n is saturation exponent, a is the constant, A=1.94×m in (S/m)/(mol/l) and C =0.7/Q_v in S/m, Q_v (in mol/l) is the concentration of Na-exchange cations relative to the water saturated pore space, which depends on the cation exchange capacity (C_{ex}) in mol/g and the matrix specific density ρ_m. Q_v replaced by $Q^* = Q_v/S$ (for partial saturation; [6]), with:

$$Q_v = C_{ex}\rho_m\frac{1-\phi}{\phi} \qquad (4)$$

The dependence of the exchange capacity C_{ex} on the relative clay and silt content (mineral composition of clay) P_{clay} and P_{silt} is estimated by a relationship proposed by [6]:

$$C_{ex} = 0.47(P_{clay} + 0.2P_{silt}) \qquad (5)$$

2. EXPERIMENT

The characterization of the unconsolidated sediments comprised the analyses of the main components, grain size distribution, grain shape, grain arrangement and pore structure (size and shape). The main physical properties of unconsolidated sediments investigated here are density (bulk and mineral density), porosity, water saturation, and electrical resistivity.

Semi-quantitative X-ray diffraction (XRD) analysis was used to identify the main components. Diffracted X-rays are used to measure the dimensions of the various atomic layers in the crystals, and different minerals have a distinct set of atomic layer spacing, which can be used to identify the mineral [7]

For analyzing the grain size distribution of the unconsolidated sediment, the distribution of the coarse particles (gravel and sand) was determined by sieve analysis. Fine particles (silt and clay), less than 0.063 mm in size, were analyzed by the hydrometer method. Grain sizes can occur in a wide range of sizes from micrometer to centimeters, and the assumption is that the particles are roughly circular with the diameter measured [8].

For the sieve analysis, weighed samples are poured into a top sieve which has the largest screen opening. Each lower sieve in the layer has smaller opening, at the base is a pan. The shaker shakes the column, usually for some fixed amount of time. After the shaking is complete the material on each sieve is weighed. The weight of the sample of each

sieve is then divided by the total weight to give a percentage retained on each sieve. The hydrometer method is based on the change of density of a soil and water suspension upon the settling of the soil particles. The hydrometer is gently placed into the cylinder containing the suspension after predetermined periods of time and a reading taken by determining where the meniscus of the suspension strikes the hydrometer.

The density, ρ, is defined as the ratio of its mass m to its volume V. It of a material can be separated into the matrix density ($\rho_{Mineral}$) that depends on the components (mineral) and the bulk density (ρ_{Bulk}), which depends on the minerals and the porosity.

The mineral density was determined by the pycnometer methods using water. First, the mass of the empty pycnometer was determined, then the sample was put in and the mass was measured. Distilled water was added to fill the pycnometer (with sample), removing entrapped air and weighted. Finally, the pycnometer was filled with distilled water only and weighted again. The density was calculated from the value of the sample mass per water mass and multiplied by the density of water. The bulk density of a sample was obtained by measuring the dimensions of a geometric sample container filled with the sediment and by this getting the volume and weight of the dry sample.

Porosity, ϕ, is a measure of the total void spaces in a material, and is the volume of voids over the total volume, between 0 and 1. The value for total porosity can be calculated from ϕ=1-(bulk density/mineral density).

Pore space properties are controlling the fluid distribution in the pore space and are important for the characterization of the pore volume fractions of the fluids (porosity, saturation, bulk volume of fluids) [3]. The pore structure with pore space and pore size was analyzed using scanning electron microscopy (SEM). Samples needed to be made conductive by covering the sample with a thin layer of conductive material, here gold [9].

The electrical resistivity measurements were performed following a classical four-electrode-configuration. Electrical current (I) was injected by two electrodes named and the resulting electrical potential (ΔV) is measured by two other electrodes. This geometrical configuration offered a compromise between two contradictory constrains of a small contact (electrical) resistance that requires a large electrode diameter and the assumption of point electrodes needed for calculating the electrical resistivity (ρ) value. With A is cross sectional area in square meters, s is length in m, V in volt and I in ampere. The electrical resistivity was determined under laboratory conditions at room temperature with increasing (tap) water saturation (0–100%) of the air dried sample. The samples were always compacted by hand as much as possible before each measurement of the electrical resistivity.

3. RESULTS AND DISCUSSIONS

The grain size distributions of three of the unconsolidated sediment samples are show in Fig. 2, their frequency and cumulative curves based on the logarithmic particle size method. The grain size distribution of the samples show that more than 50% of the unconsolidated

sediment fraction exceeded 0.063 mm (gravel and sand). KH_1_2 contained less coarse particles (gravel) than KH_2_2 and KH_3_2 as it is the top soil (KH_1_2) and because of weathering, erosion and transportation of particles. But KH_1_2 has a higher sand content than the other two samples, whereas KH_3_2 had the highest clay content.
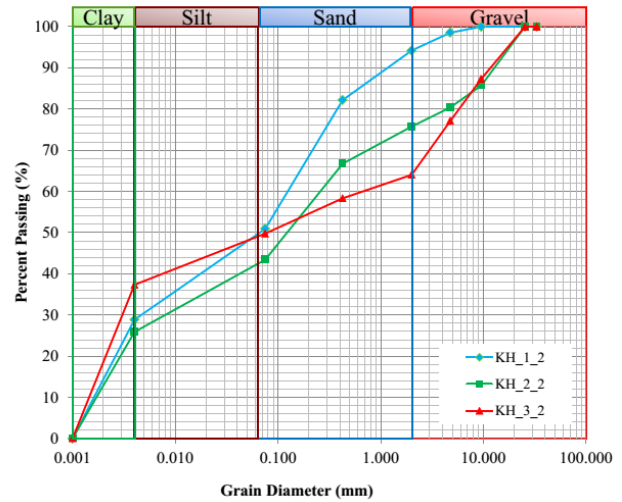

FIGURE 2. Grain size distribution curve for KH_1_2 (top soil), KH_2_2 (second layer), and KH_3_2 (bottom layer)
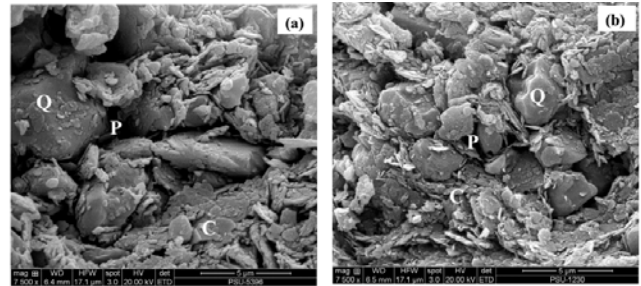

FIGURE 3. SEM microphotographs of unconsolidated sediment samples (a) KH_1_2, top soil, (b) KH_6_2, second layer (parallel sample to KH_2_2). P: pore, Q: quartz grain, C: clay mineral.

The main minerals of the unconsolidated sediments are quartz and clay minerals (illite and kaolinite) based on the XRD results. SEM microphotographs of the samples showed differences in micro texture and morphology due to the mineral content and grain size distribution. Mineral constituents identified under SEM are clay and quartz, consistent with the XRD results. Fig. 3(a) shows SEM microphotographs of KH_1_2 with pores and grains, which have a sub-rounded to angular grain shape, and show a fine to coarse grain size. Fig. 3(b) shows SEM micro-photographs of sample KH_6_2 after 100% water saturation and subsequent drying under air. Smaller pores are seen than in the SEM microphotographs of KH_1_2 because the grains are arranged closer together than before due to the saturation.

Result from the resistivity measurements versus increasing water saturation are shown in Fig. 4 for the three samples, KH_1_2, KH_2_2, and KH_3_2 in semi-log graph. In general, the electrical resistivity decreases when

the water content increases which is in accordance with the theory, see Eq. 2 and 3. It can be seen that for a water content of 0-40% there is a larger gradient for the decrease of the electrical resistivity.
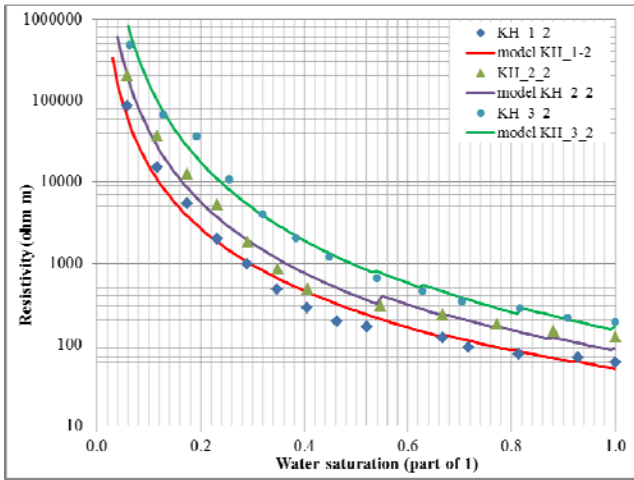

FIGURE 4. Relationship between the degree of water saturation and the electrical resistivity for different sample

Measured resistivity decreases logarithmically with increasing water saturation. The shape of the curve for all three samples is similar, but the absolute values are different, with the resistivity values showing following order: KH_3_2 > KH_2_2 > KH_1_2 (Fig. 4).

The shape of the resistivity curve can be attributed to a combination of electrolytic conductivity of the pore fluid and colloidal conductivity processes related to the clay content. In sediments with clay content, the electrical charges located at the surface of the clay texture lead to less electrical resistivity than in coarse-textured soils because of the magnitude of the specific surface [10]. A large specific surface area supports the surface conductivity because a number of cations in clay minerals are higher valence; electrical charge of the clay mineral surface is negative. It is compensated by the concentration of cations in the pore water in the mineral surface. This process is the cation exchange capacity (CEC). The calculation of the resistivity of clayey material is not trivial, since the electrical current flow is possible through clay minerals as well as through pore fluid [4]. However, for the three samples here the clay content is relatively similar, which might not explain the differences in the absolute resistivity values.

However, the three samples in Fig. 4 show significant difference in the gravel and sand grain size distribution. Sample KH_3_2 has a gravel content of 36% and a sand content of 15%, sample KH_2_2 has 24% and 36%, and sample KH_1_2 has 6% and 47%, respectively. A higher resistivity correlates with a higher content in gravel and vice versa. The larger gravel grains might obstruct the electrical pathway more than the sand grains and might also have an effect on the clay distribution in the sample (see Fig. 5). This would explain that the differences are more or less independent from the saturation degree.
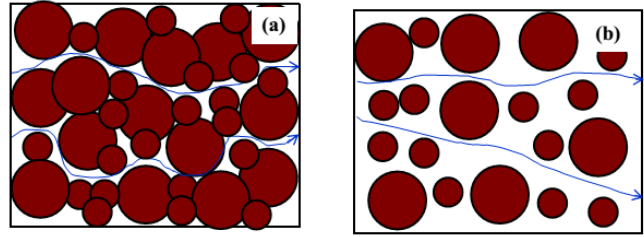

FIGURE 5. Relationship between the grain size and electrical current. a) higher content of larger grain size, b) lower content of larger grains size, white area represent smaller grain sizes.

In Fig. 4 the lines represent the calculations of the electrical resistivity using Eq. 3, using average parameters from the laboratory measuremtns: clay content (percent of clay and silt), porosity, matrix density, and conductivity of the water used. In order to fit a curve with the experimental values from the electrical resistivity measurements, the values m, n, and a in Eq. 3 were changed; it was tried not to change a significantly. When m was increased, the curve changed to higher resistivity values at higher degrees of saturation and the curve changed to much higher resitivity values at lower degrees of saturation when n was incresed. For the three samples shown in Fig. 4 following order for the values m and n were obtained: KH_3_2 > KH_2_2 > KH_1_2. The tortuosity factor m increases with depth and with increasing larger grain size, making it more difficult for the electrical current to find a pathway, thus resulting in a higher resistivity. The increase in n value with depth might reflect the distribution of the pores associated with a larger portion of larger grains.

A summary of all m, n, and a values for nine samples from KH location and seven samples from KB location give following values: m=0.3-3.1, n=1.4-2.2, a = 0.8-1.0 for sediments from the granite site (KB), and m=1.0-3.9, n=2.5-3.2, a=1.0-1.1 for the sandstone site (KH) as shown in Fig. 6. Values of m for KB and KH are overlapping, whereas values of n for KB are less than for KH, illustrating that these values change with sediment type, in general, and that one set of these values cannot be applied to all sediments types.
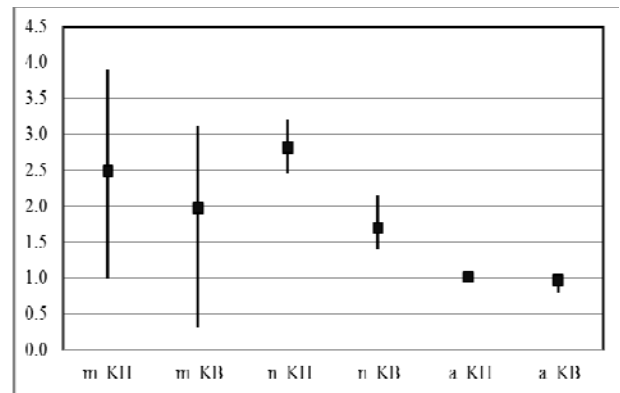

FIGURE 6. Comparison of m, tortuosity factor, n, saturation exponent, and *a*, a constant, of KH (9 samples) and KB (7 samples) location. Line reflects the range of all values, symbols represent the average value for each factor.

4. CONCLUSION

The electrical resistivity of clay bearing unconsolidated sediments is a complex phenomenon. Laboratory measurements have shown that the electrical resistivity decreases when the water content increases because of a combined effect from the electrolytic conductivity of the pore fluid and the colloidal conductivity from the clay mineral, and that the data follow current theory. However, the fitting parameter, m, n, and a, vary with different sediment type. With limited data the difference are clear. Further, the results of this study suggest that the grain size distribution has a significant effect on the absolute resistivity, independent from the water saturation.

1. Telford, W.M., Geldart, L.P. and Sheriff, R.E., Applied Geophysics, Cambridge University Press, UK, 1998

2. Immoor, L., Permeability, porosity and capillarity, http://jroberson.mssd14.wikispaces.net/file/view/Permeability, porosity,capilarity.pdf (March 22, 2014), 2006
3. Schön, J. H., Physical Properties of Rocks, Oxford, United Kingdom, 2011
4. Kirsch, R., Groundwater Geophysics – a Tool for Hydrogeology, Springer-Verlag Berlin Heidelberg, Germany, 2006
5. Sen, P.N., Goode, P.A. and Sibbit, A., Electrical conduction in clay bearing sandstones at low and high salinities, Journal of Applied Physics ,Vol.63, pp.4832. 1988
6. Günzel, F., Geoelektrische Untersuchung von Grundwasser-kontaminationen unter Berücksichtigung von Ton- und Wassergehalt auf die elektrische Leitfähigkeit des Untergrundes, PhD thesis Ludwig-Maximilians-Universität, München, Germany, 1994
7. Lewis, D.W. and McConchie, D., Analytical sedimentology, Chapman & Hall, New York, U.S.A., 1994
8. Wentworth, C. K., A scale of grade and class terms for clastic sediments, The Journal of Geology, Vol.30, pp.377-392. 19222.
9. Schweitzer, J, Scanning Electron Microscope, http://www.purdue.edu/rem/rs/sem.html (March 22, 2014), 2010
10. Samouëlian, A., Cousin, I., Tabbagh, A., Bruand, A. and Richard, G., Electrical resistivity survey in soil science: a review, Soil & Tillage Research, Vol.83, pp.173–193, 2005

Ultrasonic laboratory investigations of unconsolidated sediments with clay

S. Suksawat[1] and H. Dürrast[1,2]

[1] Department of Physics, Faculty of Science, Prince of Songkla University, HatYai 90112, Thailand
[2] Geophysics Research Center (GRC), Prince of Songkla University, HatYai 90112, Thailand

The shallow subsurface, a few hundred meters in depth, comprises mainly of unconsolidated sediments, a porous material, with gravel, sand, silt, clay, and rock fragments, and it is the source for groundwater as well as the region of landslide hazards, and the main resource in agriculture, soil. For this study disturbed samples of unconsolidated sediments from different layers from bedrock to the top soil layer were taken from two location of the Khao Khohong mountain range near Hat Yai District, Songkhla Province. The two sample locations comprise different bedrock lithologies, sandstone and granite. The dried samples were characterized as following: main composition (X-ray diffraction), grain size distribution (sieve analysis for sand and hydrometer method for clay and silt content), grain matrix density (water pycnometer), bulk density, porosity, as well as pore structure (scanning electron microscopy). The seismic velocities, P- and S-wave, were determined at ultrasonic frequencies at 63 kHz and 33 kHz, respectively, under laboratory conditions at 0.12 MPa semi-confining pressure with increasing water saturation (0–100%) of the sample in five steps. In general the seismic velocities do not change much with water saturation. Vp is primary controlled by the bulk modulus of the water, as well as by the porosity and the bulk modulus of the matrix grains (quartz, etc.). The S-wave velocities in general are more consistent for both sample groups and the shear wave velocities have a direct effect on the small strain stiffness. The data from this study show that for the samples from the granite site as well as for the sandstone site the shear velocities significantly decrease at around 60-80% water saturation. This is reflected in a decrease in the shear modulus at the same water saturation percentage. This also correlates with a decrease in the Young's modulus and an increase to almost 0.5 of the Poisson's ratio. All this indicated that at around 60-80% water saturation the mechanical properties of the sediment samples from both sites significantly changes, thus reducing the stiffness of the unconsolidated sediments.

Comments and Suggestions

A number of technical issues as well as service support from other departments were the main reasons for the extension of the project duration. However, finally all planned measurements could be carried out and by this meeting the project objectives.

All of the data will be published, as a full journal paper is in preparation.